Spectroscopic Investigations on the Molecular Motions and Solution Chemistry of the Medicinal Pigment Curcumin

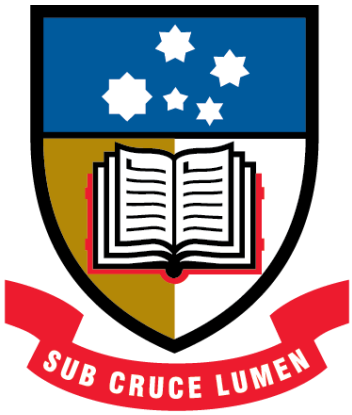

Mandy Hei Man Leung

Department of Chemistry

The University of Adelaide

This dissertation is submitted in total fulfilment of the requirements for the degree of Doctor of Philosophy

January 2015

DECLARATION

I certify that this work contains no material which has been accepted for the award of any other degree or diploma in my name, in any university or other tertiary institution and, to the best of my knowledge and belief, contains no material previously published or written by another person, except where due reference has been made in the text. In addition, I certify that no part of this work will, in the future, be used in a submission in my name, for any other degree or diploma in any university or other tertiary institution without the prior approval of the University of Adelaide and where applicable, any partner institution responsible for the joint-award of this degree.

I give consent to this copy of my thesis when deposited in the University Library, being made available for loan and photocopying, subject to the provisions of the Copyright Act 1968. The author acknowledges that copyright of published works contained within this thesis resides with the copyright holder(s) of those works.

I also give permission for the digital version of my thesis to be made available on the web, via the University's digital research repository, the Library Search and also through web search engines, unless permission has been granted by the University to restrict access for a period of time.

Mandy Hei Man Leung

January 2015

ACKNOWLEDGEMENTS

First and foremost, I would like to thank my supervisor Dr. Tak Kee for his guidance, encouragement and patience since I started my research experiences in the group as an undergraduate. His knowledge in ultrafast spectroscopy and continuous support have been invaluable.

I would also like to thank my co-supervisors, Prof. Stephen Lincoln and Assoc. Prof. Greg Metha, for their advice and support. Their wisdom and passion in Science have been truly inspiring.

Thanks also go to Dr. Tara Pukala for her expertise in the mass spectrometry, Dr. Denis Scanlon for his expertise in the high performance liquid chromatography, Dr. Truc Pham for his advice in data analysis, Dr. Matt Addicoat for his expertise in computational chemistry. I would like to thank Assoc. Prof. Sheng Dai and Dr. Qiuhong Hu at the School of Chemical Engineering in the University of Adelaide for their advice and equipment, which allow detail characterisation of my samples. Thanks must also go to Mr. Kevin Kuan, Ms. Annelie Karssen and Mrs. Pravena Bako for their assistance with experiments. I would also like to thank Mr. Peter Apoefis, Mr. Philip Clements, Mr. Matthew Bull, Mr. Graham Bull and Mr. Gino Farese for their technical support.

A big thank you to all the past and present Postdocs, PhD and Honours students whom I have had the pleasure of exchanging ideas in science and sometimes non-science related topics. Special thanks go to Mr. Scott Clafton for his help in time-resolved fluorescence upconversion, Mr. Takaaki Harada for his assistance with the NMR and laser experiments and Mr. Patrick Tapping for his assistance with laser maintenance. Also, I would like to thank them for proofreading this thesis.

Finally, I would like to thank my parents for being understanding and encouraging.

ABSTRACT

Curcumin is the bioactive molecule in the pigments found in turmeric, a spice and traditional medicine in Asia for centuries. Research has shown that curcumin exhibits a number of medicinal benefits, in particular, anti-Alzheimer's and anti-cancer properties. It has been shown that there is an elevated level of Cu(II) in amyloid plaques and tumours. In addition, curcumin has the ability to damage the DNA of cancer cells in the presence of Cu(II), which leads to apoptosis. Furthermore, the tautomerisation of curcumin is essential for the binding of amyloid aggregates, which is associated with Alzheimer's disease. This thesis provides insight into the interaction between curcumin and copper ion and tautomerisation of curcumin, which are related to the proposed modes of action for curcumin. In addition, a method for stabilising of curcumin in an aqueous environment using biocompatible polyester nanoparticles is described in this thesis. These nanoparticles show potential applications as curcumin delivery systems in biological environment.

As a part of the PhD thesis, the interaction between curcumin and Cu(II) has been investigated in methanol and the sodium dodecyl sulphate (SDS) micellar solution. The fluorescence quenching results show that curcumin forms both 1:1 and 1:2 Cu(II)−curcumin complexes and the binding constants are on the order of 10^5 – 10^8 M^{-1}, which indicate a strong binding between curcumin and Cu(II). The transient absorption spectroscopic results reveal that the strong interaction between curcumin and Cu(II) changes the electronic excited states of curcumin substantially.

In addition, the decomposition of Cu(II)−curcumin complexes in a reducing environment has been studied. The UV-visible absorption values of the Cu(II)−curcumin complex in acetonitrile and in SDS micellar solution with ascorbic acid show a monotonic decrease as a function of time, indicating decomposition of curcumin in a reduc-

ing environment. In contrast, a lack of decomposition of Cu(II)−curcumin complex in methanol and curcumin in the presence of Cu(I) in acetonitrile was observed. The fluorescence results reveal that curcumin has a weaker interaction with Cu(I) than Cu(II). Therefore, the decomposition of curcumin is associated with the reduction of Cu(II) to Cu(I).

The tautomerisation of curcumin in methanol, acetone and acetonitrile has been investigated by nuclear magnetic resonance spectroscopy. As tautomerisation of curcumin is the rate limiting step of the deuteration at the α-carbon position (C_α), the rate of tautomerisation is inferred from the rate of deuteration at the C_α of curcumin. The proton resonance peak corresponding to the hydrogen of C_α decays as a function of time, signifying a successful hydrogen-deuterium exchange. The rate constants of tautomerisation of curcumin have been measured at several temperatures and analysis using the Arrhenius equation has revealed that the activation energy of tautomerisation of curcumin is between 60 and 80 $\mathrm{kJ\,mol^{-1}}$. The high activation energy values are attributable to the high energy barrier for disrupting the intramolecular hydrogen bonding and extended π-conjugation in the keto-enol tautomer of curcumin.

Although curcumin has shown many medicinal effects, there are two major challenges regarding the utilisation of curcumin for disease treatments. These challenges are the poor solubility of curcumin in an aqueous environment and its lack of stability under physiological conditions. A one-step nanoprecipitation method to prepare curcumin-encapsulated polyester nanoparticles using polylactic acid, poly(lactide-*co*-glycolide) and poly(ε-caprolactone) has been developed. The resulting nanoparticles have an average diameter less than 100 nm and a negative surface charge, which enables these nanoparticles to remain suspended in water. Furthermore, the UV-visible absorption values of the curcumin-polyester nanoparticles show only a minor decrease as a function of time, indicating that the polyester nanoparticles are able to prevent curcumin degradation. The results from studies using fluorescence upconversion spectroscopy reveal a lack of deuterium isotope effect of curcumin encapsulated in the polyester nanoparticles in the presence of D_2O. As a result of limited interaction between curcumin and water, the degradation of curcumin is suppressed. Overall, the polyester nanoparticles show significant potential as curcumin delivery agents.

PUBLICATIONS

The following publications contains some of the work presented in this thesis:

Leung, M. H. M.[†]; Harada, T.[†]; Kee, T. W. Delivery of Curcumin and Medicinal Effects of the Copper(II)-Curcumin Complexes. *Curr. Pharm. Des.* **2013**, *19*, 2070–2083. [†]These authors contribute equally to this review article.

Leung, M. H. M.; Pham, D.-T.; Lincoln, S. F.; Kee, T. W. Femtosecond Transient Absorption Spectroscopy of Copper(II)-Curcumin Complexes. *Phys. Chem. Chem. Phys.* **2012**, *14*, 13580–13587.

Leung, M. H. M.; Mohan, P.; Pukala, T. L.; Scanlon, D. S.; Lincoln, S. F.; Kee, T. W. Reduction of Copper(II) to Copper(I) in the Copper-Curcumin Complex Induces Decomposition of Curcumin. *Aust. J. Chem.* **2012**, *65*, 490–495.

The following publications are currently in preparation and will each contain some of the work presented in this thesis:

Leung, M. H. M.; Addicoat, M. A.; Clafton, S. N.; Metha, G. F.; Kee, T. W., Keto-Enol Tautomerisation of the Medicinal Pigment Curcumin (In Preparation).

Leung, M. H. M.; Kee, T. W., Nanoprecipitation and Spectroscopic Characterisation of Curcumin-Encapsulated Polyester Nanoparticles (In Preparation).

CONTENTS

Contents vi

List of Figures x

List of Tables xiii

1 Overview 1

1.1 Curcumin 1

1.2 Introduction of Spectroscopic Techniques 5

1.2.1 UV-visible Absorption Spectroscopy 5

1.2.2 Fluorescence Emission Spectroscopy 5

1.2.3 Dynamic Light Scattering 6

1.2.4 Zeta Potential 6

1.3 Summary of Thesis Chapters 8

1.4 References 11

2 Ultrafast Laser and Time-Resolved Spectroscopy 22

2.1 Titanium Sapphire Laser 22

2.1.1 Mode-locking 23

2.1.2 Dispersion Compensation 28

2.1.3 Chirped Pulse Amplification 29

2.2 Ultrafast Laser Setup 30

2.3 Parametric Non-linearities 32

2.3.1 Optical Parametric Amplification 33

2.4 Time-resolved Spectroscopy 35

2.4.1 Transient Absorption Spectroscopy 36
2.4.2 Fluorescence Upconversion Spectroscopy 38
2.5 References 40

3 Femtosecond Transient Absorption Spectroscopy of Copper(II)–Curcumin Complexes 42
3.1 Abstract 44
3.2 Introduction 45
3.3 Materials and Methods 47
3.3.1 Materials 47
3.3.2 Sample Preparation 47
3.3.3 UV-visible Absorption and Fluorescence Emission Spectroscopy 47
3.3.4 Determination of Binding Constants from Titration Experiment 48
3.3.5 Femtosecond Transient Absorption Spectroscopy 49
3.4 Results and Discussion 51
3.4.1 UV-visible Absorption and Fluorescence Spectroscopy of the Copper(II)–Curcumin Complexes 51
3.4.2 Complexation Constants of the Copper(II)–Curcumin Complexes 52
3.4.3 Speciation of the Copper(II)–Curcumin Complexes 58
3.4.4 Transient Absorption Spectra of Curcumin in Methanol and SDS micelles 59
3.4.5 Transient Absorption Spectra of the Copper(II)–Curcumin Complexes 61
3.4.6 Excited State Kinetics of Curcumin and the Copper(II)–Curcumin Complexes 63
3.4.7 Kinetic Modelling Analysis 66
3.5 Conclusions 69
3.6 References 70

4 Reduction of Copper(II) to Copper(I) in the Copper–Curcumin Complex Induces Decomposition of Curcumin 74
4.1 Abstract 77

4.2 Introduction 78
4.3 Materials and Methods 80
4.3.1 Materials 80
4.3.2 UV-visible Absorption and Fluorescence Studies 80
4.4 Results and Discussion 82
4.4.1 Time-dependent UV-visible Absorption Spectra of the Copper–Curcumin Complex 82
4.4.2 Reduction of Cu(II) to Cu(I) in Acetonitrile 85
4.5 Conclusions 89
4.6 References 90

5 Keto-Enol Tautomerisation of the Medicinal Pigment Curcumin 95
5.1 Abstract 96
5.2 Introduction 97
5.3 Materials and Methods 100
5.3.1 Materials 100
5.3.2 ^{1}H NMR Spectroscopy 100
5.3.3 Data Analysis 100
5.4 Results and Discussion 103
5.4.1 Deuteration of Curcumin at C_{α} 103
5.4.2 From Deuteration to Tautomerisation of Curcumin 107
5.4.3 Activation Energy for Tautomerisation of Curcumin 110
5.5 Conclusions 113
5.6 References 114

6 Nanoprecipitation and Spectroscopic Characterisation of Curcumin-Encapsulated Polyester Nanoparticles 119
6.1 Abstract 119
6.2 Introduction 121
6.3 Materials and Methods 124
6.3.1 Materials 124
6.3.2 Preparation of Curcumin-polyester Nanoparticles 124
6.3.3 Dynamic Light Scattering Measurement 125

6.3.4 Steady State UV-visible Absorption and Fluorescence Spectroscopy 126
6.3.5 Time-resolved Fluorescence Spectroscopy 126
6.4 Results and Discussion 128
6.4.1 Characterisation of Curcumin-polyester Nanoparticles 128
6.4.2 Solution Stability of Curcumin-polyester Nanoparticles 132
6.4.3 Time-resolved Fluorescence Spectroscopy of Curcumin-polyester Nanoparticles 137
6.5 Conclusions 142
6.6 References 143

7 Concluding Remarks 150
7.1 References 152

Appendix A 153
A.1 Time-dependent Mass Spectrometry of the Copper(II)–Curcumin Complex 153
A.2 Time-dependent High Performance Liquid Chromatography of the Copper(II)–Curcumin Complex 157

Appendix B 160
B.1 MATLAB Script for the Determination of the Rate Constant of Tautomerisation of Curcumin 160

Appendix C 162
C.1 Determination of the Number of Curcumin Encapsulated in Polyester Nanoparticles 162
C.2 Determination of the Distance between Adjacent Curcumin 165

List of Figures

1.1 Diagram of electric layers of a negatively charged nanoparticle. 7

2.1 Energy diagram of Ti^{3+} ion. 23
2.2 Time- and frequency-domain description on mode-locking. 24
2.3 Active mode-locking with an acousto-optic modulator. 26
2.4 Non-linear Kerr effect. 27
2.5 Dispersion compensation of a positively-chirped pulse using the four prism sequence. 28
2.6 Schematic layout of a chirped pulse amplifier, which consists of a stretcher, a regenerative amplifier and a compressor. 29
2.7 Second-order non-linear optical effect. 32
2.8 Time-resolved pump-probe spectroscopy. 35
2.9 Time-resolved pump-probe transient absorption spectroscopy. 36
2.10 Time-resolved fluorescence upconversion spectroscopy. 39

3.1 Structure of curcumin, the 1:1 and 1:2 Cu(II)–Curcumin complexes. 45
3.2 Absorption and fluorescence spectra of curcumin and the Cu(II)–Curcumin complexes in methanol and SDS micelles. 51
3.3 Fluorescence quenching of curcumin as a result of addition of Cu(II) in methanol and SDS micelles. 53
3.4 Normalised fluorescence intensity at 540 and 530 nm for various ratio of curcumin and Cu(II) in methanol and the SDS micelles. 54
3.5 Hill plot of fluorescence quenching of curcumin as a result of addition of Cu(II) in methanol and SDS micelles. 56

3.6 UV-visible absorption spectra of curcumin in methanol and SDS micelles with addition of Cu(II). 57
3.7 Speciation plot of free curcumin and Cu(II)–Curcumin complexes in methanol and SDS micelles. 58
3.8 Transient absorption spectra of curcumin and Cu(II)–Curcumin complexes in methanol and SDS micelles at various time delays. 60
3.9 Excited state absorption signals of curcumin and Cu(II)–Curcumin complexes with various Cu(II) to curcumin ratios in methanol and SDS micelles. 62
3.10 Excited state kinetics at 500 nm for Cu(II)–Curcumin complexes with excess Cu(II) in methanol and SDS micelles. 64
3.11 Proposed kinetic models for curcumin and the Cu(II)–Curcumin complexes. 67

4.1 Chemical structures of curcumin and 1:1 Cu(I)–Curcumin complex. 78
4.2 Time-dependent UV-visible absorption spectra of curcumin in acetonitrile and methanol in the presence of Cu(II). 83
4.3 Time-dependent UV-visible absorption spectra of curcumin in acetonitrile with an addition of water and Cu(I). 84
4.4 UV-visible absorption and fluorescence emission spectra of curcumin in acetonitrile with various concentrations of Cu(I). 86
4.5 UV-visible absorption and fluorescence emission spectra of curcumin in acetonitrile with various concentrations of Cu(II). 87
4.6 Time-dependent UV-visible absorption spectra of curcumin in the presence of ascorbic acid and Cu(II) in SDS micelles. 88

5.1 Structure of keto-enol and diketo tautomers of curcumin. 97
5.2 NMR spectra of curcumin in methanol-d_4, D_2O/acetone-d_6 and D_2O/acetonitrile-d_3. 102
5.3 Time-dependent ^1H NMR spectra of curcumin at 45 °C in methanol-d_4, D_2O/acetone-d_6 and D_2O/acetonitrile-d_3. 106
5.4 Fluorescence upconversion data of curcumin in methanol and methanol-d_4 at ambient temperature over time. 107

5.5 The decrease in the normalised H_α signal of curcumin in methanol-d_4, D_2O/acetone-d_6 and D_2O/acetonitrile-d_3 as a function of time at several temperatures. 109
5.6 Arrhenius plot of the rate constants of tautomerisation of curcumin at various temperatures. 111
5.7 DFT optimised geometry of the transition state of tautomerisation of curcumin with various number of water molecules. 112

6.1 Chemical structure of curcumin, polylactate, poly(D,L-lactide-*co*-glycolide) and poly(ε-caprolactone). 122
6.2 Particle size distribution and zeta potential of Cur-polyester nanoparticles in neat water. 128
6.3 Time-dependent particle size measurements of Cur-polyester nanoparticles in neat water. 130
6.4 Steady state UV-visible absorption and fluorescence emission spectra of Cur-PLA, Cur-PLGA and Cur-PCL nanoparticles in neat water. 133
6.5 Stability of Cur-PLA, Cur-PLGA and Cur-PCL nanoparticles in neat water by steady state UV-visible absorption spectroscopy. 135
6.6 Stability of 1:15 curcumin:monomer units molar ratio of Cur-PLGA and Cur-PCL nanoparticles in neat water by steady state UV-visible absorption spectroscopy. 136
6.7 Fluorescence upconversion data of Cur-PLA, Cur-PLGA and Cur-PCL nanoparticles in neat water. 138

A.1 Mass spectra of curcumin in the presence of Cu(II) in acetonitrile as a function of time. 155
A.2 Mass spectra of curcumin in acetonitrile as a function of time. 155
A.3 Mass spectra of curcumin in acetonitrile with various Cu(II) concentrations. 156
A.4 HPLC chromatograms of curcumin in the presence of Cu(II) in acetonitrile as a function of time. 158
A.5 HPLC chromatograms of curcumin in acetonitrile as a function of time. 159

LIST OF TABLES

3.1 Binding Constants and Hill Coefficients of Complexation between Curcumin and Cu(II) in Methanol and the SDS Micelles. 55

3.2 Transient Absorption Kinetic Parameters at 500 nm with Various Cu(II) to Curcumin Ratios in Methanol and SDS Micelles. 65

3.3 Summary of Linear Combination Kinetic Fitting. 68

5.1 Rate Constants of Tautomerisation of Curcumin in Methanol-d_4, D_2O/Acetone-d_6 and D_2O/Acetonitrile-d_3 at Several Temperatures 108

6.1 Summary of Particle Diameter, Zeta Potential, Rate of Degradation and Fluorescence Quantum Yield of Curcumin-encapsulated Polyester Nanoparticles in Neat Water. 129

6.2 Fluorescence Upconversion Decay Parameters for Curcumin-encapsulated Polyester Nanoparticles in Neat Water. 139

6.3 Fluorescence Upconversion Decay Amplitude Parameters with Fixed Time Constants for Curcumin-encapsulated Polyester Nanoparticles in Neat Water. 141

C.1 Calculated Parameters of Cur-polyester Nanoparticles. 163

C.2 Physical Parameters of Curcumin and Polyester Used in Preparation of Cur-polyester Nanoparticles. 163

C.3 Average Number of Curcumin in Cur-polyester Nanoparticles. 164

C.4 Average Distance between Adjacent Curcumin in Cur-polyester Nanoparticles. 165

List of Abbreviations

E_a	Activation energy
$[Cu^{II}–Cur_2]$	1:2 Cu(II)–Curcumin complexes
$[Cu^{II}–Cur]^+$	1:1 Cu(II)–Curcumin complexes
AOM	Acousto-optic modulator
BBO	β-Barium borate
C_α	Carbon at the α position
CPA	Chirped pulse amplification
CTAB	Cetyltrimethylammonium bromide
Cur-PCL NP	Curcumin-encapsulated poly(ε-caprolactone) nanoparticles
Cur-PLA NP	Curcumin-encapsulated polylactate nanoparticles
Cur-PLGA NP	Curcumin-encapsulated poly(D,L-lactide-*co*-glycolide) nanoparticles
Cur-polyester NP	Curcumin-encapsulated polyester nanoparticles
DNA	Deoxyribonucleic acid
DTAB	Dodecyltrimethylammonium bromide
EPR	Enhanced permeability and retention
ESA	Excited state absorption

ESIHT	Excited-state intramolecular hydrogen atom transfer
fwhm	Full width at half maximum
GVD	Group velocity dispersion
H/D exchange	Hydrogen and deuterium exchange
HPLC	High performance liquid chromatography
NIR	Near infrared
NMR	Nuclear magnetic resonance
PBS	Phosphate buffer solution
PCL	Poly(ε-caprolactone)
PLA	Polylactate
PLGA	Poly(D,L-lactide-*co*-glycolide)
SDS	Sodium dodecyl sulphate
SE	Stimulated emission
SFG	Sum frequency generation
SHG	Second harmonic generation
SPM	Self-phase modulation
THF	Tetrahydrofuran
Ti:sapphire	Titanium-doped sapphire crystal
UV	Ultraviolet

CHAPTER 1

OVERVIEW

1.1 Curcumin

Turmeric, the rhizome of the plant *Curcuma longa*, is commonly used in Asian cooking and traditional medicine [1–3]. The bright yellow colour of turmeric is derived from a group of molecules known as curcuminoids, which were first isolated in 1815 by Vogel and Pelletier [4]. There are three major components identified, namely curcumin (77 %), demethoxycurcumin (17 %) and bisdemethoxycurcumin (3 %), and a trace amount of cyclocurcumin [4, 5]. This thesis focusses on curcumin owing to its intriguing photophysical properties and beneficial biological activities. The chemical name of curcumin is (1*E*,6*E*)-1,7-bis(4-hydroxy-3-methoxyphenyl)-1,6-heptadiene-3,5-dione, and it has a molecular weight of 368.38 g/mol. It exists as an orange-yellow solid with a melting point of 183 °C. There are two tautomeric forms of curcumin, which are the keto-enol and diketo tautomers. A recent study by Payton et al. has demonstrated that the keto-enol tautomer is the dominant form of curcumin in a variety of solvents from non-polar organic solvents to mixtures of water with dimethylsulphoxide, which have dielectric constants ranging from 4.8 to 47 [6].

There is an increasing interest in the photophysics of curcumin because of its photosensitising effect [7, 8]. Upon photo-excitation, photosensitisers induce the formation of radicals, which cause cell damage and lead to apoptosis of cells [9]. Owing to the high time resolution of ultrafast time-resolved fluorescence upconversion spectroscopy, the fast dynamics of excited-state curcumin have been investigated [10–12]. Recent studies have demonstrated that solvation and excited-state intramolecular hydrogen atom transfer (ESIHT) are the major relaxation pathways of excited-state curcumin [10–13]. The time constants of solvation and ESIHT for curcumin in methanol

are 12 ps and 70 ps, respectively [10]. In particular, ESIHT exhibits a strong deuterium isotope effect, which results in slower dynamics characterised by a time constant of 120 ps in deuterated methanol while solvation remains unaffected [10]. The prominent deuterium isotope effect of the excited-state curcumin is also observed in micellar solutions [11]. Micelles are dynamic colloidal aggregates that are formed by surfactant molecules, which consist of a hydrophilic head group and a hydrophobic tail [14]. At the concentrations above the critical micelle concentration, the interactions of the hydrophobic tails of surfactants become the dominant interaction, which leads to spontaneous formation of micelles. It has been demonstrated that micelle aggregates enhance solubility and stability of curcumin in aqueous environment [15–18]. The deactivation of excited state of curcumin by ESIHT exhibits a time constant approximately 1.6 times slower in SDS micelle with deuterated water [11]. The presence of the intramolecular hydrogen bonding greatly influences the photophysics of keto-enol curcumin.

In addition to the use of curcumin in traditional medicine, it has been demonstrated that curcumin exhibits therapeutic activities against inflammation [19–26], cystic fibrosis [27–29], Alzheimer's disease [30–33], and cancers [24, 34–39]. Furthermore, there are no significant side effects associated with the use of curcumin as a large oral dose of up to 12 g of curcumin has shown insignificant toxicity in human subjects [40]. Although detailed mechanisms of the mode of action for curcumin are unclear, studies have shown that the interaction between curcumin and transition metals, namely copper and iron, may be an important aspect of the anti-cancer and anti-amyloid formation properties of curcumin [41–49]. In particular, the anti-cancer activities of curcumin have been related to metal-mediated deoxyribonucleic acid (DNA) damage by curcumin [42–44, 46, 50–55]. A strong interaction between Cu(II)−Curcumin complexes and double stranded DNA has been reported [50]. Furthermore, it has been demonstrated that curcumin exhibits pro-oxidant effects in the presence of copper [43, 46]. Although curcumin is well known for its anti-oxidant effect and it protects DNA from damage by radicals, it has been demonstrated that curcumin interacts and damages DNA in the presence of copper and causes cell apoptosis, in particular for cancer cells [42, 45, 51, 53–55]. As a result of reduction of Cu(II) to Cu(I), curcumin is oxidised and reactive oxygen species are generated, which leads to DNA damage [42–44, 46, 51, 52]. However, little is known about the nature of the interaction between

curcumin and copper even though curcumin exhibits prominent biological activity in the presence of copper. As a consequence, developing a good understanding of the interaction between curcumin and copper is fundamental and will lead to insight into the biological activities of curcumin.

In addition to the copper-mediated effects, some of the biological activities of curcumin have been related to its keto-enol tautomerisation. As mentioned before, there are two tautomeric forms of curcumin with the keto-enol tautomer as the dominant form [6]. It has been demonstrated that curcumin inhibits the formation of amyloid β fibrils by binding to small amyloid β species [32]. Furthermore, the curcumin derivatives that lack the ability to tautomerise exhibit a weaker interaction with the amyloid β aggregates than the native form of curcumin [56]. In other words, tautomerisation of curcumin plays a role in its effectiveness against amyloid fibril formation. Therefore, this reaction of curcumin may be important to its medicinal activities and studies on tautomerisation of curcumin will provide further insight into the relationship between its molecular structure and medicinal activities.

Although curcumin exhibits a number of therapeutic activities, two critical issues that hinder its bioavailability must be addressed in order for curcumin to be utilised as an effective therapeutic agent. While it is well known that polar organic solvents can solubilise curcumin at a high concentration, it is important to consider its solubility and stability in an aqueous environment for biological applications. The solubility of curcumin is approximately 30 nM in an aqueous environment [57, 58]. In addition, although the solubility of curcumin is increased under alkaline conditions, curcumin undergoes rapid degradation by hydrolysis. The hydrolysis of curcumin leads to formation of *trans*-6-(4'-hydroxy-3'-methoxyphenyl)-2,4-dioxo-5-hexenal as the major degradation product, which further fragments to vanillin, ferulic acid and feruloyl methane [59].

To address the rapid degradation of curcumin in an aqueous environment, research with a focus on encapsulation of curcumin using delivery agents to improve its aqueous solubility and stability is ongoing. Such delivery agents require two key features to achieve a high solubility and stability of curcumin: (1) a hydrophobic region, which is essential to stabilise curcumin as well as segregate curcumin from water to prevent its rapid hydrolysis, and (2) a hydrophilic exterior, which is necessary to disperse the

delivery agents loaded with curcumin in an aqueous environment. Recent work has focussed on curcumin delivery agents such as micelles [15–18], polymer nanoparticles [60–64], plasma proteins [65–67] and cyclodextrins [68–70]. Surfactant micelles are often used for solubilising and stabilising hydrophobic molecules. The structures of surfactant and lipid molecules consist of hydrophobic alkyl chain(s) and a hydrophilic head group [71, 72]. In the formation of micelles in an aqueous environment, the alkyl chains of surfactants aggregate and form a hydrophobic core, while the polar head groups provide charges on the surface of the micelles. It is important to note that, the formation of micelles only occurs above the critical micelle concentration [71]. Curcumin is stable in anionic and neutral micelles including sodium dodecyl sulphate (SDS) and Triton-X 100 [15, 16]. In other previous work, cationic micelles such as cetyltrimethylammonium bromide (CTAB) and dodecyltrimethylammonium bromide (DTAB) also show significant stabilisation of curcumin at pH 13 where rapid hydrolysis is expected [17, 18]. The stabilising effect of curcumin by micelles is attributable to the strong interaction between curcumin and the hydrophobic regions of the micelles. As the encapsulated curcumin is separated from water, the hydrolysis reaction is suppressed [18].

Similarly, synthetic polymers also form aggregates to yield polymer nanoparticles, which are used to stabilise and solubilise hydrophobic molecules in an aqueous environment. In particular, polyester nanoparticles are widely used in biological applications because of their biocompatibility. For instance, poly(D,L-lactide-*co*-glycolide) (PLGA) and poly(ε-caprolactone) (PCL) are biodegradable, which undergo hydrolysis of their ester bonds to form smaller units that can be metabolised by cells [73, 74]. Recent studies have demonstrated that the curcumin-encapsulated polyester nanoparticles exhibit medicinal activities against cancer [75–77], cystic fibrosis [27] and inflammation [78, 79]. Furthermore, the bioavailability of curcumin is improved significantly using polyester nanoparticles as delivery systems due to enhancements of its aqueous stability and solubility [60–63]. Investigating the photophysics of curcumin in these nanoparticles provides insight into the behaviour of curcumin in nanoparticles, which may be important for its applications in therapy.

1.2 Introduction of Spectroscopic Techniques

1.2.1 UV-visible Absorption Spectroscopy

UV-visible absorption spectroscopy enables quantitative measurement of absorption of photons in the UV-visible spectral region by pigment molecules, which is known as absorbance and is represented by the following.

$$A = \log(\frac{I_0}{I})$$

where A is the absorbance, I_0 is the intensity of an incident light and I is the intensity of a transmitted light. The π-electrons of curcumin absorb the energy in the visible light and promoted to the excited-state and the absorption maxima occur between 420 – 450 nm depending on the solvent environment [66, 80]. The use of UV-visible spectroscopy in studying degradation of curcumin has been previously demonstrated [16–18, 41, 59, 69, 81–83]. The principle behind is based on the relationship between absorbance and concentration of curcumin, as described by the Beer-Lambert Law shown in Equation (1.1) [84].

$$A = \varepsilon cl \tag{1.1}$$

where A is the absorbance, ε is the molar extinction coefficient of curcumin, c is the concentration of curcumin and l is the path length of the sample. Therefore, the change in the concentration of curcumin is inferred from the change in absorbance according to Equation (1.1).

1.2.2 Fluorescence Emission Spectroscopy

Fluorophores are molecules that deactivate the excited states by emitting photons, which is known as fluorescence emission. Fluorescence emission spectroscopy measures the fluorescence emission after photo-excitation of a fluorophore. Furthermore, fluorescence quantum yield (ϕ_{Fl}) quantifies the efficiency of emission by a fluorophore and it is routinely determined by comparison with a known standard, as shown in

Equation (1.2) [85, 86].

$$\phi_{\text{unknown}} = \phi_{\text{standard}}\left(\frac{\text{Gradient}_{\text{unknown}}}{\text{Gradient}_{\text{standard}}}\right)\left(\frac{\eta_{\text{unknown}}}{\eta_{\text{standard}}}\right) \tag{1.2}$$

where the gradient is determined from plotting the integrated fluorescence intensities at various absorbance values and η is the refractive index of the solvent. In particular, curcumin has typical emissions around 460 – 550 nm and a ϕ_{Fl} value less than 10 % depends on the solvent environment [11, 17, 18, 66, 80]. Furthermore, the fluorescence emission of curcumin is quenched by the presence of water as non-radiative decay of the excited state becomes the dominant process [87, 88].

1.2.3 Dynamic Light Scattering

Small particles in colloidal solution undergo a random movement known as Brownian motion [89, 90]. Dynamic light scattering is commonly used to determine the size distribution of a colloidal solution, which is illuminated by monochromatic light with wavelength higher than particle's size [89, 90]. The Brownian motion of particles changes the frequency and the phase of the scatting light and diffusion coefficient of particles (D) can be determined from the fluctuations of the scattered light by particles are detected at a known scattering angle, as shown in Equation (1.3) [89, 90].

$$D = \frac{kT}{6\pi \mathrm{r}\eta} \tag{1.3}$$

where k is the Boltzmann constant, T is the temperature, η is the viscosity and r denotes the hydrodynamic radius of the particle. Therefore, the size of the particle is determined from its velocity of diffusion.

1.2.4 Zeta Potential

The liquid layer surrounding the particle exists as two parts called the Stern layer and diffuse layer [91]. The potential at the shear plane in the diffuse layer relative to bulk solution is known as the zeta potential, as shown in Figure 1.1. The magnitude of zeta potential indicates the stability of the colloidal system and it is related to the electrophoretic mobility or the velocity of particles in an electric field, as shown in

Equation (1.4) [91–93].

$$U_E = \frac{2\upsilon\zeta f(\kappa a)}{3\eta} \tag{1.4}$$

where U_E is the electrophoretic mobility, υ is the dielectric constant, ζ is the zeta potential, η is the viscosity and $f(\kappa a)$ denotes the Henry's function, which is generally approximated as 1.5 for aqueous solution [92, 93]. Using Equation (1.4), the zeta potential of particles is determined from the electrophoretic mobility.

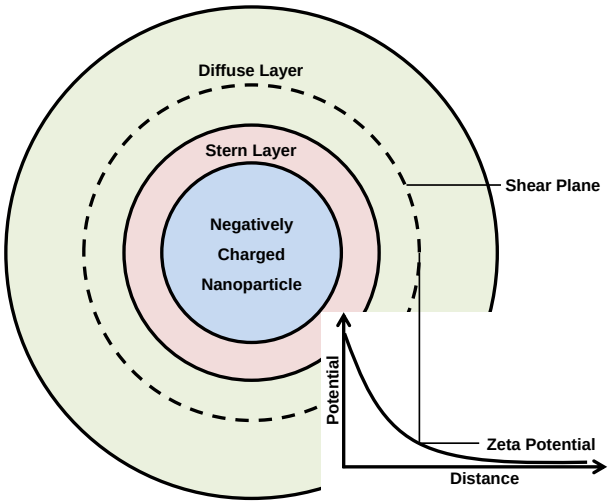

Figure 1.1. Diagram of the diffuse and Stern layers of a negatively charged nanoparticle and the potential between the shear plane and the bulk solution is known as the zeta potential.

1.3 Summary of Thesis Chapters

This thesis starts with an introduction of the techniques for the generation of ultrashort laser pulses and time-resolved spectroscopy, which is followed by a presentation of studies on the solution chemistry and photophysics of curcumin in various environments using this spectroscopic technique. The purpose of the studies presented is to gain insight into two processes that play a role in the mode of action for curcumin: (1) the interaction between curcumin and copper ion and (2) the tautomerisation of curcumin. Finally, the stabilisation of curcumin in water using biocompatible polyester nanoparticles is presented.

In Chapter 2, the generation of high gain ultrafast laser pulses by mode-locking and chirped pulse amplification is discussed. Then, descriptions of our ultrafast laser set-up and the use of an optical parametric amplifier to generate a wide range of wavelengths are given. In addition, an overview of two types of time-resolved spectroscopy, namely transient absorption and fluorescence upconversion, is presented.

The ligand-metal interactions between curcumin and Cu(II) in methanol and the SDS micellar solution are explored in Chapter 3. Curcumin exists in two tautomeric forms, keto-enol and diketo form, similar to other β-diketone molecules [94–98]. The extended π-conjugation throughout curcumin stabilises the planar keto-enol structure, which results in an UV-visible absorption peak around 420 nm [80, 99]. In contrast, the diketo tautomer of curcumin exhibits an absorption peak around 340 nm [80]. The relatively lower energy of the absorption peak of keto-enol tautomer is indicative of the more extended π-conjugation compared with diketo tautomer of curcumin. The strongly allowed $\pi - \pi^*$ transition gives rise to a high molar extinction coefficient of 30 000 – 70 000 $\mathrm{M^{-1}\,cm^{-1}}$ at the absorption peak in water, methanol or ethanol [17]. Although curcumin is non-fluorescent in water due to effective fluorescence quenching by water, it has a fluorescence quantum yield of 2 – 10 % in organic solvents, lipid membranes, micellar solutions [17, 18, 80, 87]. The high efficiency in quenching the fluorescence of curcumin by Cu(II) ions indicates a strong interaction. The complexation constants for the formation of the 1:1, K_1, and 1:2, K_2, Cu(II)−Curcumin complexes have been determined by quantifying the fluorescence quenching of curcumin as a function of Cu(II) concentration. Furthermore, time-resolved transient absorp-

tion spectra of curcumin and the Cu(II)−Curcumin complexes show a combination of stimulated emission and excited state absorption (ESA). In particular, the ESA kinetics of curcumin in methanol and the SDS micelles show a decay component with a time constant of 60 – 125 ps, consistent with the ESIHT of curcumin. In contrast, the ESA kinetics of Cu(II)−Curcumin complexes exhibit a sharp rise followed by a fast decay with a time constant of approximately 1 ps. The ESA kinetics of curcumin and Cu(II)−Curcumin complexes are vastly different. This difference is attributable to the efficient energy transfer from excited-state curcumin to Cu(II) ion due to the strong interaction between Cu(II) and curcumin.

Chapter 4 shows the behaviour of curcumin in the presence of Cu(II) in methanol, acetonitrile and the SDS micellar solution. In contrast to the stable Cu(II)−Curcumin complexes in methanol and SDS micelles presented in Chapter 3, the Cu(II)−Curcumin complexes decomposes readily in acetonitrile and in SDS micellar solution in the presence of ascorbic acid. While curcumin interacts strongly with Cu(II), a weak association between curcumin and Cu(I) is observed. In addition, the UV-visible absorption results of the Cu(II)−Curcumin complexes in a reducing environment show a monotonic decrease as a function of time. The decay in absorbance is consistent with the decomposition of curcumin as a result of the reduction of Cu(II) to Cu(I). Furthermore, the decomposition of curcumin accompanied by the reduction of Cu(II) to Cu(I) is also observed using mass spectrometry and high performance liquid chromatography.

Investigations on the keto-enol tautomerisation of curcumin using nuclear magnetic resonance (NMR) spectroscopy are presented in Chapter 5. There are two key differences between the keto-enol and diketo tautomers of curcumin, namely the hybridisation of the carbon at the α position (C_α) and the intramolecular hydrogen bond of the keto-enol moiety. First, the hybridisation of C_α is sp^2 in the keto-enol tautomer while sp^3 hybridisation is present in the diketo tautomer. Second, there is intramolecular hydrogen bonding in the keto-enol tautomer, which is absent in the diketo tautomer [10, 96, 97, 100]. As a consequence of the sp^2 hybridisation and the intramolecular hydrogen bonding of the keto-enol tautomer, the π-conjugation of curcumin is more extended than that of the diketo tautomer. The decrease in the NMR peak corresponding to the hydrogen at the C_α as a function of time signifies a successful hydrogen-deuterium exchange. It is important to note that tautomerisation is the rate limiting

step of the deuteration at C_α. Therefore, the rate of tautomerisation is inferred from the rate of deuteration at the C_α of curcumin. Rate constants of the tautomerisation of curcumin in methanol, D_2O/acetone and D_2O/acetonitrile were determined at several temperatures. Analyses of the temperature dependence of the rate constants using the Arrhenius equation reveal the activation energy (E_a) of tautomerisation of curcumin for the first time in these solvents. The difference between the E_a of tautomerisation of curcumin in methanol, D_2O/acetone and D_2O/acetonitrile is due to the catalytic effect of D_2O.

Chapter 6 describes a one-step nanoprecipitation method to prepare curcumin-encapsulated polyester nanoparticles (Cur-polyester NP). Cur-polyester NP of less than 100 nm in diameter with a negatively charged surface are prepared with three biodegradable polyesters, namely polylactate (PLA), PLGA and PCL. The resulting Cur-polyester NP, namely Cur-PLA NP, Cur-PLGA NP and Cur-PCL NP, enhance the stability, solubility and fluorescence quantum yield of curcumin in water. The improvement in the stability of curcumin is attributable to the lack of interaction between the encapsulated curcumin and water. The fluorescence quantum yield of Cur-polyester NP is comparable to those of curcumin in organic solvents, indicating that the polyester nanoparticles are capable of encapsulating curcumin in their hydrophobic regions. Furthermore, the results from femtosecond time-resolved fluorescence upconversion spectroscopy reveal not only that there is a decrease in the signal amplitude corresponding to solvent reorganisation of the excited state of curcumin, but also a lack of deuterium isotope effect in the fluorescence lifetime of Cur-polyester NP compared with curcumin in micellar systems. These results indicate that curcumin is encapsulated within the hydrophobic region of the polyester nanoparticles where water is excluded. Therefore, the stability of curcumin is greatly improved due to effective segregation from water molecules by polyester nanoparticles.

1.4 References

(1) Sa, G.; Das, T. Anti-Cancer Effects of Curcumin: Cycle of Life and Death. *Cell Division* **2008**, *3*, 1–14.

(2) Ammon, H. P. T.; Wahl, M. A. Pharmacology of *Curcuma Longa*. *Planta Med.* **1991**, *57*, 1–7.

(3) Mishra, S.; Palanivelu, K. The Effect of Curcumin (Turmeric) on Alzheimer's Disease: An Overview. *Ann. Indian Acad. Neurol.* **2008**, *11*, 13–19.

(4) Vogel, E.; Pelletier, S. Curcumin - Biological and Medicinal Properties. *J. Pharm.* **1815**, *2*, 50–54.

(5) Kiuchi, F.; Goto, Y.; Sugimoto, N.; Akao, N.; Kondo, K.; Tsuda, Y. Nematocidal Activity of Turmeric - Synergistic Action of Curcuminoids. *Chem. Pharm. Bull.* **1993**, *41*, 1640–1643.

(6) Payton, F.; Sandusky, P.; Alworth, W. L. NMR Study of the Solution Structure of Curcumin. *J. Nat. Prod.* **2007**, *70*, 143–146.

(7) Hegge, A. B.; Bruzell, E.; Kristensen, S.; Tønnesen, H. Photoinactivation of Staphylococcus Epidermidis Biofilms and Suspensions by the Hydrophobic Photosensitizer Curcumin - Effect of Selected Nanocarrier: Studies on Curcumin nnd Curcuminoides XLVII. *Eur. J. Pharm. Sci.* **2012**, *47*, 65–74.

(8) Park, K.; Lee, J.-H. Photosensitizer Effect of Curcumin on UVB-Irradiated HaCaT Cells through Activation of Caspase Pathways. *Oncol. Rep.* **2007**, *17*, 537–540.

(9) Detty, M. R.; Gibson, S. L.; Wagner, S. J. Current Clinical and Preclinical Photosensitizers for Use in Photodynamic Therapy. *J. Med. Chem.* **2004**, *47*, 3897–3915.

(10) Adhikary, R.; Mukherjee, P.; Kee, T. W.; Petrich, J. W. Excited-State Intramolecular Hydrogen Atom Transfer and Solvation Dynamics of the Medicinal Pigment Curcumin. *J. Phys. Chem. B* **2009**, *113*, 5255–5261.

(11) Adhikary, R.; Carlson, P. J.; Kee, T. W.; Petrich, J. W. Excited-State Intramolecular Hydrogen Atom Transfer of Curcumin in Surfactant Micelles. *J. Phys. Chem. B* **2010**, *114*, 2997–3004.

(12) Khopde, S. M.; Indira Priyadarsini, K.; Palit, D. K.; Mukherjee, T. Effect of Solvent on the Excited-State Photophysical Properties of Curcumin. *Photochem. Photobiol.* **2000**, *72*, 625–631.

(13) Nardo, L.; Andreoni, A.; Másson, M.; Haukvik, T.; Tønnesen, H. H. Studies on Curcumin and Curcuminoids. XXXIX. Photophysical Properties of Bisdemethoxycurcumin. *J. Fluorescence* **2011**, *21*, 627–635.

(14) Taşcioğlu, S. Micellar Solutions as Reaction Media. *Tetrahedron* **1996**, *52*, 11113–11152.

(15) Iwunze, M. O. Binding and Distribution Characteristics of Curcumin Solubilized in CTAB Micelle. *J. Mol. Liq.* **2004**, *111*, 161–165.

(16) Tønnesen, H. H. Solubility, Chemical and Photochemical Stability of Curcumin in Surfactant Solutions. Studies of Curcumin and Curcuminolds, XXVIII. *Pharmazie* **2002**, *57*, 820–824.

(17) Wang, Z. F.; Leung, M. H. M.; Kee, T. W.; English, D. S. The Role of Charge in the Surfactant-Assisted Stabilization of the Natural Product Curcumin. *Langmuir* **2010**, *26*, 5520–5526.

(18) Leung, M. H. M.; Colangelo, H.; Kee, T. W. Encapsulation of Curcumin in Cationic Micelles Suppresses Alkaline Hydrolysis. *Langmuir* **2008**, *24*, 5672–5675.

(19) Lantz, R. C.; Chen, G. J.; Solyom, A. M.; Jolad, S. D.; Timmermann, B. N. The Effect of Turmeric Extracts on Inflammatory Mediator Production. *Phytomedicine* **2005**, *12*, 445–452.

(20) Gopinath, D.; Ahmed, M. R.; Gomathi, K.; Chitra, K.; Sehgal, P. K.; Jayakumar, R. Dermal Wound Healing Processes with Curcumin Incorporated Collagen Films. *Biomaterials* **2004**, *25*, 1911–1917.

(21) Jagetia, G. C.; Rajanikant, G. K. Curcumin Treatment Enhances the Repair and Regeneration of Wounds in Mice Exposed to Hemibody γ-Irradiation. *Plast. Reconstr. Surg.* **2005**, *115*, 515–528.

(22) Jagetia, G. C.; Rajanikant, G. K. Acceleration of Wound Repair by Curcumin in the Excision Wound of Mice Exposed to Different Doses of Fractionated γ Radiation. *Int. Wound J.* **2012**, *9*, 76–92.

(23) Legeza, V.; Galenko-Yaroshevskii, V.; Zinov'ev, E.; Paramonov, B.; Kreichman, G.; Turkovskii, I.; Gumenyuk, E.; Karnovich, A.; Khripunov, A. Effects of New Wound Dressings on Healing of Thermal Burns of the Skin in Acute Radiation Disease. *Bull. Exp. Biol. Med.* **2004**, *138*, 311–315.

(24) Aggarwal, B. B.; Kumar, A.; Bharti, A. C. Anticancer Potential of Curcumin: Preclinical and Clinical Studies. *Anticancer Res.* **2003**, *23*, 363–398.

(25) Suresh, M. V.; Wagner, M. C.; Rosania, G. R.; Stringer, K. A.; Min, K. A.; Risler, L.; Shen, D. D.; Georges, G. E.; Reddy, A. T.; Parkkinen, J.; Reddy, R. C. Pulmonary Administration of Water-Soluble Curcumin Complex Reduces Severity of Acute Lung Injury. *Am. J. Respir. Cell Mol. Biol.* **2012**, *47*, 280–287.

(26) Park, J. H.; Kim, H. A.; Park, J. H.; Lee, M. Amphiphilic Peptide Carrier for the Combined Delivery of Curcumin and Plasmid DNA into the Lungs. *Biomaterials* **2012**, *33*, 6542–6550.

(27) Cartiera, M. S.; Ferreira, E. C.; Caputo, C.; Egan, M. E.; Caplan, M. J.; Saltzman, W. M. Partial Correction of Cystic Fibrosis Defects with PLGA Nanoparticles Encapsulating Curcumin. *Mol. Pharmaceutics* **2010**, *7*, 86–93.

(28) Egan, M. E.; Pearson, M.; Weiner, S. A.; Rajendran, V.; Rubin, D.; Glockner-Pagel, J.; Canny, S.; Du, K.; Lukacs, G. L.; Caplan, M. J. Curcumin, a Major Constituent of Turmeric, Corrects Cystic Fibrosis Defects. *Science* **2004**, *304*, 600–602.

(29) Zeitlin, P. Can Curcumin Cure Cystic Fibrosis? *N. Engl. J. Med.* **2004**, *351*, 606–608.

(30) Lim, G. P.; Chu, T.; Yang, F. S.; Beech, W.; Frautschy, S. A.; Cole, G. M. The Curry Spice Curcumin Reduces Oxidative Damage and Amyloid Pathology in an Alzheimer Transgenic Mouse. *J. Neurosci.* **2001**, *21*, 8370–8377.

(31) Ono, K.; Hasegawa, K.; Naiki, H.; Yamada, M. Curcumin has Potent Anti-Amyloidogenic Effects for Alzheimer's β-Amyloid Fibrils *in Vitro*. *J. Neurosci. Res.* **2004**, *75*, 742–750.

(32) Yang, F. S.; Lim, G. P.; Begum, A. N.; Ubeda, O. J.; Simmons, M. R.; Ambegaokar, S. S.; Chen, P. P.; Kayed, R.; Glabe, C. G.; Frautschy, S. A.; Cole, G. M. Curcumin Inhibits Formation of Amyloid β Oligomers and Fibrils, Binds Plaques, and Reduces Amyloid *in Vivo*. *J. Biol. Chem.* **2005**, *280*, 5892–5901.

(33) Jiang, T.; Zhi, X.-L.; Zhang, Y.-H.; Pan, L.-F.; Zhou, P. Inhibitory Effect of Curcumin on the Al(III)-Induced Aβ_{42} Aggregation and Neurotoxicity *in Vitro*. *BBA-Mol. Basis Dis.* **2012**, *1822*, 1207–1215.

(34) Hatcher, H.; Planalp, R.; Cho, J.; Tortia, F. M.; Torti, S. V. Curcumin: From Ancient Medicine to Current Clinical Trials. *Cell. Mol. Life Sci.* **2008**, *65*, 1631–1652.

(35) Anand, P.; Sundaram, C.; Jhurani, S.; Kunnumakkara, A. B.; Aggarwal, B. B. Curcumin and Cancer: An"Old-Age" Disease with an"Age-Old" Solution. *Cancer Lett.* **2008**, *267*, 133–164.

(36) Huang, M. T.; Lou, Y. R.; Ma, W.; Newmark, H. L.; Reuhl, K. R.; Conney, A. H. Inhibitory Effects of Dietary Curcumin on Forestomach, Duodenal, and Colon Carcinogenesis in Mice. *Cancer Res.* **1994**, *54*, 5841–5847.

(37) Rao, C. V.; Rivenson, A.; Simi, B.; Reddy, B. S. Chemoprevention of Colon Carcinogenesis by Dietary Curcumin, a Naturally-Occurring Plant Phenolic Compound. *Cancer Res.* **1995**, *55*, 259–266.

(38) Sharma, R. A.; Gescher, A. J.; Steward, W. P. Curcumin: The Story so Far. *Eur. J. Cancer* **2005**, *41*, 1955–1968.

(39) Caruso, F.; Rossi, M.; Benson, A.; Opazo, C.; Freedman, D.; Monti, E.; Gariboldi, M. B.; Shaulky, J.; Marchetti, F.; Pettinari, R.; Pettinari, C. Ruthenium-Arene Complexes of Curcumin: X-Ray and Density Functional Theory Structure, Synthesis, and Spectroscopic Characterization, *in Vitro* Antitumor Activity, and DNA Docking Studies of (p-Cymene)Ru(Curcuminato)Chloro. *J. Med. Chem.* **2012**, *55*, 1072–1081.

(40) Lao, C. D.; Ruffin, M. T. t.; Normolle, D.; Heath, D. D.; Murray, S. I.; Bailey, J. M.; Boggs, M. E.; Crowell, J.; Rock, C. L.; Brenner, D. E. Dose Escalation of a Curcuminoid Formulation. *BMC Complem. Altern. M.* **2006**, *6*, 10.

(41) Baum, L.; Ng, A. Curcumin Interaction with Copper and Iron Suggests One Possible Mechanism of Action in Alzheimer's Disease Animal Models. *J. Alzheimers Dis.* **2004**, *6*, 367–377.

(42) Yoshino, M.; Haneda, M.; Naruse, M.; Htay, H. H.; Tsubouchi, R.; Qiao, S. L.; Li, W. H.; Murakami, K.; Yokochi, T. Prooxidant Activity of Curcumin: Copper-Dependent Formation of 8-Hydroxy-2-Deoxyguanosine in DNA and Induction of Apoptotic Cell Death. *Toxicol. in Vitro* **2004**, *18*, 783–789.

(43) Ahsan, H.; Hadi, S. M. Strand Scission in DNA Induced by Curcumin in the Presence of Cu(II). *Cancer Lett.* **1998**, *124*, 23–30.

(44) Ahsan, H.; Parveen, N.; Khan, N. U.; Hadi, S. M. Pro-Oxidant, Anti-Oxidant and Cleavage Activities on DNA of Curcumin and Its Derivatives Demethoxycurcumin and Bisdemethoxycurcumin. *Chem. Biol. Interact.* **1999**, *121*, 161–175.

(45) Lou, J. R.; Zhang, X.-X.; Zheng, J.; Ding, W.-Q. Transient Metals Enhance Cytotoxicity of Curcumin: Potential Involvement of the NFκB and mTOR Signaling Pathways. *Anticancer Res.* **2010**, *30*, 3249–3255.

(46) Sakano, K.; Kawanishi, S. Metal-Mediated DNA Damage Induced by Curcumin in the Presence of Human Cytochrome P450 Isozymes. *Arch. Biochem. Biophys.* **2002**, *405*, 223–230.

(47) Deng, S.-L.; Chen, W.-F.; Zhou, B.; Yang, L.; Liu, Z.-L. Protective Effects of Curcumin and Its Analogues against Free Radical-Induced Oxidative Haemolysis of Human Red Blood Cells. *Food Chem.* **2006**, *98*, 112–119.

(48) Chen, W.-F.; Deng, S.-L.; Zhou, B.; Yang, L.; Liu, Z.-L. Curcumin and Its Analogues as Potent Inhibitors of Low Density Lipoprotein Oxidation: H-Atom Abstraction from the Phenolic Groups and Possible Involvement of the 4-Hydroxy-3-Methoxyphenyl Groups. *Free Radic. Biol. Med.* **2006**, *40*, 526–535.

(49) Barik, A.; Mishra, B.; Shen, L.; Mohan, H.; Kadam, R. M.; Dutta, S.; Zhang, H. Y.; Priyadarsini, K. I. Evaluation of a New Copper(II)-Curcumin Complex as Superoxide Dismutase Mimic and Its Free Radical Reactions. *Free Radic. Biol. Med.* **2005**, *39*, 811–822.

(50) Serpi, C.; Stanic, Z.; Girousi, S. Electroanalytical Study of the Interaction between dsDNA and Curcumin in the Presence of Copper(II). *Talanta* **2010**, *81*, 1731–1734.

(51) Nair, J.; Strand, S.; Frank, N.; Knauft, J.; Wesch, H.; Galle, P. R.; Bartsch, H. Apoptosis and Age-Dependant Induction of Nuclear and Mitochondrial Etheno-DNA Adducts in Long-Evans Cinnamon (LEC) Rats: Enhanced DNA Damage by Dietary Curcumin upon Copper Accumulation. *Carcinogenesis* **2005**, *26*, 1307–1315.

(52) Sahu, S. C.; Washington, M. C. Effect of Ascorbic-Acid and Curcumin on Quercetin-Induced Nuclear-DNA Damage, Lipid-Peroxidation and Protein-Degradation. *Cancer Lett.* **1992**, *63*, 237–241.

(53) Bush, J. A.; Cheung, K. J. J.; Li, G. Curcumin Induces Apoptosis in Human Melanoma Cells through a Fas Receptor/Caspase-8 Pathway Independent of p53. *Exp. Cell Res.* **2001**, *271*, 305–314.

(54) Jaiswal, A. S.; Marlow, B. P.; Gupta, N.; Narayan, S. β-Catenin-Mediated Transactivation and Cell - Cell Adhesion Pathways are Important in Curcumin (diferuylmethane)-Induced Growth Arrest and Apoptosis in Colon Cancer Cells. *Oncogene* **2002**, *21*, 8414–8427.

(55) Nagai, S.; Kurimoto, M.; Washiyama, K.; Hirashima, Y.; Kumanishi, T.; Endo, S. Inhibition of Cellular Proliferation and Induction of Apoptosis by Curcumin in Human Malignant Astrocytoma Cell Lines. *J. Neurooncol.* **2005**, *74*, 105–111.

(56) Yanagisawa, D.; Shirai, N.; Amatsubo, T.; Taguchi, H.; Hirao, K.; Urushitani, M.; Morikawa, S.; Inubushi, T.; Kato, M.; Kato, F.; Morino, K.; Kimura, H.; Nakano, I.; Yoshida, C.; Okada, T.; Sano, M.; Wada, Y.; Wada, K.-n.; Yamamoto, A.; Tooyama, I. Relationship between the Tautomeric Structures of Curcumin Derivatives and Their Aβ-Binding Activities in the Context of Therapies for Alzheimer's Disease. *Biomaterials* **2010**, *31*, 4179–4185.

(57) Kaminaga, Y.; Nagatsu, A.; Akiyama, T.; Sugimoto, N.; Yamazaki, T.; Maitani, T.; Mizukami, H. Production of Unnatural Glucosides of Curcumin with Drastically Enhanced Water Solubility by Cell Suspension Cultures of Catharanthus Roseus. *FEBS Lett.* **2003**, *555*, 311–316.

(58) Letchford, K.; Liggins, R.; Burt, H. Solubilization of Hydrophobic Drugs by Methoxy Poly(Ethylene Glycol)-Block-Polycaprolactone Diblock Copolymer Micelles: Theoretical and Experimental Data and Correlations. *J. Pharm. Sci.* **2008**, *97*, 1179–1190.

(59) Wang, Y. J.; Pan, M. H.; Cheng, A. L.; Lin, L. I.; Ho, Y. S.; Hsieh, C. Y.; Lin, J. K. Stability of Curcumin in Buffer Solutions and Characterization of Its Degradation Products. *J. Pharm. Biomed. Anal.* **1997**, *15*, 1867–1876.

(60) Tsai, Y.-M.; Chang-Liao, W.-L.; Chien, C.-F.; Lin, L.-C.; Tsai, T.-H. Effect of Polymer Molecular Weight on Relative Oral Bioavailability of Curcumin. *Int. J. Nanomedicine* **2012**, *7*, 2957–2966.

(61) Tsai, Y.-M.; Chien, C.-F.; Lin, L.-C.; Tsai, T.-H. Curcumin and its Nano-Formulation: The Kinetics of Tissue Distribution and Blood-Brain Barrier Penetration. *Int. J. Pharm.* **2011**, *416*, 331–338.

(62) Mohanty, C.; Acharya, S.; Mohanty, A. K.; Dilnawaz, F.; Sahoo, S. K. Curcumin-Encapsulated MePEG/PCL Diblock Copolymeric Micelles: A

Novel Controlled Delivery Vehicle for Cancer Therapy. *Nanomedicine* **2010**, *5*, 433–449.

(63) Khalil, N. M.; do Nascimento, T. C. F.; Casa, D. M.; Dalmolin, L. F.; de Mattos, A. C.; Hoss, I.; Romano, M. A.; Mainardes, R. M. Pharmacokinetics of Curcumin-Loaded PLGA and PLGA-PEG Blend Nanoparticles after Oral Administration in Rats. *Colloids Surf. B* **2013**, *101*, 353–360.

(64) Bisht, S.; Feldmann, G.; Soni, S.; Ravi, R.; Karikar, C.; Maitra, A.; Maitra, A. Polymeric Nanoparticle-Encapsulated Curcumin ("Nanocurcumin"): A Novel Strategy for Human Cancer Therapy. *J. Nanobiotechnology* **2007**, *5*, 18.

(65) Leung, M. H. M.; Kee, T. W. Effective Stabilization of Curcumin by Association to Plasma Proteins: Human Serum Albumin and Fibrinogen. *Langmuir* **2009**, *25*, 5773–5777.

(66) Barik, A.; Priyadarsini, K. I.; Mohan, H. Photophysical Studies on Binding of Curcumin to Bovine Serum Albumin. *Photochem. Photobiol.* **2003**, *77*, 597–603.

(67) Bourassa, P.; Kanakis, C. D.; Tarantilis, P.; Pollissiou, M. G.; Tajmir-Riahi, H. A. Resveratrol, Genistein, and Curcumin Bind Bovine Serum Albumin. *J. Phys. Chem. B* **2010**, *114*, 3348–3354.

(68) Harada, T.; Giorgio, L.; Harris, T. J.; Pham, D.-T.; Ngo, H. T.; Need, E. F.; Coventry, B. J.; Lincoln, S. F.; Easton, C. J.; Buchanan, G.; Kee, T. W. Diamide Linked γ-Cyclodextrin Dimers as Molecular-Scale Delivery Systems for the Medicinal Pigment Curcumin to Prostate Cancer Cells. *Mol. Pharmaceutics* **2013**, *10*, 4481–4490.

(69) Harada, T.; Pham, D.-T.; Leung, M. H. M.; Ngo, H. T.; Lincoln, S. F.; Easton, C. J.; Kee, T. W. Cooperative Binding and Stabilization of the Medicinal Pigment Curcumin by Diamide Linked γ-Cyclodextrin Dimers: A Spectroscopic Characterization. *J. Phys. Chem. B* **2011**, *115*, 1268–1274.

(70) Yadav, V. R.; Prasad, S.; Kannappan, R.; Ravindran, J.; Chaturvedi, M. M.; Vaahtera, L.; Parkkinen, J.; Aggarwal, B. B. Cyclodextrin-Complexed Curcumin Exhibits Anti-Inflammatory and Antiproliferative Activities Superior

to Those of Curcumin through Higher Cellular Uptake. *Biochem. Pharmacol.* **2010**, *80*, 1021–1032.

(71) Wennerström, H.; Lindman, B. Micelles. Physical Chemistry of Surfactant Association. *Phys. Rep.* **1979**, *52*, 1–86.

(72) Nagarajan, R.; Ruckenstein, E. Theory of Surfactant Self-Assembly: A Predictive Molecular Thermodynamic Approach. *Langmuir* **1991**, *7*, 2934–2969.

(73) Chernenko, T.; Matthaeus, C.; Milane, L.; Quintero, L.; Amiji, M.; Diem, M. Label-free Raman Spectral Imaging of Intracellular Delivery and Degradation of Polymeric Nanoparticle Systems. *ACS Nano* **2009**, *3*, 3552–3559.

(74) Musyanovych, A.; Schmitz-Wienke, J.; Mailaender, V.; Walther, P.; Landfester, K. Preparation of Biodegradable Polymer Nanoparticles by Miniemulsion Technique and Their Cell Interactions. *Macromol. Biosci.* **2008**, *8*, 127–139.

(75) Verderio, P.; Bonetti, P.; Colombo, M.; Pandolfi, L.; Prosperi, D. Intracellular Drug Release from Curcumin-Loaded PLGA Nanoparticles Induces G2/M Block in Breast Cancer Cells. *Biomacromolecules* **2013**, *14*, 672–682.

(76) Mukerjee, A.; Vishwanatha, J. K. Formulation, Characterization and Evaluation of Curcumin-Loaded PLGA Nanospheres for Cancer Therapy. *Anticancer Res.* **2009**, *29*, 3867–3875.

(77) Yallapu, M. M.; Jaggi, M.; Chauhan, S. C. β-Cyclodextrin-Curcumin Self-Assembly Enhances Curcumin Delivery in Prostate Cancer Cells. *Colloids Surf., B.* **2010**, *79*, 113–125.

(78) Chereddy, K. K.; Coco, R.; Memvanga, P. B.; Ucakar, B.; des Rieux, A.; Vandermeulen, G.; Preat, V. Combined Effect of PLGA and Curcumin on Wound Healing Activity. *J. Controlled Release* **2013**, *171*, 208–215.

(79) Devadasu, V. R.; Wadsworth, R. M.; Kumar, M. N. V. R. Protective Effects of Nanoparticulate Coenzyme Q10 and Curcumin on Inflammatory Markers and Lipid Metabolism in Streptozotocin-Induced Diabetic Rats: A Possible Remedy to Diabetic Complications. *Drug Deliv. and Transl. Res.* **2011**, *1*, 448–455.

(80) Chignell, C. F.; Bilskj, P.; Reszka, K. J.; Motten, A. G.; Sik, R. H.; Dahl, T. A. Spectral and Photochemical Properties of Curcumin. *Photochem. Photobiol.* **1994**, *59*, 295–302.

(81) Bernabe-Pineda, M.; Ramirez-Silva, M. T.; Romero-Romo, M.; Gonzadlez-Vergara, E.; Rojas-Hernandez, A. Determination of Acidity Constants of Curcumin in Aqueous Solution and Apparent Rate Constant of Its Decomposition. *Spectrochim. Acta A* **2004**, *60*, 1091–1097.

(82) Tønnesen, H. H.; Karlsen, J. Studies on Curcumin and Curcuminoids. VI. Kinetics of Curcumin Degradation in Aqueous Solution. *Z. Lebensm. Unters. Forsch.* **1985**, *180*, 402–404.

(83) Tønnesen, H. H.; Másson, M.; Loftsson, T. Studies of Curcumin and Curcuminoids. XXVII. Cyclodextrin Complexation: Solubility, Chemical and Photochemical Stability. *Int. J. Pharm.* **2002**, *244*, 127–135.

(84) Beer, A. Bestimmung der Absorption des rothen Lichts in farbigen Flüssigkeiten. *Ann. der Physik* **1852**, *162*, 78–88.

(85) Williams, A. T. R.; Winfield, S. A.; Miller, J. N. Elative Fluorescence Quantum Yields Using a Computer-Controlled Luminescence Spectrometer. *Analyst* **1983**, *108*, 1067–1071.

(86) Fery-Forgues, S.; Lavabre, D. Are Fluorescence Quantum Yields So Tricky to Measure? A Demonstration Using Familiar Stationery Products. *J. Chem. Educ.* **1999**, *76*, 1260–1264.

(87) Bong, P.-H. Spectral and Photophysical Behaviors of Curcumin and Curcuminoids. *Bull. Korean Chem. Soc.* **2000**, *21*, 81–86.

(88) Jasim, F.; Ali, F. A Novel and Rapid Method for the Spectrofluorometric Determination of Curcumin in Curcumin Spices and Flavors. *Microchem. J.* **1992**, *46*, Proceedings of the V Italo-Hungarian Symposium on Spectrochemistry: Quality Control and Assurance in Life Sciences, 209–214.

(89) Kato, H., Singh, S. C., Zeng, H. B., Guo, C., Eds.; John Wiley & Sons: 2012; Chapter 8. Size Determination of Nanoparticles by Dynamic Light Scattering, pp 535–554.

(90) Yin, L. *Nanotechnology Research Methods for Foods and Bioproducts*, Padua, G. W., Wang, Q., Eds.; Wiley-Blackwell: 2012; Chapter 8. Dynamic Light Scattering, pp 145–161.

(91) Kirby, B. J.; Hasselbrink, E. F. Zeta Potential of Microfluidic Substrates: 1. Theory, Experimental Techniques, and Effects on Separations. *Electrophoresis* **2004**, *25*, 187–202.

(92) Henry, D. C. The Cataphoresis of Suspended Particles. Part I. The Equation of Cataphoresis. *Proc Roy Soc (London) Ser A* **1931**, *133*, 106–129.

(93) Deshiikan, S. R.; Papadopoulos, K. D. Modified Booth Equation for the Calculation of Zeta Potential. *Colloid Polym. Sci.* **1998**, *276*, 117–124.

(94) Allen, G.; Dwek, R. A. An N.M.R. Study of Keto-Enol Tautomerism in β-Diketones. *J. Chem. Soc. B* **1966**, 161–163.

(95) Emsley, J. The Composition, Structure and Hydrogen Bonding of the β-Diketones. *Struct. Bond.* **1984**, *57*, 147–199.

(96) Kawaguchi, S. Variety in the Coordination Modes of β-Dicarbonyl Compounds in Metal Complexes. *Coord. Chem. Rev.* **1986**, *70*, 51–84.

(97) Emsley, J.; Freeman, N. J. β-Diketone Interactions: Part 5. Solvent Effects on the Keto$\rightleftharpoons$Enol Equilibrium. *J. Mol. Struct.* **1987**, *161*, 193–204.

(98) Nichols, M. A.; Waner, M. J. Kinetic and Mechanistic Studies of the Deuterium Exchange in Classical Keto-Enol Tautomeric Equilibrium Reactions. *J. Chem. Educ.* **2010**, *87*, 952–955.

(99) Kolev, T. M.; Velcheva, E. A.; Stamboliyska, B. A.; Spiteller, M. DFT and Experimental Studies of the Structure and Vibrational Spectra of Curcumin. *Int. J. Quantum Chem.* **2005**, *102*, 1069–1079.

(100) Ghosh, R.; Mondal, J. A.; Palit, D. K. Ultrafast Dynamics of the Excited States of Curcumin in Solution. *J. Phys. Chem. B* **2010**, *114*, 12129–12143.

CHAPTER 2

ULTRAFAST LASER AND TIME-RESOLVED SPECTROSCOPY

2.1 Titanium Sapphire Laser

Titanium sapphire lasers use a titanium-doped sapphire crystal (Ti:sapphire) as a gain medium for laser amplification. In the crystal, a concentration of 0.1 – 0.5 wt% of titanium(III) oxide (Ti_2O_3) is doped into a crystal of Al_2O_3 [1, 2]. The doped Ti^{3+} ions, which replace some of the Al^{3+} ions in the matrix, are responsible for the lasing action. Titanium has an electronic configuration of $1s^2\ 2s^2\ 2p^6\ 3s^2\ 3p^6\ 3d^2\ 4s^2$. The three outermost electrons are involved in ionic bonding with oxygen in the Ti:Al_2O_3 matrix, resulting in the Ti^{3+} ion [2]. Figure 2.1 illustrates the excitation from the lowest vibrational state of the ground state ($^2\mathbf{T}_2$) to the excited state ($^2\mathbf{E}$) of Ti^{3+}, which is followed by rapid internal conversion to the lowest vibrational state of the $^2\mathbf{E}$ [1–3]. The lasing process occurs from the lowest vibrational state of the $^2\mathbf{E}$ to the vibrational states of the $^2\mathbf{T}_2$ state due to the large stimulated emission cross section of Ti^{3+}, even though the lifetime of the $^2\mathbf{E}$ is relatively short (3.8 µs) [1]. It is important to note that the $^2\mathbf{T}_2$ and $^2\mathbf{E}$ states of Ti^{3+} have a broad sequence of overlapping vibrational states and there are no other *d*-state energy levels above $^2\mathbf{E}$. As a result, this particular energy-state configuration of Ti^{3+} eliminates excited state absorption, which is a phenomenon that can reduce the efficiency and tunable range of the laser [1, 2].

The lasing property of Ti:sapphire was first demonstrated in 1986 and since then it is the most widely used solid state laser for two main reasons [3]. First, Ti:sapphire has a broad pump absorption spectrum from 400 – 600 nm. Although there is a wide range of possible pump wavelengths for Ti:sapphire, the blue and green in the visible region

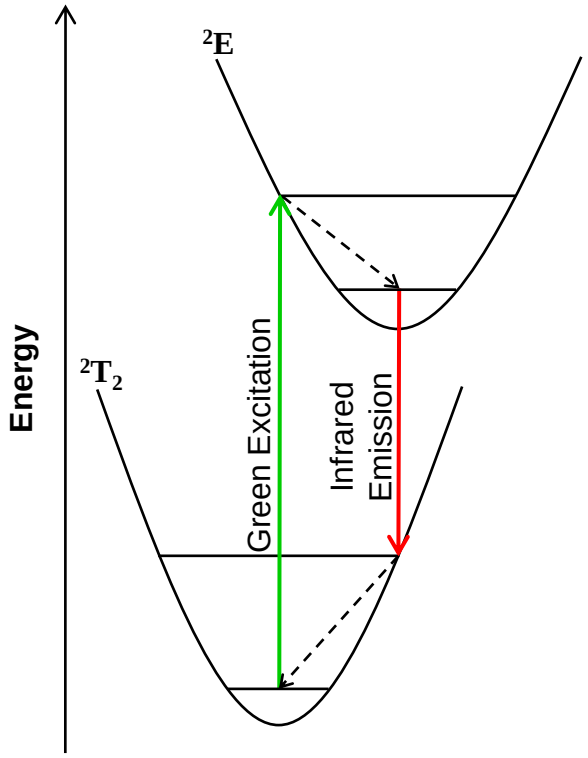

Figure 2.1. The energy diagram of Ti^{3+} ion. The green arrow represents excitation from the ground state, $^2T_2$, to the excited state, ^2E, while the red arrow represents emission from the ^2E state back to $^2T_2$. The dashed arrows represent internal conversion between vibrational levels.

are not accessible with laser diodes. The Ti:sapphire laser, however, can be pumped with a flashlamp, but it has poor efficiency because of the mismatch between the short-lived upper laser level of the Ti:sapphire and the pulse duration from a conventional flashlamp [1, 2]. Therefore, Ti:sapphire is typically pumped with a 514-nm argon ion laser for continuous wave operation or a green laser (532 nm) based on the frequency-doubled output of a neodymium-doped gain medium, such as Nd:YVO_4, for pulsed operation [1, 2]. Second, Ti:sapphire exhibits a broad laser emission spectrum which provides a tunable wavelength range of 660 – 1180 nm [1]. The large gain-bandwidth of Ti^{3+} enables the generation of very short pulses with the maximum gain and laser efficiency at 800 nm with mode-locking techniques.

2.1.1 Mode-locking

In mode-locking lasers, the longitudinal modes are locked in phase so that they have constructive interference at certain points within the laser cavity while destructive

interference occurs elsewhere. As a result, a train of light pulses is generated and its oscillation wavelength is dependent on the gain-bandwidth of the laser medium and the longitudinal modes, which is determined by the laser cavity. Figure 2.2a shows the time dependence of the amplitude of the wave having different numbers of longitudinal modes, n, with locked phases according to

$$A(t) = E_0 \frac{sin[(2n+1)\Delta\omega\frac{t}{2}]}{sin(\Delta\omega\frac{t}{2})} \tag{2.1}$$

where $\Delta\omega$ is the frequency difference between two consecutive modes [2]. At the maximum of each pulse, the denominator of Equation (2.1) vanishes. As shown in Figure 2.2a, the first and its consecutive maximum occurs at $t_1 = 0$ and $t_2 = \frac{2\pi}{\Delta\omega}$ with

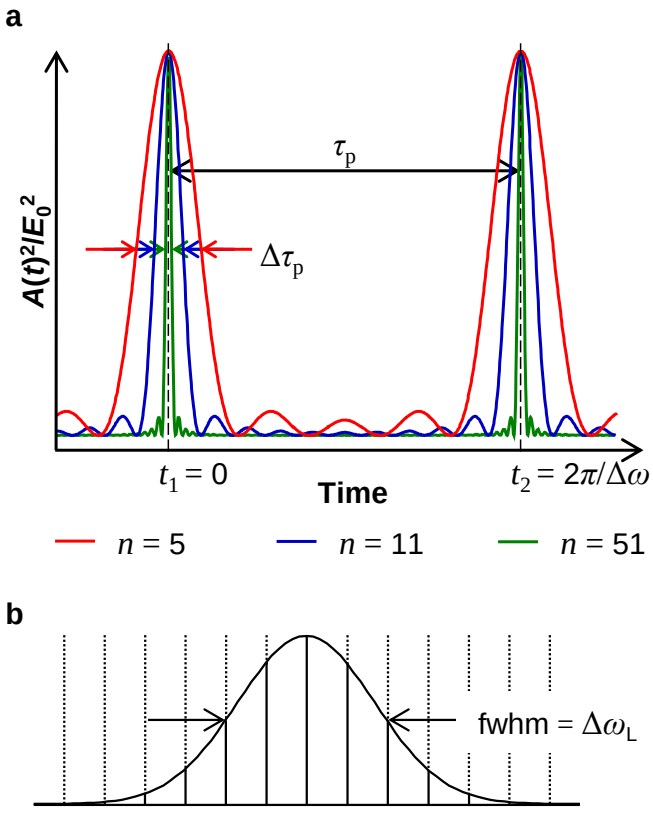

Figure 2.2. (a) Time-domain description of the amplitude of the pulse with mode-locking according to Equation (2.1) with the number of oscillating longitudinal mode of 5, 11 and 51. (b) A frequency-domain illustration of a Gaussian amplitude distribution gain-bandwidth.

τ_p as the interval between two these pulses, we obtain the following.

$$\begin{aligned}\tau_p &= t_2 - t_1 \\ &= \frac{2\pi}{\Delta\omega} - 0 \\ &= \frac{2\pi}{\Delta\omega} = \frac{1}{\Delta\upsilon} = \frac{2L}{c}\end{aligned} \tag{2.2}$$

where $\Delta\upsilon$ is the frequency separation of two adjacent longitudinal modes, L is the length of the laser cavity and c is the speed of light [2, 4]. Equation (2.2) shows that the interval between the pulses and, therefore, the repetition rate of laser are determined by the laser cavity. It is important to note that $2L$ is equal to a round trip inside the laser cavity.

As the number of longitudinal modes are increased in the mode-locking process, the pulse width ($\Delta\tau_p$) becomes narrower, as shown in Figure 2.2a. The $\Delta\tau_p$ is given as followed:

$$\Delta\tau_p = \frac{2ln2}{\pi\Delta\upsilon_L} \approx \frac{0.441}{\Delta\upsilon_L} \tag{2.3}$$

where $\Delta\upsilon_L$ is the total oscillation bandwidth, which is dependent on the gain-bandwidth, $\delta\omega_L$, of a gain medium, as shown in Figure 2.2b [2]. For lasers with a gain medium that has a relatively broad gain-bandwidth, such as Ti:sapphire lasers, the number of longitudinal modes supported within the laser cavity is on the order of 10^5 or higher. The large number of phase-locked longitudinal modes enables generation of short pulses with pico- to femtosecond pulse duration.

Mode-locking can be achieved from either active mode-locking or passive mode-locking techniques. In most mode-locked lasers, combinations of mode-locking techniques are employed to generate ultrashort pulses. Active mode-locking is a common method to generate short pulses. A modulator is included in the laser cavity which operates at the same frequency as the pulse repetition rate. For a pulsed high gain laser, a Pockels cell amplitude modulator with the cell voltage sinusoidally modulated between 0 to $\lambda/4$ is typically used [2]. For a continuous wave pumped low gain laser, mode-locking is commonly achieved using an acousto-optic modulator (AOM) placed inside the laser cavity near one of the end mirrors, as illustrated in Figure 2.3a. In addition, the AOM is orientated with its two polished faces, of which one of them

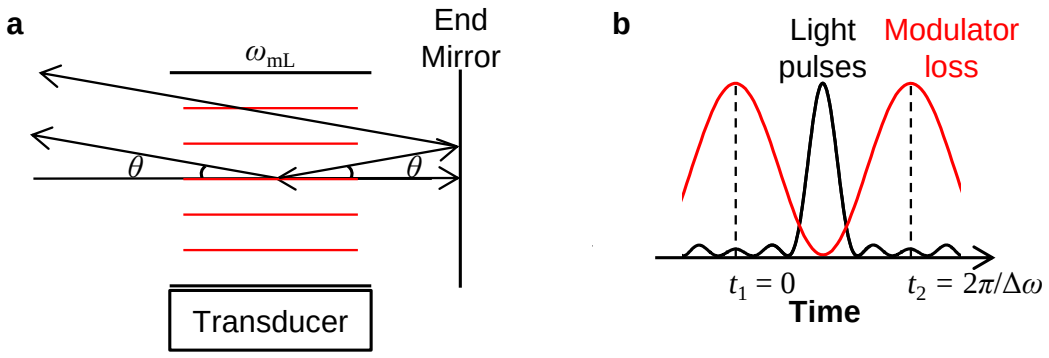

Figure 2.3. (a) A schematic diagram of the acousto-optic modulator. The red lines represent the acoustic standing-wave oscillating at a frequency of $\omega_{mL} = c/2L$ while the black arrows represent the diffracted light beams that arise at an angle of θ. (b) A time domain description of the acousto-optic modulator mode-locking with the red curve and the black curve represent the modulator loss and the light pulse, respectively. When the ω_{mL} is precisely matched with the laser cavity length, the light pulse passes through the acousto-optic modulator during minimum modulator loss when the maximum modulator loss occurs at $t = 0$ and $\frac{2\pi}{\delta\omega}$.

has a piezoelectric transducer attached, parallel to the light propagation. The acoustic wave from the transducer is reflected by its opposite face and a standing-wave is generated, which is shown as red lines in Figure 2.3a. The light beam interacts with the standing-wave, which has a deflection angle, θ, that depends on the wavelength of the light beam relative to that of the acoustic wave. Figure 2.3b illustrates the modulator loss reaches a maximum at the peak amplitude of the acoustic standing-wave, which is sinusoidally modulated in time. It is important to note that there are two maxima within one oscillation of the acoustic standing-wave occurring at $t = 0$ and $\frac{2\pi}{\delta\omega}$, which lead to a modulated loss with a frequency twice of that of the acoustic wave. In other words, for an acoustic wave oscillating at a frequency, ω_{mL}, the modulated loss occurs at a frequency of $2\omega_{mL}$. For an optimum mode-locking operation, the frequency of the modulated loss has to be matched with the repetition rate of the laser ($2\omega_{mL} = \frac{c}{2L}$) [2]. As a consequence, the transducer operates at a frequency of $\frac{c}{4L}$, which is half the frequency of the repetition rate of laser. Furthermore, when ω_{mL} is precisely matched with the cavity length, the light pulses always pass through the AOM during minimum modulator loss (Figure 2.3b). As the precise matching of ω_{mL} with the cavity length is difficult to achieve, the drive signal of the transducer is derived from the detected intensity modulation of the pulse. In other words, synchronisation between the drive

signal and the laser is achieved by a feedback mechanism and automatically adjusts ω_{mL}, which is known as regenerative mode-locking [5].

On one hand, active mode-locking is achieved by a modulator with a periodic modulation; on the other hand, passive mode-locking is achieved by the pulses themselves. Previous work has demonstrated the use of passive mode-locking of Ti:sapphire to generate short pulses [6–8]. At a sufficiently high intensity of a light beam traversing the Ti:sapphire crystal, its refractive index is influenced by the pulse intensity. The change in the refractive index of a non-linear material due to the traversing light intensity is known as the optical Kerr effect and the non-linear refractive index change is given as

$$\Delta n = n_2 I \tag{2.4}$$

where I is the intensity of the traversing light and n_2 is the non-linear index of a material [2]. Figure 2.4 shows the non-linear optical Kerr effect of the Ti:sapphire crystal where the centre of the traversing light beam has a higher intensity than its wings with a Gaussian profile. When the intensity is high, the electric field of the light beam deforms the electron cloud due to the hyper-polarisability of the Ti:sapphire crystal. As a consequence, the refractive index of the Ti:sapphire crystal becomes intensity dependent [2]. It is important to note that the refractive index increases with intensity, which is given in Equation (2.4), and the beam becomes focussed. This phenomenon is known as Kerr-induced self-focussing [9, 10]. Furthermore, the hyper-polarisability of the Ti:sapphire crystal has a response time of a few femtoseconds [2]. As a result, the non-linear optical Kerr effect is very fast and enables the generation of ultrashort

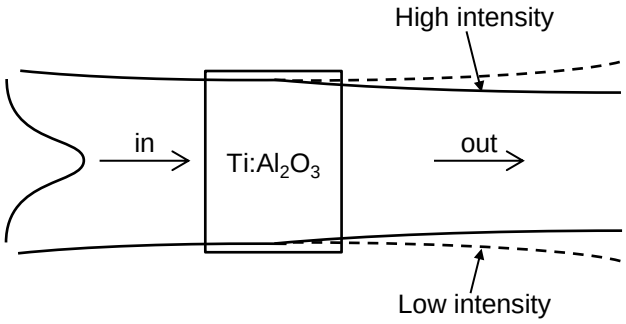

Figure 2.4. A scheme of Kerr-induced self-focussing where the light beam has a Gaussian profile. The centre of a light beam is focussed due to an increase in the refractive index, which depends on the light intensity as shown in Equation (2.4).

pulses. This type of passive mode-locking is known as the Kerr lens mode-locking. In our laser system, the Kerr lens mode-locking are employed to generate femtosecond pulses.

2.1.2 Dispersion Compensation

The large gain-bandwidth of the Ti^{3+} ions enables the generation of very short pulses with Kerr lens mode-locking. It is important to note that there are drawbacks from the non-linear effect of Ti:sapphire which are self-phase modulation (SPM) and group velocity dispersion (GVD) of the pulse. For SPM, the front and the back of the light pulse experience a changing refractive index as the pulse propagates in the laser cavity. As a result of the non-linear optical Kerr effect causing a phase shift in the light pulse, the spectrum of the pulse is broadened. In addition to SPM, GVD changes the pulse width due to differences in the velocity of different frequencies [11]. For a positive GVD or positively-chirped pulse, the higher frequencies travel slower than the lower frequencies. This phenomenon has a pronounced effect in the broadening of pulse duration because of the large gain-bandwidth of the Ti:sapphire. A four-prism sequence as shown in Figure 2.5 gives rise to a net negative GVD and is commonly used to correct a positive chirp pulse. The configuration of the prisms provides different path lengths for different frequency waves as the prisms force the high frequencies (blue-side of the pulse) to travel a shorter distance while the low frequencies (red-

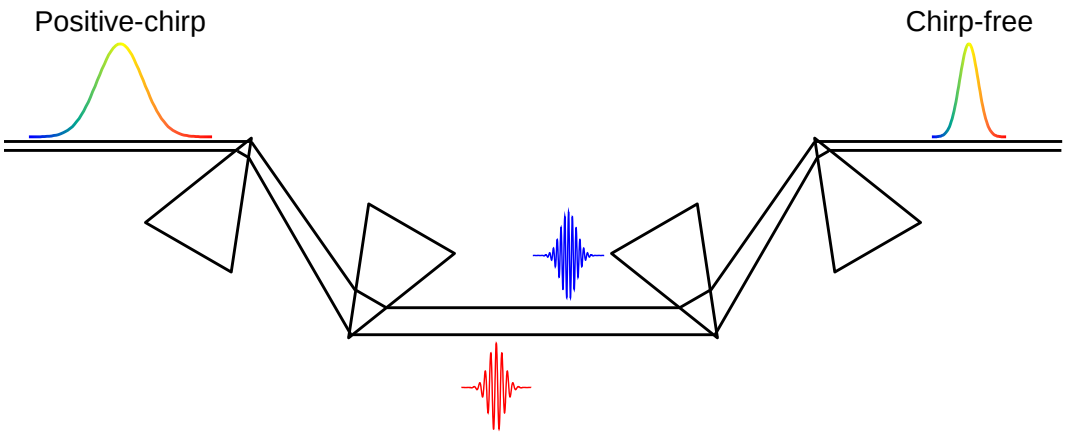

Figure 2.5. Dispersion compensation of a positively-chirped pulse using the four prism sequence, which gives rise to a shorter path length for the higher frequencies than the lower frequencies.

side of the pulse) travel a longer distance. The difference in path lengths for different frequencies compensates for the delay on the blue-side of the pulse by delaying the red-side of the pulse by the same degree. The resulting pulse has all the frequencies arriving at the same time, which also known as a chirp-free pulse. It is important to note that both positive and negative GVD are the key properties for ultrashort pulse amplification.

2.1.3 Chirped Pulse Amplification

Despite the Ti:sapphire having high thermal conductivity, it cannot be optically pumped with high power without the possibility of having thermal distortion effects [12]. Therefore, chirped pulse amplification (CPA) is used to amplify pulses to avoid damage of the Ti:sapphire. Figure 2.6 shows a schematic layout of a chirped pulse

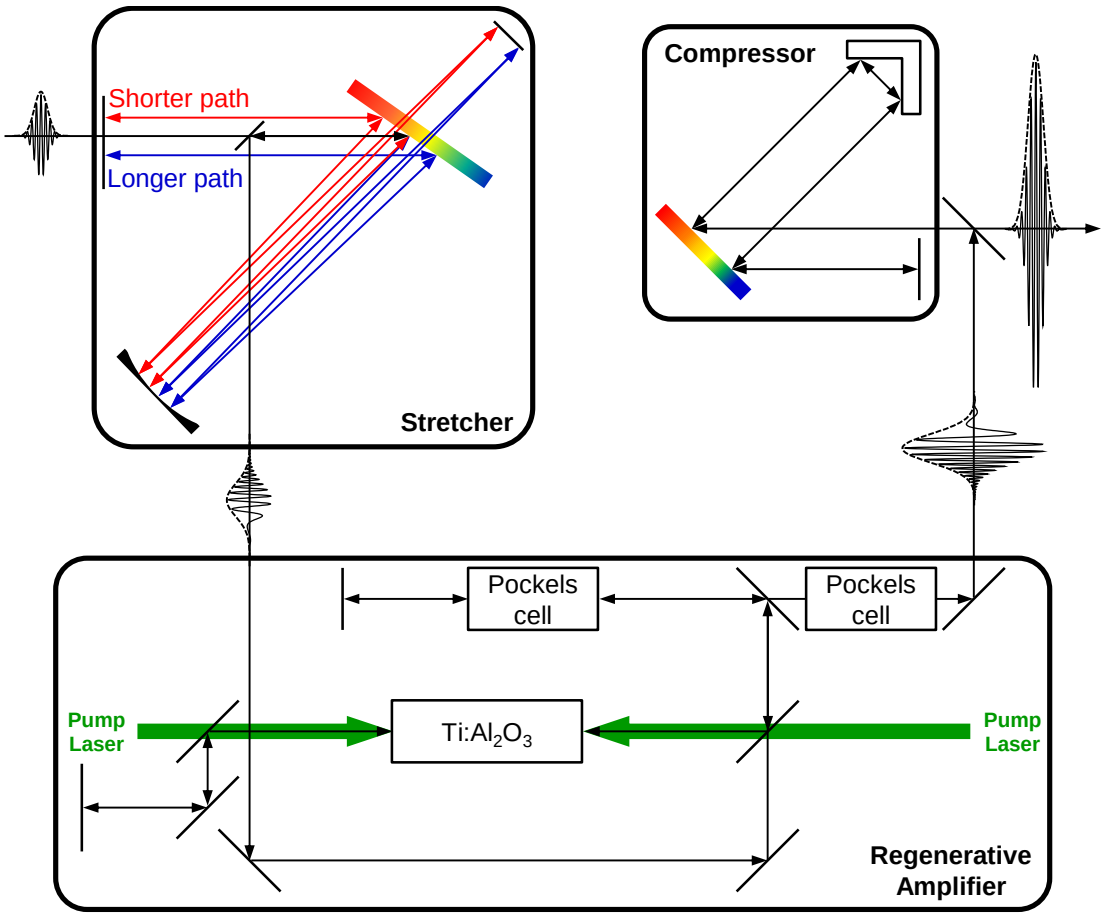

Figure 2.6. Schematic layout of a chirped pulse amplifier, which consists of a stretcher, a regenerative amplifier and a compressor.

amplifier, which consists of a stretcher, a regenerative amplifier and a compressor. The stretcher increases the pulse width by providing a positive GVD, which is achieved by a diffraction grating and a concave mirror. As illustrated in Figure 2.6, the stretcher allows multiple passes of the pulse between the diffraction grating and the concave mirror. The positive GVD of the stretcher causes the higher frequencies to travel a longer path length than the lower frequencies. As a result, the red-side of the pulse exits before the blue-side. After the stretcher, a 'stretched' pulse with a lower peak intensity than the initial pulse is produced and guided into the regenerative amplifier. Typically, a gain medium, such as a Ti:sapphire crystal, is pumped by a high-energy laser (shown as green arrows in Figure 2.6) to achieve population inversion and most of the energy is retained in the crystal. The 'stretched' pulses are then passed through the gain medium and recirculated multiple times until all the energy retained in the Ti:sapphire crystal is extracted, which results in an amplified pulse. The amplified pulse is then introduced to the compressor by synchronised Pockels cells, which select, confine and eject light pulse in the regenerative amplifier. Different from the four prism sequence discussed earlier, the negative GVD of the compressor is achieved with a horizontal retroreflector and a diffraction grating. The negative GVD of the compressor corrects the positively-chirped pulse by forcing the higher frequencies to travel a shorter distance than the lower frequency. The output pulses after CPA has a pulse width that is comparable to the initial pulse but with a much higher peak intensity. It is important to note that the output pulses have the same repetition rate as the pump laser, which is used to achieve a population inversion in the Ti:sapphire crystal.

2.2 Ultrafast Laser Setup

Our ultrafast laser system consists of two main components: a Ti:sapphire mode-locked oscillator (Spectra-Physics, *Tsunami*) and a Ti:sapphire regenerative amplifier (Spectra-Physics, *Spitfire Pro XP*). The output pulses are centred at 800 nm with a 100-fs pulse duration and a repetition rate of 1 kHz. First, the *Tsunami* laser is pumped by a 532-nm Nd:YVO_4 laser (a diode-pumped, continuous wave solid state laser) and generates 100-fs pulses with a repetition rate of 80 MHz. It has a cavity length of $\sim$ 12.2 ns and it is passively mode-locked (see Section 2.1.1). It is important to note that there is

the equivalent of a four-prism sequence for the compensation of dispersion inside the laser cavity, which is detailed in Section 2.1.2. Second, the output of the *Tsunami* laser is amplified by the Ti:sapphire regenerative amplifier using CPA, which is discussed in Section 2.1.3. Briefly, the 100-fs pulses from the *Tsunami* are stretched using a diffraction grating and a concave mirror, which create a positive GVD temporally prior to the regenerative amplification. A population inversion is generated in a Ti:sapphire rod pumped by a 20-W 527-nm Nd:YLF laser with a repetition rate of 1 kHz (Spectra-Physics, *Empower*). The stretched pulses from the *Tsunami* laser pass through the rod multiple times until most of the energy accumulated in the rod is extracted. It is worth noting that the overlap of the pump and the seed pulse in space at the rod is aligned to optimise the power of the amplified output. Then the amplified pulse is recompressed to its initial pulse width using a diffraction grating and a horizontal retroreflector and the compressor is regularly optimised to achieve a stable amplified output. Finally, a fraction of the 800-nm output beam with a 100-fs pulse duration and a repetition rate of 1 kHz is used to pump an optical parametric amplifier.

2.3 Parametric Non-linearities

Parametric non-linearities are optical non-linearities based on the second-order ($\chi^{(2)}$) non-linear susceptibility of a material, with which the energy conversion of photons is satisfied. High light intensity causes deformation of the electron cloud, and gives rise to an induced dipole moment in the non-linear material. This phenomenon is known as dielectric polarisability. It is important to note that this dielectric polarisation propagates in the form of a polarisation wave together with the induced electromagnetic field in the non-linear material. The dielectric polarisation (**P**) of a material with $\chi^{(2)}$ non-linear susceptibility subjected to an electric field is given as

$$\boldsymbol{P} = \varepsilon_0(\chi^{(1)}\boldsymbol{E} + \chi^{(2)}\boldsymbol{E}^2) \tag{2.5}$$

of which the first linear term ($\chi^{(1)}\boldsymbol{E}$) describes the Rayleigh scattering and the second quadratic term ($\chi^{(2)}\boldsymbol{E}^2$) contributes to the second order non-linear effect [4, 13–15].

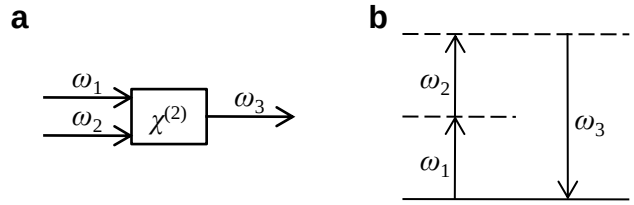

Figure 2.7. (a) A schematic illustration of the $\chi^{(2)}$ non-linear optical effect. (b) Energy-level diagram of the $\chi^{(2)}$ non-linear optical effect. For sum frequency generation, $\omega_3 = \omega_1 + \omega_2$ and for second harmonic generation, $\omega_1 = \omega_2 = \omega$ and $\omega_3 = 2\omega$.

β-Barium borate or β-BaB_2O_4 (BBO) is a common non-linear material and it has birefringence, which is a phenomenon of refractive indices depending on the polarisation of light beam. BBO has two refractive indices for the ordinary (n_o) and extraordinary wave (n_e). The ordinary wave is polarised perpendicular to the optical axis of the material while the extraordinary wave is parallel [14]. On one hand, when n_e is greater than n_o, the material is positively birefringent; on the other hand, when n_e is less than n_o, the material is negatively birefringent. Phase matching (Δk) is a constant phase relationship between the pump, ω_1 and ω_2, and signal waves, ω_3, ($\Delta k = k_{\text{pump}} - k_{\text{signal}} = 0$) when the refractive indices are the same for both waves

($n_{\text{pump}} = n_{\text{signal}}$), which is essential for efficient non-linear energy conversion [4, 13–15]. Furthermore, the types of phase matching in BBO are characterised according to the pump and signal waves propagating as ordinary or extraordinary wave. There are three types of phase matching in BBO: type-I, which is o, $o \rightarrow e$; type-II, which is o, $e \rightarrow e$; and type-III, which is e, $o \rightarrow e$, where 'o' represents ordinary wave and 'e' for extraordinary wave [14, 16]. The major advantage of BBO is its large birefringence that enables a wide phase-matching range for type-I and type-II but type-III is rarely used for its relatively small spectral phase-matching range [16]. Examples of a $\chi^{(2)}$ non-linear optical effect of BBO include sum frequency generation (SFG) and second harmonic generation (SHG), as shown in Figure 2.7. In the case of SFG, the pump waves with frequencies of ω_1 and ω_2 generate a sum frequency signal with $\omega_3 = \omega_1 + \omega_2$. In the case of SHG, the pump frequency $\omega_1 = \omega_2 = \omega$ generate a second harmonic signal with $\omega_3 = 2\omega$ through a material with a $\chi^{(2)}$ non-linearity. From Equation (2.5), the non-linear polarisation for the SFG is

$$\boldsymbol{P}(\omega_1 + \omega_2) = 2\varepsilon_0(\chi^{(2)}\boldsymbol{E}_1\boldsymbol{E}_2) \tag{2.6}$$

and similarly, the non-linear polarisation for the SHG is

$$\boldsymbol{P}(2\omega) = \varepsilon_0(\chi^{(2)}\boldsymbol{E}_1^2) \tag{2.7}$$

where $\boldsymbol{E}_1$ and $\boldsymbol{E}_2$ are the electric fields of the pump [13–15]. Furthermore, the phase-mismatch condition for SFG is $\Delta k = k_1 + k_2 - k_3$ and that for SHG is $\Delta k = 2k_1 - k_3$ where $k_1 = k_2$ [13, 15].

2.3.1 Optical Parametric Amplification

Optical parametric amplification is a phenomenon where a signal is amplified using optical parametric non-linearity and a pump wave. It is different from laser amplification, in which stimulated emission of a gain medium is involved. An optical parametric amplifier does not involve any excitation of a gain medium to higher energy levels but instead it uses the non-linearity of a non-linear crystal [14]. One advantage of optical parametric amplification is the tunable and wide-range of wavelengths avail-

able, which are often difficult to access with lasers due to the lack of a suitable gain medium. Basically, the optical parametric amplifier consists of a white-light generator, a pre-amplifier and a power amplifier. A small fraction (1 – 3 μJ) of the 800-nm pump pulse, which is obtained by CPA with a Ti:sapphire regenerative amplifier described in Section 2.2, is used to generate a white-light continuum with a sapphire plate. The vertically polarised white-light continuum is then non-collinearly overlapped with another fraction (30 – 50 μJ) of the horizontally polarised pump pulse in a BBO crystal where pre-amplification of the signal beam occurs. The signal beam and about 90 – 98 % of the pump pulse are collinearly overlapped in a second BBO crystal where power amplification takes place yielding collinear signal and idler beams. The wavelength tuning is achieved by changing the delay of the white-light pulse with respect to the first pump pulse, the angles of the pre-amplification and the power amplification BBO crystal, and the delay of the signal beam with respect to the second pump pulse. Finally, wavelengths tunability in the near infrared (NIR) to ultraviolet (UV) region are obtained by frequency mixing of the pump, signal and idler beams with type-I BBO crystals. The SHG of the signal or idler and SFG of the 800-nm pump pulse with the signal or idler cover the range 480 – 1200 nm of the visible and NIR spectra. In addition, the SHG of the second harmonic of the signal or idler and SHG of the sum frequency of the pump pulse with the signal or idler results in wavelengths from 240 – 590 nm in the UV and visible spectra.

2.4 Time-resolved Spectroscopy

One of the applications of ultrafast lasers is to study very fast processes in atomic and molecular system that occur on the time scales of pico- to femtosecond [4, 17]. To achieve a high resolution beyond the response limits of electronic devices, a pump-probe technique using a pulsed laser is employed [4, 17]. Figure 2.8 illustrates a schematic time-domain description of time-resolved pump-probe spectroscopy and the corresponding energy levels of a sample as a function of time. As illustrated by the red curve in Figure 2.8, before the arrival of the pump pulse at the sample, there is no signal generated by the probe pulse as there is no population in the first excited state (S_1), as shown in the energy-level diagram at the top of Figure 2.8. The pump pulse is then applied to promote some of the ground state (S_0) population into the S_1 state, which is measured by the probe pulse. For a simple system shown in Figure 2.8, a signal is generated from the probe and it is most intense at time zero (t_0), when the pump and the probe pulses arrive at the sample at the same time. The probe pulse measures the population of the S_1 state as a function of time by delaying its arrival with respect to the pump pulse. As the population in the S_1 state relaxes to the lower S_0 state, the signal arises from the probe decreases as a function of time and eventually decreases to the baseline level. As the temporal resolution is limited by the pulse durations of

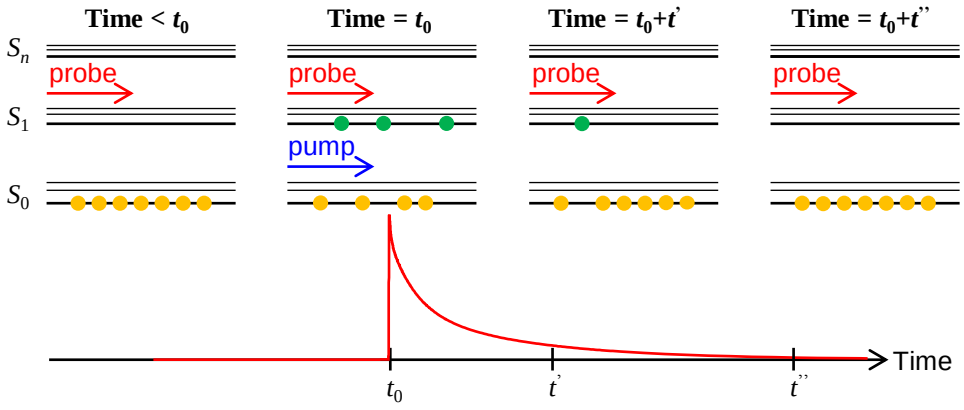

Figure 2.8. Energy-level diagrams of a system interacting with the probe and pump pulses (top) and its excited state decay curve as a function of time (bottom). Both the pump and probe pulses arrive at the sample simultaneously at t_0. The kinetics of the S_1 decay is therefore measured by delaying the arriving time of the probe pulse with respect to the pump pulse.

pump and probe pulses, the ultrashort pulse laser enables measurements with pico- to femtosecond resolution. In the following section, two time-resolved spectroscopic techniques are discussed, namely, transient absorption spectroscopy and fluorescence upconversion spectroscopy.

2.4.1 Transient Absorption Spectroscopy

In transient absorption spectroscopy, the excited state absorbance of a sample is measured as a function of time after excitation by a pump pulse [17]. Figure 2.9 shows the layout of the pump-probe transient absorption spectrometer (Ultrafast Systems, *Helios*). The 800-nm output beam with a 100-fs pulse duration and a repetition rate of 1 kHz of the Ti:sapphire regenerative amplifier (see Section 2.2) is split to generate the pump and probe beams. The pump beam is generated from an optical parametric amplifier (Light Conversion, *TOPAS-C*) as discussed in Section 2.3.1 and the probe beam is derived from white-light generation using a 2-mm sapphire plate. The polarisation

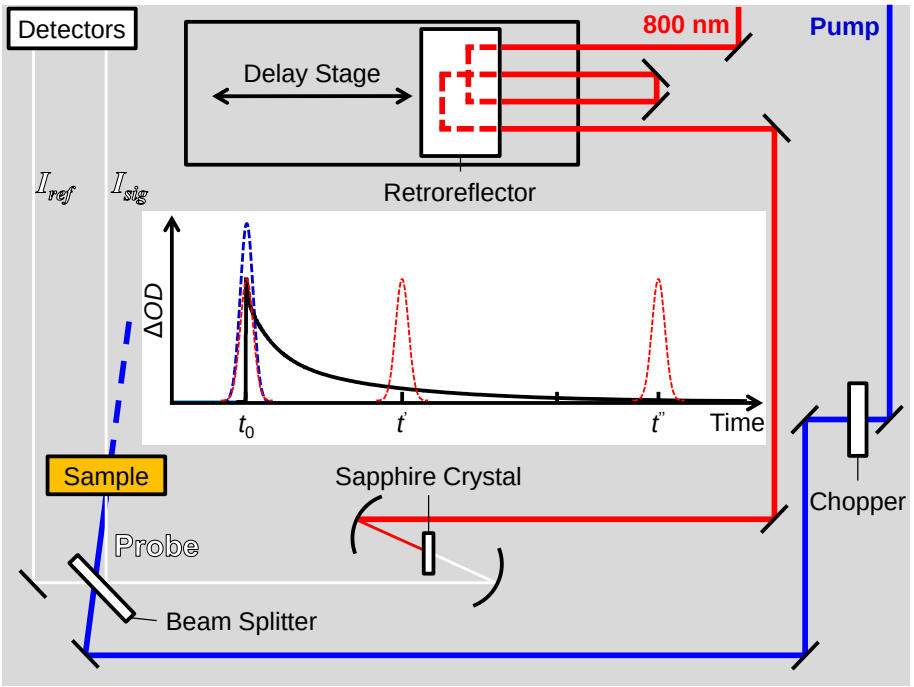

Figure 2.9. Schematic layout of the time-resolved transient absorption spectrometer. The pump is shown as the blue beam. The white-light continuum is the probe. The inset shows the ESA decay curve as a function of time with the arrival of the pump pulse and the delayed probe pulses at the sample represented by the blue and red dashed-curves, respectively.

of the pump beam is set at magic angle (54.7°) with respect to the probe beam and the overlap of the two beams is regularly maintained for an optimised signal. The probe beam is split equally into signal and reference beams. The signal beam gives the optical density signal (OD). The reference beam accounts for laser intensity fluctuations in the OD signal. The pump beam is mechanically modulated at a rate of 500 Hz to produce measurements both with and without it. The transient signal as a function of wavelength and time ($\Delta OD(\lambda,t)$) is then given as

$$\Delta OD(\lambda,t) = OD(\lambda,t)_{\text{pump}} - OD(\lambda)_{\text{no pump}} \tag{2.8}$$

It is important to note that the $OD(\lambda)_{\text{no pump}}$ is equivalent to the ground state absorbance and the $OD(\lambda,t)_{\text{pump}}$ is the time-resolved absorbance of the ground and excited states. For a negative $\Delta OD(\lambda,t)$, the amplitude of $OD(\lambda,t)_{\text{pump}}$ is lower than that of $OD(\lambda)_{\text{no pump}}$ (Equation (2.8)), which is attributable to ground-state bleaching or stimulated emission (SE) of the sample. On one hand, a fraction of population in the S_0 state is promoted to the S_1 state by the pump pulse, causing a decrease in the S_0 state population. As a consequence, the ground state absorption of the sample after the pump pulse is less than that without the pump pulse, leading to a negative $\Delta OD(\lambda,t)$ at wavelengths in the ground state absorption region. On the other hand, if the probe arrives at the excited sample and its frequency is resonant to the energy gap between the S_0 and S_1 states, this will lead to emission of photons as the excited population relaxes back to the S_0 state. As a result of SE, the value of $OD(\lambda,t)_{\text{pump}}$ is smaller than $OD(\lambda)_{\text{no pump}}$, and thus a negative $\Delta OD(\lambda,t)$. It is important to note that the negative $\Delta OD(\lambda,t)$ due to SE appears at wavelengths within the emission spectrum of the sample. According to Equation (2.8), the value of $OD(\lambda,t)_{\text{pump}}$ must be larger than that of $OD(\lambda)_{\text{no pump}}$ to yield a positive $\Delta OD(\lambda,t)$. In the case, the probe light is absorbed by the excited state, which leads to $OD(\lambda,t)_{\text{pump}} > OD(\lambda)_{\text{no pump}}$. As a result, the $\Delta OD(\lambda,t)$ is positive and it is attributable to excited state absorption (ESA). The inset of Figure 2.9 shows the ESA decay curve (black) as a function of time with the dashed-curves indicating the arrival of the pump pulse and the delayed probe pulses at the sample.

2.4.2 Fluorescence Upconversion Spectroscopy

In fluorescence upconversion spectroscopy, a gate pulse is used to upconvert a fluorescence emission signal produced after excitation with a pump pulse [4, 17]. The layout of a fluorescence upconversion spectrometer (Ultrafast Systems, *Halcyone*) is shown in Figure 2.10. The output of the Ti:sapphire regenerative amplifier, centred at 800 nm with a repetition rate of 1 kHz and pulse duration of 100 fs, is split into the excitation and gate beams. The polarisation of the pump is set at magic angle (54.7°) with respect to the gate. Frequency-doubled pulses (400 nm) are used to excite the sample and fluorescence is collected with a plano-convex lens. The gate pulse and fluorescence from the sample are then focussed onto a 0.4 mm type-I BBO crystal to generate sum-frequency signals, which are detected by a photomultiplier tube attached to a monochromator. Similar to the probe pulse in the transient spectroscopy, the gate pulse is delayed with respect to the pump pulse, which enables measurements of the fluorescence decay kinetics, as shown in Figure 2.10. In fluorescence upconversion, the t_0 is defined as the time when the fluorescence signal and the gate pulses arrive at the BBO crystal simultaneously and the optimisation of upconverted signal is done by overlapping of the two beams.

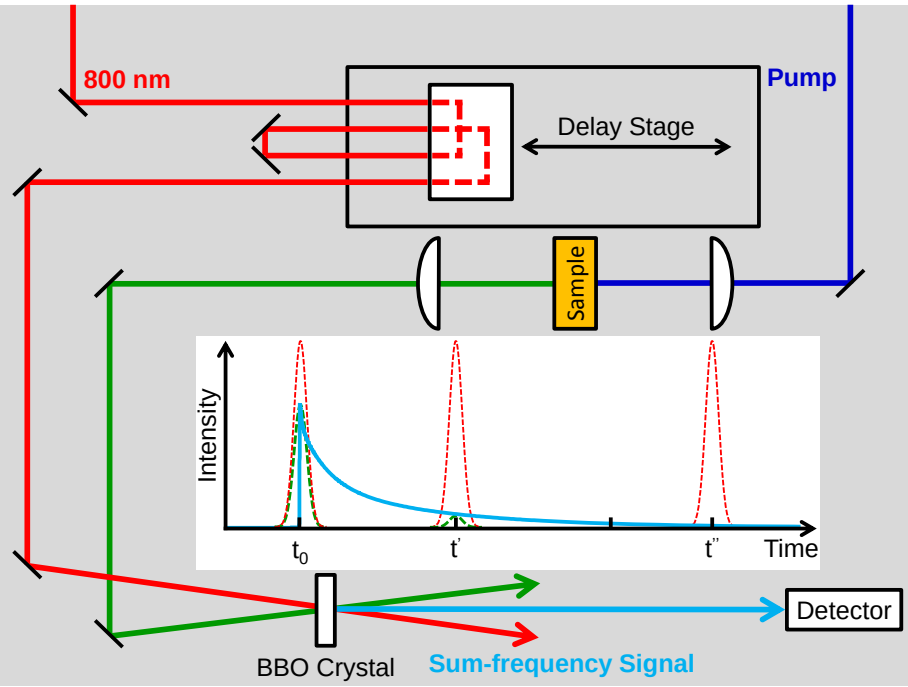

Figure 2.10. Schematic layout of the fluorescence upconversion spectrometer. The pump is used to excite a sample (blue). The red represents the 800-nm gate beam, which overlaps with the fluorescence emission (green) from the sample at the BBO crystal to generate the sum-frequency signal. The inset shows the sum-frequency signal decay curve as a function of time with the dashed-line, indicating the arrival of the fluorescence signal (green dashed-curve) and the gate (red dashed-curve) at the BBO crystal.

2.5 References

(1) Silfvast, W. T., *Laser Fundamentals*, 2nd ed.; Cambridge University Press: 2004.

(2) Svelto, O., *Principles of Laser*, 5th ed.; Hanna, D. C., Ed.; Springer: 2010.

(3) Moulton, P. F. Spectroscopic and Laser Characteristics of Ti:Al_2O_3. *J. Opt. Soc. Am. B* **1986**, *3*, 125–133.

(4) Abramczyk, H., *Introduction to Laser Spectroscopy*; Abramczyk, H., Ed.; Elsevier Science: 2005.

(5) Huggett, G. R. Mode-Locking of CW Lasers by Regenerative RF Feedback. *Appl. Phys. Lett.* **1968**, *13*, 186–187.

(6) Spence, D. E.; Kean, P. N.; Sibbett, W. 60-fsec Pulse Generation from a Self-Mode-Locked Ti:Sapphire Laser. *Opt. Lett.* **1991**, *16*, 42–44.

(7) Keller, U.; 'tHooft, G. W.; Knox, W. H.; Cunningham, J. E. Femtosecond Pulses from a Continuously Self-Starting Passively Mode-Locked Ti:Sapphire Laser. *Opt. Lett.* **1991**, *16*, 1022–1024.

(8) Salin, F.; Squier, J.; Piché, M. Mode Locking of Ti:Al_2O_3 Lasers and Self-Focusing: A Gaussian Approximation. *Opt. Lett.* **1991**, *16*, 1674–1676.

(9) Chiao, R. Y.; Garmire, E.; Townes, C. H. Self-Trapping of Optical Beams. *Phys. Rev. Lett.* **1964**, *13*, 479–482.

(10) Kelley, P. L. Self-Focusing of Optical Beams. *Phys. Rev. Lett.* **1965**, *15*, 1005–1008.

(11) Diels, J.-C.; Rudolph, W. *Ultrashort Laser Pulse Phenomena*, 2nd ed.; Academic Press: 2006.

(12) Backus, S.; Durfee, C. G.; Murnane, M. M.; Kapteyn, H. C. High Power Ultrafast Lasers. *Review of Scientific Instruments* **1998**, *69*, 1207–1223.

(13) Boyd, R. W., *Nonlinear Optics*, 3rd ed.; Academic Press: 2008.

(14) Demtröder, W., *Laser Spectroscopy: Volume 1 Basic Principles*, 4th ed.; Springer: 2008.

(15) Zheltikov, A.; L'Huillier, A.; Krausz, F. *Springer Handbook of Lasers and Optics*, Träger, F., Ed.; Springer Berlin Heidelberg: 2012.

(16) Chen, C.; Sasaki, T.; Li, R., *Nonlinear Optical Borate Crystals: Principles and Applications*, 1st ed.; John Wiley & Sons: 2012.

(17) Singh, S. C.; Dwivedi, Y. *Nanomaterials*, Singh, S. C., Zeng, H., Guo, C., Cai, W., Eds.; Wiley-VCH Verlag GmbH & Co. KGaA: 2012.

CHAPTER 3

FEMTOSECOND TRANSIENT ABSORPTION SPECTROSCOPY OF COPPER(II)–CURCUMIN COMPLEXES

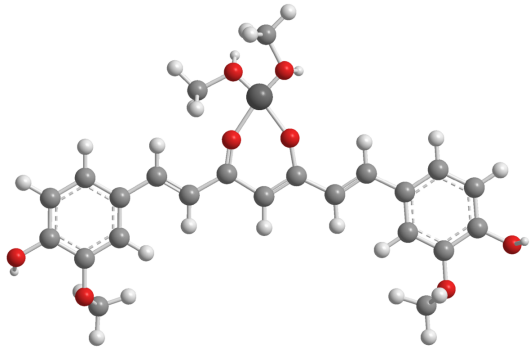

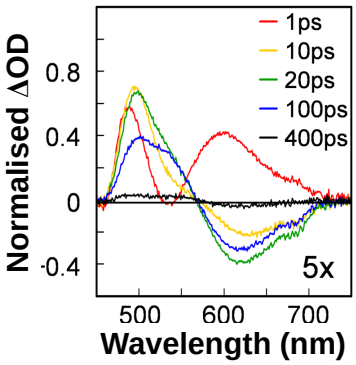

Reproduced by permission from the PCCP Owner Societies.
Leung, M. H. M.; Pham, D.-T.; Lincoln, S. F.; Kee, T. W. Femtosecond Transient Absorption Spectroscopy of Copper(II)–Curcumin Complexes. *Phys. Chem. Chem. Phys.* **2012**, *14*, 13580–13587. http://pubs.rsc.org/en/Content/ArticleLanding/2012/CP/c2cp40208d#!divAbstract

Statement of Authorship

By signing the Statement of Authorship, each author certifies that their stated contribution to the following publication is accurate and that permission is granted for the publication to be included in this thesis.

> Leung, M. H. M.; Pham, D.-T.; Lincoln, S. F.; Kee, T. W., Femtosecond Transient Absorption Spectroscopy of Copper(II)−Curcumin Complexes. *Phys. Chem. Chem. Phys.* **2012**, *14*, 13580–13587.

Author Contributions

Name of First Author (Candidate)	Mandy H. M. Leung
Contribution to the Paper	Data collection and analysis Preparation and editing for manuscript
Signature	
Date	01/09/2014
Name of Co-Author	Dr. Duc-Truc Pham
Contribution to the Paper	Supervision of the candidate Editing of manuscript
Signature	
Date	21/08/2014
Name of Co-Author	Prof. Stephen F. Lincoln
Contribution to the Paper	Supervision of the candidate Editing of manuscript
Signature	
Date	01/09/2014
Name of Co-Author	Dr. Tak W. Kee
Contribution to the Paper	Supervision of the candidate Preparation and editing of manuscript Corresponding author
Signature	
Date	01/09/2014

3.1 Abstract

Ligand-metal interaction between curcumin and Cu(II) in methanol and sodium dodecyl sulphate (SDS) micelles was investigated using fluorescence spectroscopy and transient absorption spectroscopy. The Cu(II) ion exhibits a high efficiency in quenching the fluorescence of curcumin. By quantifying fluorescence quenching as a function of Cu(II) concentration, the complexation constants, K_1 and K_2, for the formation of the 1:1 and 1:2 Cu(II)−Curcumin complexes, $[Cu^{II}{-}Cur]^+$ and $[Cu^{II}{-}Cur_2]$, have been determined. In methanol, K_1 and K_2 are $(1.33 \pm 0.47) \times 10^8\ M^{-1}$ and $(6.79 \pm 1.77) \times 10^5\ M^{-1}$, respectively, whereas those in SDS micelles are $(9.90 \pm 1.68) \times 10^5\ M^{-1}$ and $(1.70 \pm 0.48) \times 10^6\ M^{-1}$, respectively. The transient absorption spectra of curcumin and the Cu(II)−Curcumin complexes from 520 – 700 nm show a combination of stimulated emission and excited state absorption (ESA). However, the transient absorption signal at 500 nm corresponds to ESA exclusively. For curcumin, the ESA kinetics exhibit two rising components with time constants of 0.9 ps and 8.2 ps in methanol, and 0.5 ps and 2.5 ps in SDS micelles, which are consistent with solvation dynamics of excited state curcumin in these media. In addition, the ESA kinetics show a decay component with a time constant of 125 ps in methanol and 64 ps in SDS micelles, reflecting the excited state intramolecular hydrogen atom transfer of curcumin in these media. The ESA kinetics of the Cu(II)−Curcumin complexes exhibit a sharp rise and a fast decay with a time constant of approximately 1 ps in both media due to the strong interaction between Cu(II) and curcumin.

3.2 Introduction

Curcumin (Figure 3.1) forms the majority of the naturally occurring yellow pigments in the Indian spice turmeric [1]. It has been shown that curcumin exhibits anti-cancer [2], anti-Alzheimer's [3], anti-cystic fibrosis [4], and other medicinal effects [5–7], and consequently there is an intense research focus on curcumin due to its apparent targeted medicinal effects. In particular, curcumin is a potent inhibitor to cancer cells while exhibiting negligible side effects to normal cells [2, 8]. Recently, it was shown that the cytotoxicity of curcumin to cancer cells can be enhanced by photo-excitation, indicating its potential as an effective photodynamic therapy agent [9–11]. More recently, studies have shown that the interaction of curcumin with Cu(II) ions may be important for its anti-amyloid and anti-cancer properties for the follow-

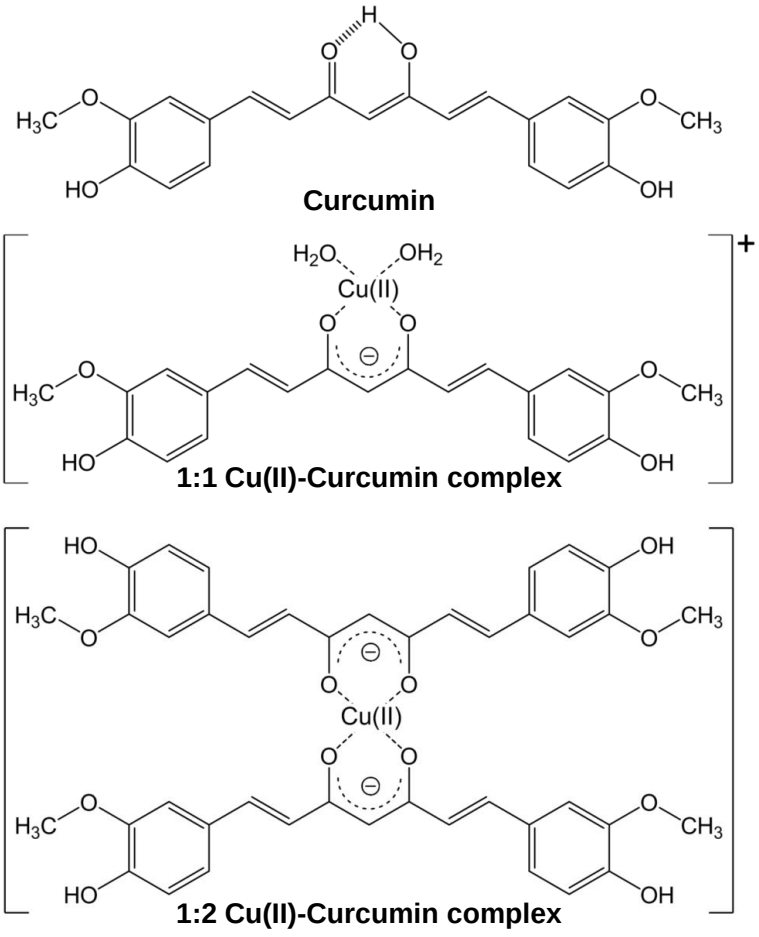

Figure 3.1. Structure of curcumin, the 1:1 and 1:2 Cu(II)−Curcumin complexes, $[Cu^{II}-Cur]^{+}$ and $[Cu^{II}-Cur_2]$.

ing two reasons [12–15]. First, an elevated level of Cu(II) is found in amyloid fibrils and in tumours [16–18]. Second, deprotonation of the hydroxyl group in the keto-enol moiety of curcumin (Figure 3.1) leads to formation of a bidentate β-diketonate which strongly chelates with Cu(II) [19, 20]. A recent study revealed that curcumin forms stable complexes with Cu(II) in two different square planar geometries, the 1:1 and 1:2 Cu(II)−Curcumin complexes [21], as shown in Figure 3.1.

Femtosecond transient absorption spectroscopy and time-resolved fluorescence up-conversion spectroscopy have been used to reveal important processes of curcumin in the excited state including solvation, intramolecular hydrogen atom transfer and intermolecular hydrogen bonding dynamics [22–25]. Here, we report the excited state kinetics of the Cu(II)−Curcumin complexes for the first time. Our investigation provides insight into the fundamental events that are involved in the photodynamic therapy effects of curcumin [9–11]. Femtosecond transient absorption spectroscopy is used to investigate curcumin and the Cu(II)−Curcumin complexes in this study. Excited state kinetics of the Cu(II)−Curcumin complexes are investigated in methanol and sodium dodecyl sulphate (SDS) micelles. In particular, the SDS micelles serve as a biological membrane model system, which provides biologically relevant information on the Cu(II)−Curcumin complexes. In addition, SDS micelles provide one of the simplest model membrane systems with a well defined and narrow size distribution. Steady state fluorescence spectroscopy is used to study the Cu(II)−Curcumin interaction due to the ability of Cu(II) to quench the fluorescence of curcumin effectively.

The fluorescence quenching results indicate that $[Cu^{II}-Cur]^+$ formation is dominant in methanol while both $[Cu^{II}-Cur]^+$ and $[Cu^{II}-Cur_2]$ complexes are present in SDS micelles. Femtosecond transient absorption studies reveal the presence of a fast decay with a time constant of approximately 1 ps in the excited state absorption of the Cu(II)−Curcumin complexes due to the strong Cu(II)−Curcumin interaction.

3.3 Materials and Methods

3.3.1 Materials

Curcumin (LKT Laboratories, purity $> 98\,\%$), copper(II) sulphate pentahydrate (Chem-Supply, Analytical Reagent Grade), sodium dodecyl sulphate (SDS , Fluka, purity $> 99\,\%$), sodium dihydrogen phosphate monohydrate (Merck, purity $> 99\,\%$), di-sodium hydrogen phosphate dihydrate (Merck, purity $> 99.5\,\%$) and methanol (Merck, Analytical Reagent Grade) were purchased and used without any further purification. All aqueous solutions were prepared using deionised water from a Millipore Milli-Q NANO pure water system.

3.3.2 Sample Preparation

A pH 7.4 phosphate buffer stock solution (PBS, 50 mM phosphate) was prepared by dissolving sodium dihydrogen phosphate monohydrate and di-sodium hydrogen phosphate dihydrate in deionised water. A micellar solution of 16.2 mM SDS in pH 7.4 PBS was prepared. The SDS concentration was twice the critical micelle concentration to ensure formation of micelles. A solution of 1.5 mM curcumin in methanol was used as stock. A 2-µL of curcumin stock was added to 3 mL of either the SDS micellar solution or methanol to achieve a final concentration of 1 µM for curcumin.

3.3.3 UV-visible Absorption and Fluorescence Emission Spectroscopy

UV-visible absorption and fluorescence emission spectra of 1 µM curcumin with and without 2 µM Cu(II) in methanol and SDS micelles were recorded. To achieve a 2 µM of Cu(II) solution, a volume of 40-µL 150 µM $CuSO_4$ stock in methanol or water was added to 3 mL of 1 µM curcumin in methanol or SDS micelles, respectively. For the UV-visible absorption spectroscopy, spectra were recorded from 350 – 700 nm using a Cary IE UV-visible spectrophotometer (Varian). The fluorescence emission spectra were recorded from 430 – 800 nm using a Perkin Elmer LS55 Fluorometer. The excitation wavelength used was 420 nm with both excitation and emission slit

widths set at 5 nm. The reported spectra were averaged over 10 scans at a scan rate of 100 nm/min. The fluorescence spectra were corrected for the wavelength dependence of the lamp spectral intensity and detector response.

3.3.4 Determination of Binding Constants from Titration Experiment

To determine the binding constants of Cu(II)−Curcumin complexes, a series of 2-µL aliquots of the 150 µM $CuSO_4$ stock in methanol or SDS micelles were added to 3 mL of 1 µM curcumin in methanol or SDS micelles, respectively, in a stepwise fashion to achieve a series of Cu(II) concentrations ranging from 0.1 – 2 µM. The overall %v/v of water resulting from the addition of Cu(II) in the sample rose to approximately 2 %. The concentrations of curcumin and Cu(II) were 10 times higher in the titration experiments using UV-visible absorption spectroscopy.

For a model that includes 1:1 and 1:2 complexation, the binding processes are described as follows.

$$\mathrm{Cu^{II}} + \mathrm{Cur{-}H} \overset{K_1}{\rightleftharpoons} [\mathrm{Cu^{II}{-}Cur}]^+ \tag{3.1}$$

$$[\mathrm{Cu^{II}{-}Cur}]^+ + \mathrm{Cur{-}H} \overset{K_2}{\rightleftharpoons} [\mathrm{Cu^{II}{-}Cur_2}] \tag{3.2}$$

where the complexation constants K_1 and K_2 are given as

$$K_1 = \frac{[[\mathrm{Cu^{II}{-}Cur}]^+]}{[\mathrm{Cu^{II}}][\mathrm{Cur{-}H}]} \tag{3.3}$$

$$K_2 = \frac{[[\mathrm{Cu^{II}{-}Cur_2}]]}{[[\mathrm{Cu^{II}{-}Cur}]^+][\mathrm{Cur{-}H}]} \tag{3.4}$$

where $[[\mathrm{Cu^{II}{-}Cur}]^+]$ and $[[\mathrm{Cu^{II}{-}Cur_2}]]$ are concentrations of the 1:1 and 1:2 complexes, respectively, $[\mathrm{Cu^{II}}]$ and $[\mathrm{Cur{-}H}]$ are the concentrations of free Cu(II) ion and free curcumin, respectively, and the proton displaced from Cur−H on complexation is not shown as the solution pH is buffered.

The initial concentrations of Cu(II), $[Cu^{II}]_0$, and curcumin, $[Cur{-}H]_0$, are:

$$[Cu^{II}]_0 = [Cu^{II}] + [[Cu^{II}{-}Cur]^+] + [[Cu^{II}{-}Cur_2]] \tag{3.5}$$

$$[Cur{-}H]_0 = [Cur{-}H] + [[Cu^{II}{-}Cur]^+] + 2[[Cu^{II}{-}Cur_2]] \tag{3.6}$$

The measured spectroscopic signal (either UV-visible absorption or fluorescence) at a particular wavelength for each sample is

$$S(\lambda) = \phi_{Cur-H}(\lambda)[Cur{-}H] + \phi_{[Cu^{II}-Cur]^+}(\lambda)[[Cu^{II}{-}Cur]^+] + \phi_{[Cu^{II}-Cur_2]}(\lambda)[[Cu^{II}{-}Cur_2]] \tag{3.7}$$

where ϕ_{Cur-H}, $\phi_{[Cu^{II}-Cur]^+}$ and $\phi_{[Cu^{II}-Cur_2]}$ represent either the molar extinction coefficient or the molar fluorescence intensities of $Cur{-}H$, $[Cu^{II}{-}Cur]^+$ and $[Cu^{II}{-}Cur_2]$, respectively.

The values of K_1, K_2, $\phi_{Cur-H}(\lambda)$, $\phi_{[Cu^{II}-Cur]^+}(\lambda)$ and $\phi_{[Cu^{II}-Cur_2]}(\lambda)$ were obtained by solving Equations (3.3) to (3.7) and were best fitted to the spectroscopic data simultaneously using a nonlinear least-squares method (HypSpec) [26]. Analyses using a 1:1 complexation model were also performed by excluding the equilibrium as shown in Equation (3.2).

3.3.5 Femtosecond Transient Absorption Spectroscopy

Solutions of 100 µM curcumin in methanol or SDS micelles were used for the transient absorption studies. In addition, solutions with $[Cu(II)]_0$:$[Cur{-}H]_0$ ratio of 0:1, 1:4, 1:2, 1:1 and 2:1 were also used. All measurements were made on freshly prepared samples at room temperature using a quartz cuvette with a 2-mm path length. A maximum of 10 % curcumin photo-degradation was observed in the experiment.

The laser system used for the transient absorption experiments consisted of a mode locked oscillator (Spectra Physics, Tsunami) pumped by a 10-W Nd:YVO_4 laser (Spectra Physics, Millennia Pro) and a Ti:sapphire regenerative amplifier (Spectra Physics, Spitfire Pro XP) pumped by a 20-W Q-switched Nd:YLF laser (Spectra Physics, Em-

power). The Ti:sapphire regenerative amplifier generated 100 fs pulses, centred at 800 nm, at a 1 kHz repetition rate. The output was then split into two beams. The first beam (≈ 1 W) was used to pump an optical parametric amplifier (Light Conversion, TOPAS-C) and generate the 420 nm pump pulse using the fourth harmonic of the idler (1680 nm). The second beam (< 1 mW) was used to generate a white light continuum, which was used as the probe, in a 2-mm sapphire crystal. The diameter of the pump and probe beams were 750 µm and 250 µm, respectively, at the sample. All measurements were performed using a pump energy of 1 µJ and the polarisation of the pump was set at magic angle (54.7°) with respect to the probe. An instrument response function of 100 fs (fwhm) was used based on the goodness of fit.

3.4 Results and Discussion

3.4.1 UV-visible Absorption and Fluorescence Spectroscopy of the Copper(II)−Curcumin Complexes

Curcumin exhibits a high molar absorptivity in methanol with an absorption maximum at 425 nm ($\pi - \pi^*$ transition) as shown in Figure 3.2a (red). The spectrum of curcumin (1 µM) in methanol in the presence of Cu(II) (2 µM) has an extra peak at 450 nm due to interaction between Cu(II) and curcumin, as indicated by the arrow in Figure 3.2a. The absorption spectrum of curcumin in SDS micelles has a peak value at 430 nm and a shoulder peak around 450 nm. The fluorescence spectra of curcumin and curcumin in the presence of Cu(II) are also shown in Figure 3.2. The fluorescence intensity of curcumin in the presence of Cu(II) in methanol is approximately 135 times weaker than that of curcumin.

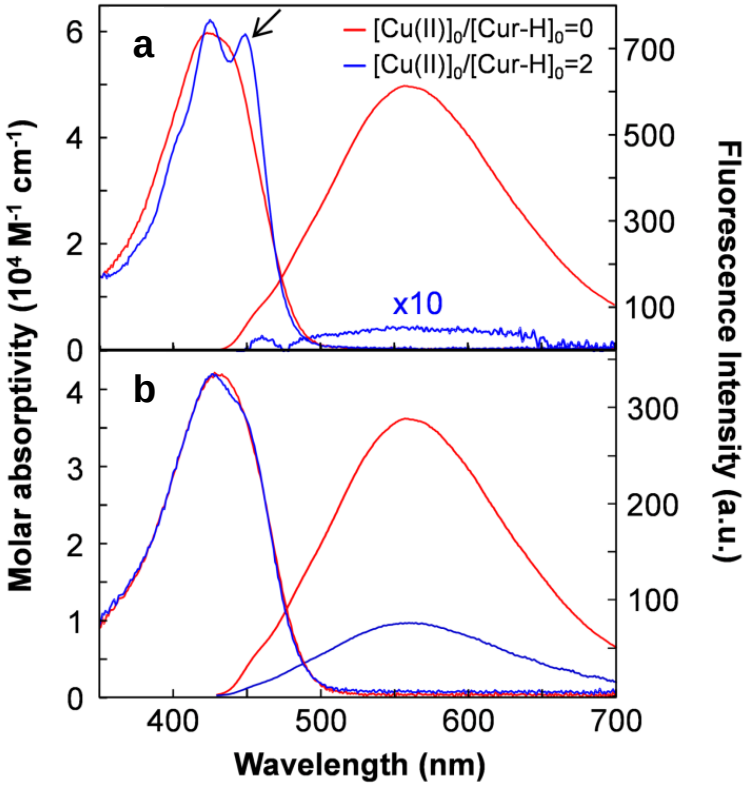

Figure 3.2. Absorption and fluorescence spectra of curcumin (red) and the Cu(II)−Curcumin complexes (blue) in (a) methanol and (b) SDS micelles.

The absorption and fluorescence spectra of curcumin show a Stokes shift of 130 nm in methanol and SDS micelles, as shown in Figure 3.2, and it is attributed to an increase in the dipole moment in the excited state relative to the ground state. It has been demonstrated that curcumin has a larger dipole moment in the excited state than the ground state in both polar media [27]. For SDS micelles, the polarity is related to the high water content [28], which enables curcumin to form hydrogen bonds with the bulk-like water molecules within to produce a large Stokes shift. The fluorescence quantum yields of curcumin in these two media are approximately 3 % and 0.7 %, respectively [29, 30]. However, the Cu(II)-bound curcumin is essentially non-fluorescent in methanol and only weakly fluorescent in SDS micelles. It is known that Cu(II) induces non-radiative deactivation of the excited fluorophore, causing a significant decrease in the fluorescence quantum yield of the fluorophore [31, 32]. It is important to note that the weak fluorescence observed for high $[\mathrm{Cu(II)}]_0/[\mathrm{Cur-H}]_0$ values shown as blue curves in Figure 3.2 are due to the presence of relatively low concentrations of free (*i.e.* uncomplexed) curcumin.

3.4.2 Complexation Constants of the Copper(II)−Curcumin Complexes

The UV-visible absorption spectral features and fluorescence quenching of curcumin by Cu(II) indicate that there is strong complexation between these two species, as described in Equations (3.1) and (3.2), from which the complexation constants may be calculated through Equations (3.3) and (3.4). The curcumin fluorescence intensity decreases monotonically with increasing concentrations of Cu(II), as shown in Figure 3.3, consistent with the formation of Cu(II)−Curcumin complexes. In the insets to Figure 3.3, similarly monotonic decreases in fluorescence seen at single wavelengths together with curves representing the best-fits to an algorithm derived for a complexation model that includes $[\mathrm{Cu^{II}-Cur}]^+$ and $[\mathrm{Cu^{II}-Cur_2}]$ as described by Equations (3.3) to (3.7). Unsatisfactory fits were obtained using a $[\mathrm{Cu^{II}-Cur}]^+$ complexation model alone as discussed and the fits are shown in Figure 3.4. The derived K_1 and K_2 for the Cu(II)−Curcumin complexation in methanol are $(1.33 \pm 0.47) \times 10^8\,\mathrm{M}^{-1}$ and $(6.79 \pm 1.77) \times 10^8\,\mathrm{M}^{-1}$, respectively. It is common for a stepwise metal com-

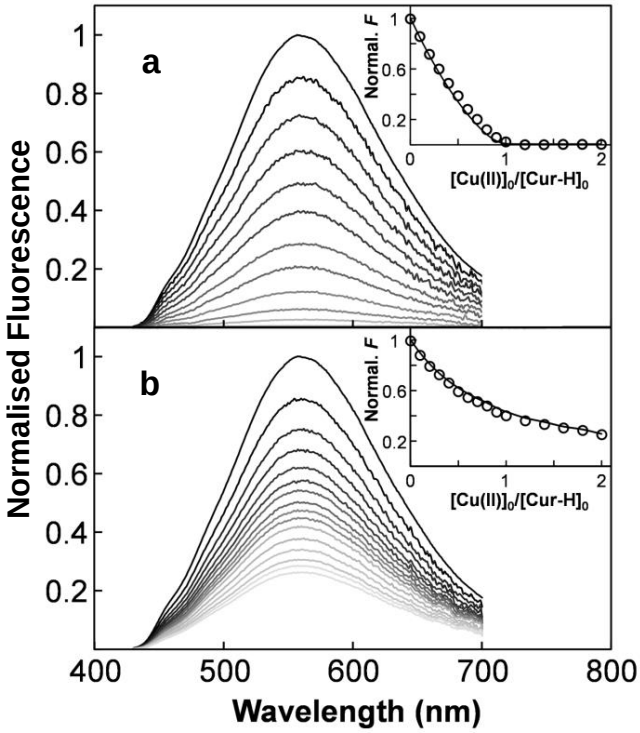

Figure 3.3. Fluorescence quenching of curcumin as a result of addition of Cu(II) in (a) methanol and (b) SDS micelles. The insets show the normalised fluorescence intensity, F, at 540 nm and 530 nm for curcumin in methanol and SDS micelles, respectively. Normalised F is defined as F/F_{max}, where F_{max} is the maximum fluorescence intensity and F is the fluorescence intensity at a specific $[\text{Cu(II)}]_0/[\text{Cur–H}]_0$ value where $[\text{Cur–H}]_0$ is 1 µM. The solid curves represent the best fits for an algorithm derived from Equations (3.3) to (3.7) over the range 500 – 570 nm at 0.5 nm intervals.

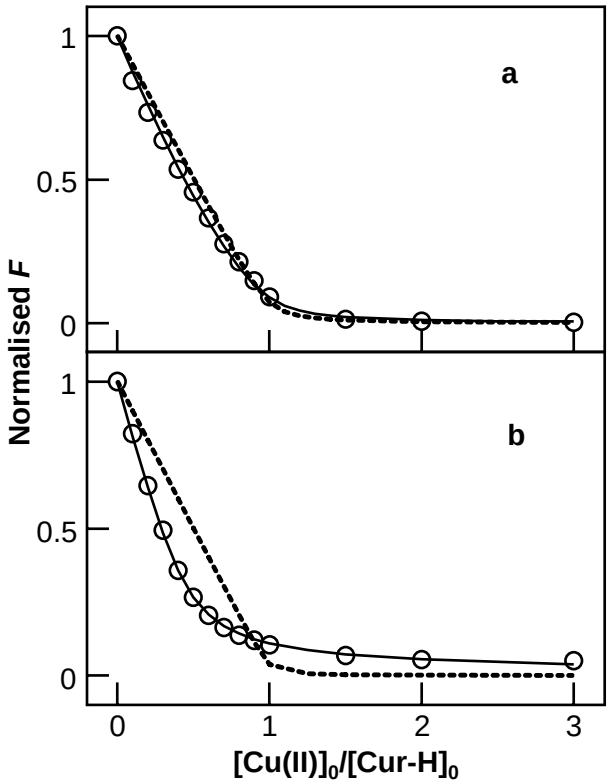

Figure 3.4. Normalised fluorescence intensity at 540 and 530 nm for Cu(II)−Curcumin complexes with $[Cu(II)]_0/[Cur–H]_0$ = 0 – 2 in (a) methanol and (b) SDS micelles, respectively. Normalised F is defined as F/F_{max}, where F_{max} is the maximum fluorescence intensity and F is the fluorescence intensity at a specific $[Cu(II)]_0/[Cur–H]_0$ value where $[Cur–H]_0$ is 10 µM. The solid curves represent the best fits for an algorithm derived from Equations (3.3) to (3.7) over the range 500 – 570 nm at 0.5 nm intervals using a 1:1 and 1:2 Cu(II)−Curcumin complexation model while the dashed curves represent the best fits using strictly a 1:1 Cu(II)−Curcumin complexation model.

plexation process to show a complexation constant trend of $K_1 > K_2$ largely due to statistical effects in the displacement of the initially coordinated ligands (methanol in this case) by a second type of ligand (curcumin in this case) in a stepwise manner when the metal coordination number is constant. It is anticipated that K_1 and K_2 for the Cu(II)−Curcumin complexation will follow the same trend in the aqueous solution. However, the complexation of curcumin with Cu(II) in the SDS micellar solution, which is largely aqueous, is characterised by K_1 and K_2 values of $(9.90 \pm 1.68) \times 10^5\,\mathrm{M}^{-1}$ and $(1.70 \pm 0.48) \times 10^6\,\mathrm{M}^{-1}$, respectively, consistent with the $[\mathrm{Cu^{II}}-\mathrm{Cur_2}]$ being more stable than $[\mathrm{Cu^{II}}-\mathrm{Cur}]^+$ in SDS micelles, in contrast to the situation in methanol.

The cooperativity in complexation of $[\mathrm{Cu^{II}}-\mathrm{Cur}]^+$ and $[\mathrm{Cu^{II}}-\mathrm{Cur_2}]$ is determined using the Hill equation, as shown in Equation (3.8) [33, 34].

$$\log\left(\frac{\mathrm{F_0}-\mathrm{F}}{\mathrm{F}}\right) = \log K_a + h \log[\mathrm{Cu(II)}] \tag{3.8}$$

where $\mathrm{F_0}$ and $\mathrm{F_0}$ are the fluorescence intensities of curcumin with and without addition of Cu(II), respectively, [Cu(II)] denotes the concentration of Cu(II) added, K_a is the binding constant and h is the Hill coefficient which indicates the cooperativity of binding between curcumin and Cu(II). The K_a and h of the binding between curcumin and Cu(II) in methanol and the SDS micellar solution are determined from the slope and y-intercept of the linear fit, respectively, as shown in Figure 3.5. The K_a and h of curcumin at a high and low concentration of Cu(II) are summarised in Table 3.1. The h of the binding between curcumin and Cu(II) in methanol and the SDS

Table 3.1. Binding Constants and Hill Coefficients of Complexation between Curcumin and Cu(II) in Methanol and the SDS Micellar Solution from the Linear Fit of the Hill Equation.[a]

Solvent	h_1	h_2	K_1 (M^{-1})	K_2 (M^{-1})
Methanol	2.58 ± 0.22	1.16 ± 0.05	$(1.60 \pm 0.12) \times 10^{14}$	$(2.42 \pm 0.13) \times 10^6$
SDS	1.02 ± 0.04	1.56 ± 0.04	$(1.16 \pm 0.04) \times 10^6$	$(5.09 \pm 0.13) \times 10^8$

[a] The subscript 1 and 2 denote high and low concentrations of Cu(II), respectively.

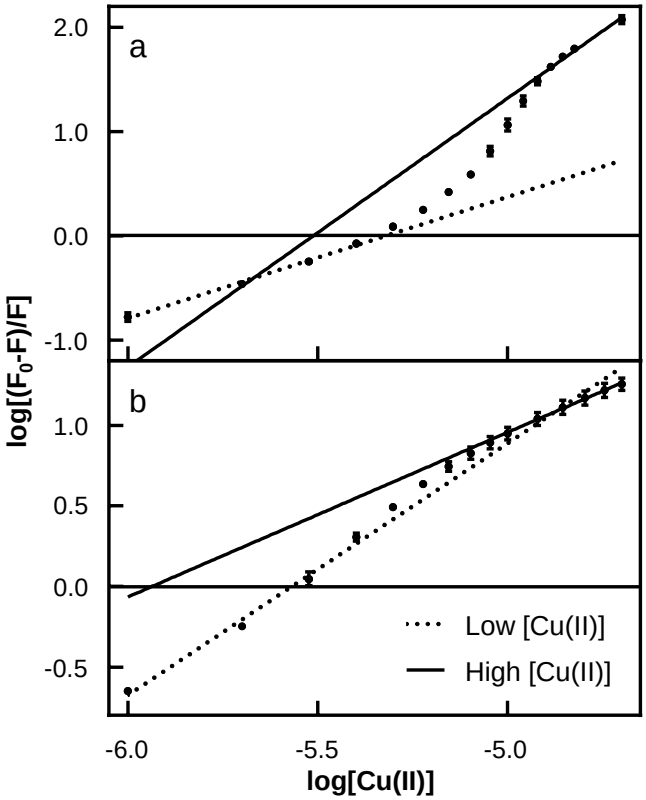

Figure 3.5. Hill plot of fluorescence quenching of curcumin as a result of addition of Cu(II) in (a) methanol and (b) SDS micelles. The solid and dotted line represent the fits with Hill equation at a high and low Cu(II) concentration, respectively.

micellar solution are greater than one, except for a high concentration of Cu(II) in SDS micelle which is equal to one. These results indicate that the binding between curcumin and Cu(II) is positively cooperative in methanol and the SDS micellar solution, however, at high concentration of Cu(II) the binding becomes non-cooperative in SDS micelles. The cooperative binding between curcumin and Cu(II) is attributed to a change from six-coordination in $[Cu^{II}{-}Cur]^{+}$ to four-coordination in $[Cu^{II}{-}Cur_2]$ at a low $[Cu(II)]_0/[Cur{-}H]_0$ ratio. Furthermore, the extrapolation of the linear fit at a high and low concentration of Cu(II) gives the binding constants, K_1 and K_2, which exhibit the same trend observed in fluorescence quenching ($K_1 > K_2$ in methanol and $K_1 < K_2$ in SDS micelle).

The changes in the UV-visible absorption spectrum of curcumin in presence of Cu(II) also suggest the formation of the Cu(II)−Curcumin complexes (Figure 3.2 and Figure 3.6). This spectral response is also best-fitted to a complexation model that includes both $[Cu^{II}{-}Cur]^{+}$ and $[Cu^{II}{-}Cur_2]$ (Figure 3.6). Analyses of these data in-

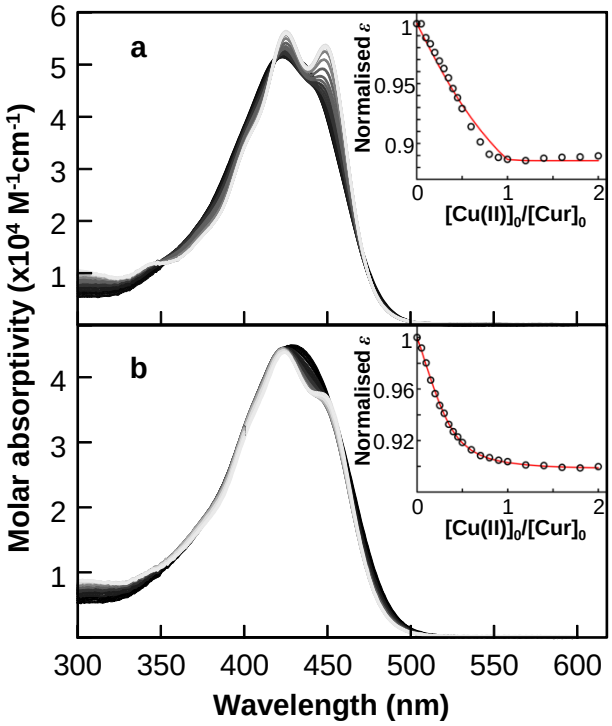

Figure 3.6. UV-visible absorption spectra of curcumin in (a) methanol with addition of Cu(II) with inset showing the change in absorptivity at 410 nm; and (b) SDS micelles with addition of Cu(II) with inset showing the change of absorptivity at 434 nm. The fitting with a 1:1 and 1:2 Cu(II)−Curcumin complexation model is shown as red curve.

dicate that K_1 and K_2 for the Cu(II)−Curcumin complexation in methanol are $(9.38 \pm 1.20) \times 10^8$ M^{-1} and $(1.15 \pm 1.05) \times 10^5$ M^{-1}, respectively. For the Cu(II)−Curcumin complexation in SDS micelles, K_1 and K_2 are $(2.16 \pm 0.44) \times 10^5$ M^{-1} and $(1.83 \pm 1.36) \times 10^6$ M^{-1}. The errors in these values are noticeably higher than those obtained from the fluorescence quenching data as a consequence of changes in the UV-visible absorption data owing to the Cu(II)−Curcumin complexation being much less than for the fluorescence quenching data. Overall, the K_1 and K_2 calculated from the UV-visible data are in reasonable agreement with those determined using fluorescence quenching.

It is noteworthy that the K_1 and K_2 values in SDS micelles are comparable to the average complexation constants of Cu(II) to ceruloplasmin, the major Cu(II) carrying protein in the blood. Ceruloplasmin has the ability to bind up to ten Cu(II) ions with an averaged complexation constant of 2×10^5 M^{-1} [35]. The substantial values of K_1 and K_2 indicate that curcumin is likely to form a complex with Cu(II) in the blood competitively in the presence of ceruloplasmin, which has been suggested to in part

give rise to the anti-cancer effects of curcumin [12, 13, 15].

3.4.3 Speciation of the Copper(II)−Curcumin Complexes

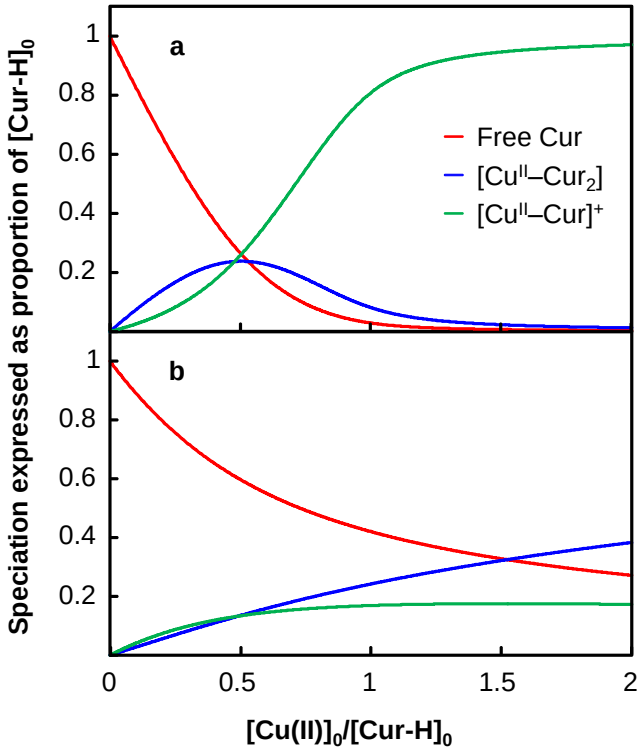

Figure 3.7. Speciation plot of free curcumin and Cu(II)−Curcumin complexes with $[Cu(II)]_0/[Cur–H]_0 = 0 – 2$ in (a) methanol and (b) the SDS micellar solution. Speciation is expressed as proportion of $[Cur–H]_0$. The proportion of the $[Cu^{II}–Cur_2]$ must be multiplied by 2 to obtain the proportion of Cur therein.

The K_1 and K_2 values derived from the fluorescence quenching data yield the speciation variation of the Cu(II)−Curcumin complexes in methanol and SDS micelles for 1 µM $[Cur–H]_0$ as $[Cu(II)]_0$ is varied from 0.1 – 2 µM as described in Equations (3.5) and (3.6), as shown in Figure 3.7. The $[Cu^{II}–Cur]^+$ complex is the dominant species in methanol and only a low concentration of $[Cu^{II}–Cur_2]$ is present as anticipated for $K_1 > K_2$. However, a different speciation occurs in SDS micelles wherein the concentration of $[Cu^{II}–Cur_2]$ is significantly higher than that in methanol as a consequence of $K_1 < K_2$.

The more favourable formation of the $[Cu^{II}–Cur_2]$ complex in SDS micelles most probably arises from its Cu(II) coordination number being decreased to four. Initially,

fully hydrated Cu(II) is complexed by six water ligands in the bulk water in the SDS micellar solution. Subsequently, the interaction between curcumin, which is located in the palisade layer of the SDS micelle [22, 24, 27], and Cu(II) results in the formation of $[Cu^{II}-Cur]^{+}$. This singly positively charged complex is likely to form at the micelle-water interface such that Cu(II) retains a coordination number of six and also interacts electrostatically with the head-groups of SDS. The binding of a second curcumin results in the formation of the neutral $[Cu^{II}-Cur_2]$, which is consequently more hydrophobic and likely to be contained partially in the hydrophobic dodecyl region of the SDS micelle. Therein, the water content is substantially less than in bulk water. The generally hydrophobic environment and a relatively low water content may cooperatively stabilise $[Cu^{II}-Cur_2]$ by comparison with $[Cu^{II}-Cur]^{+}$, and decrease its coordination number to four with the consequence that $K_1 < K_2$. This explanation is supported by the results of an earlier computational study, which show that in the absence of bulk water the complexing energy of the square planar $[Cu^{II}-Cur_2]$ is higher than that of the square planar $[Cu^{II}-Cur]^{+}$ in which two water ligands are bound [21].

3.4.4 Transient Absorption Spectra of Curcumin in Methanol and SDS micelles

The transient absorption spectra of curcumin from 450 – 750 nm in methanol and SDS micelles with probe delay times ranging from 1 – 400 ps are shown in Figure 3.8a and Figure 3.8b, respectively. Curcumin in methanol at 1 ps exhibits two excited state absorption (ESA) peaks around 500 nm and 600 nm, respectively, and a stimulated emission (SE) signal around 540 nm. In comparison, curcumin in SDS micelles (Figure 3.8b) at 1 ps exhibits two ESA peaks around 500 nm and 590 nm, and a SE signal around 660 nm. These early time results are in agreement with those in a previous study of ESA and SE of curcumin [23].

The transient absorption spectrum of curcumin in methanol undergoes rapid evolution. The ESA band at 600 nm at 1 ps evolves into a negative spectral component starting at $t = 10$ ps. This spectral component, particularly between $t = 20$ ps and $t = 100$ ps (green and blue traces in Figure 3.8a), is attributable to SE. While the initially (1 ps) emissive component at 540 nm evolves into an ESA band at later times

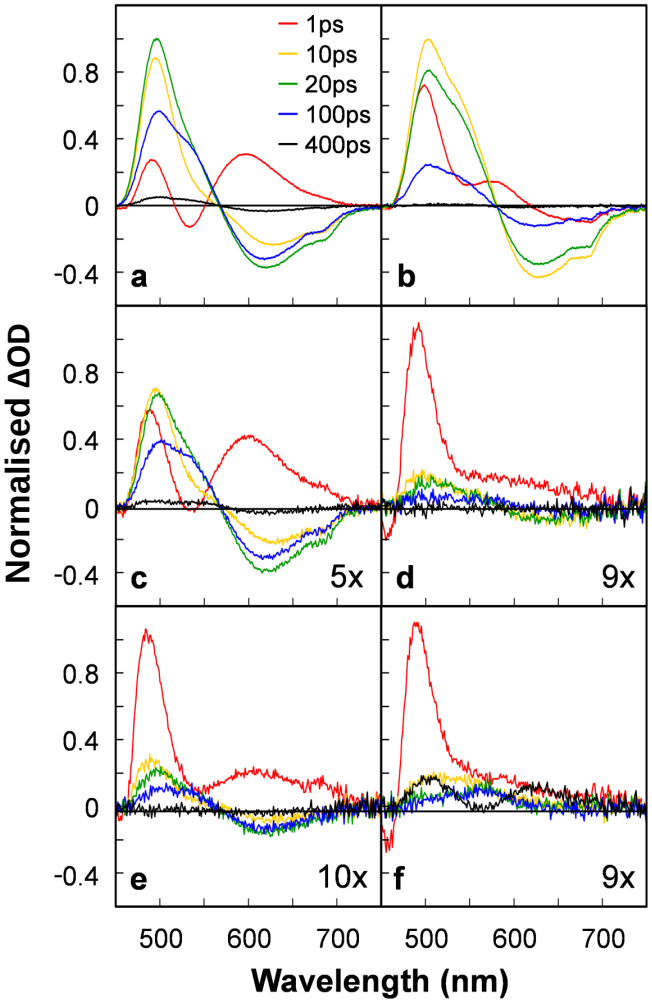

Figure 3.8. Transient absorption spectra of curcumin in (a) methanol and (b) SDS micelles at various time delays; with $[\text{Cu(II)}]_0/[\text{Cur–H}]_0 = 0.5$ (c and d) and $[\text{Cu(II)}]_0/[\text{Cur–H}]_0 = 1$ (e and f) in methanol and SDS micelles, respectively. The spectra are normalised to the maximum ΔOD value of the curcumin only sample.

($t > 10$ ps), the spectral component at 500 nm exhibits ESA exclusively, reflecting the excited state kinetics. The signal increases to a maximum value at 10 ps and then a decay is present thereafter.

The transient absorption spectrum of curcumin in SDS micelles (Figure 3.8b) also exhibits rapid evolution, which occurs significantly faster than that of curcumin in methanol. While the 600-nm ESA band of curcumin in methanol is pronounced at $t = 1$ ps, the ESA band at $t = 1$ ps for curcumin in SDS micelles has undergone a substantial evolution into an SE signal. This signal grows as time increases to 10 ps, producing similar SE signals to those observed for curcumin in methanol at $t = 20$ ps. Because the relaxation dynamics of curcumin in SDS micelles are faster than those in

methanol, the initially observed ($t = 1$ ps) SE signal at 540 nm in methanol is absent in SDS micelles as the signal has evolved rapidly into an ESA band. However, the transient absorption signal at 500 nm for curcumin in SDS micelles exhibits purely ESA, which is similar for curcumin in methanol, and hence offers insight into the excited state kinetics.

3.4.5 Transient Absorption Spectra of the Copper(II)−Curcumin Complexes

The transient absorption spectra of the Cu(II)−Curcumin complexes in methanol and SDS micelles with $[Cu(II)]_0/[Cur-H]_0 = 0.5$ are shown in Figure 3.8c and Figure 3.8d, and $[Cu(II)]_0/[Cur-H]_0 = 1$ in Figure 3.8e and Figure 3.8f, respectively. There are several major differences between these transient absorption spectra and those of curcumin alone. First, the maximum ΔOD signals with $[Cu(II)]_0/[Cur-H]_0 = 0.5$ are approximately five and nine times lower than curcumin in methanol and SDS micelles (Figure 3.8c and Figure 3.8d), respectively. Second, the maximum ΔOD signals of $[Cu(II)]_0/[Cur-H]_0 = 1$ in methanol and SDS micelles (Figure 3.8e and Figure 3.8f) are ten and nine times lower than curcumin alone in methanol and SDS micelles, respectively. Third, the transient absorption spectra of the Cu(II)−Curcumin complexes exhibit significantly faster kinetics than curcumin. For instance, the ESA band of curcumin in SDS micelles at 500 nm exhibits a growth in amplitude from t = 1 ps to t = 10 ps and is followed by a decay of $\sim$ 100 ps (Figure 3.8b). In contrast, the same ESA band for $[Cu(II)]_0/[Cur-H]_0 = 0.5$ in the same solvent has a maximum signal at t = 1 ps, which diminishes to background level by t = 10 ps (Figure 3.8d). Finally, while curcumin shows an appreciable level of SE from 540 – 700 nm (Figure 3.8a and Figure 3.8b), this signal is effectively quenched in the presence of Cu(II) as shown in Figure 3.8c – Figure 3.8f. This efficient quenching of SE is consistent with the data shown in Figure 3.3, in which the steady-state fluorescence of curcumin is quenched by Cu(II).

Although significant differences between the transient absorption spectra of curcumin and the Cu(II)−Curcumin complexes are present, there are also similarities between the spectra in Figure 3.8a (curcumin in methanol) and Figure 3.8c (Cu(II)−Cur-

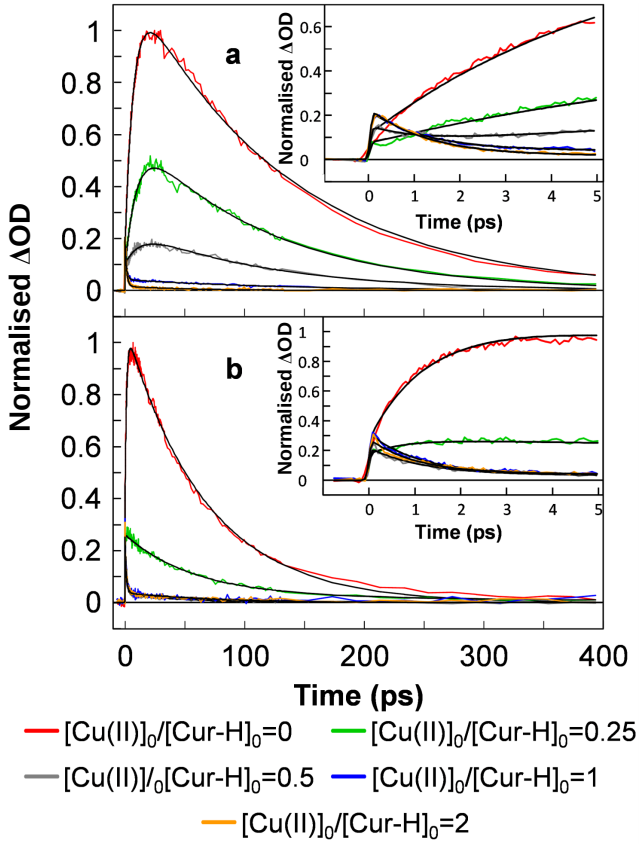

Figure 3.9. Excited state absorption signals of curcumin and Cu(II)−Curcumin complexes at various $[Cu(II)]_0/[Cur–H]_0$ values at 500 nm with 420 nm excitation with $[Cur–H]_0$ = 100 µM in (a) methanol and (b) SDS micelles. The insets show the signals at early time.

cumin complexes in methanol with $[Cu(II)]_0/[Cur{-}H]_0$ = 0.5) due to the presence of free curcumin at $[Cu(II)]_0/\ [Cur{-}H]_0 = 0.5$. The speciation plot in Figure 3.7 shows that approximately 25 % of curcumin are free at $[Cu(II)]_0/[Cur{-}H]_0 = 0.5$ and almost the same level of curcumin is present as $[Cu^{II}{-}Cur]^+$ with the rest (≈50 %) as the 1:2 Cu(II)−Curcumin complex. However, at a higher level Cu(II) concentration, where $[Cu(II)]_0/[Cur{-}H]_0 = 1$, the level of free curcumin is lower than 10 % and hence the transient absorption spectrum (Figure 3.8e) is consistent with this low level of free curcumin.

3.4.6 Excited State Kinetics of Curcumin and the Copper(II)−Curcumin Complexes

The temporal profiles of the 500-nm ESA signals recorded at several $[Cu(II)]_0/[Cur-H]_0$ ratios in methanol and SDS micelles are shown in Figure 3.9. The ESA signals of curcumin in methanol and SDS micelles are best-fitted with a tri-exponential function with two rising components and a decaying component. For the ESA signals of curcumin in the presence of Cu(II), the data are best-fitted with a bi-exponential function with either a rise and a decay ($[Cu(II)]_0/[Cur-H]_0 = 0.25$ and 0.5 in methanol) or two decays ($[Cu(II)]_0/[Cur-H]_0 = 1$ and 2 in methanol and $[Cu(II)]_0/[Cur-H]_0$ = 0.25 – 2 in SDS micelles). The fitting parameters are summarised in Table 3.2.

The insets of Figure 3.9 show that curcumin exhibits a delayed ESA signal at 500 nm (red). The ESA signal of curcumin in methanol shows two growth components with time constants of approximately 0.9 ps and 8.2 ps, with a combined amplitude of approximately 50 %. The growth components in the ESA signal of curcumin in SDS micelles have time constants of around 0.5 ps and 2.5 ps with a combined amplitude of about 45 %. The time constants of the growth components of curcumin in both media are in very good agreement with the solvation time constants of curcumin in these media, which have been determined in previous studies using fluorescence upconversion [23–25]. In addition to the growth components, there is a decay component with a time constant of approximately 125 ps for curcumin in methanol and 65 ps in SDS micelles. These decay time constants show a strong agreement with those reported in previous studies [22–25, 27, 29], which have been assigned to excited state intramolecular hydrogen atom transfer (ESIHT).

In order to examine the excited state kinetics of the Cu(II)−Curcumin complexes, we focus on the ESA of the complexes with $[Cu(II)]_0/[Cur-H]_0 = 2$, where an excess of Cu(II) is present to ensure that curcumin is complexed effectively, which is confirmed by identical kinetics observed at $[Cu(II)]_0/[Cur-H]_0 = 3$, as shown in Figure 3.10. As shown in Table 3.2, the ESA of the Cu(II)−Curcumin complex at $[Cu(II)]_0/[Cur-H]_0 = 2$ exhibits two decay components in both methanol and SDS micelles with time constants of 1.1 – 1.3 ps (> 86 % amplitude) and approximately 60 ps at low amplitudes. However, the origin of this fast and non-radiative kinetic

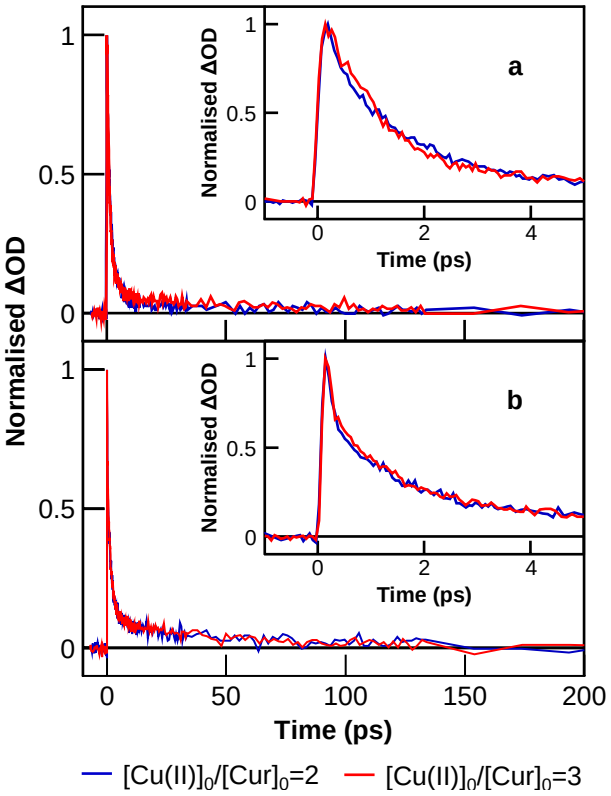

Figure 3.10. Excited state kinetics at 500 nm for $[Cu(II)]_0/[Cur–H]_0$ =2 (blue) and 3 (red) in (a) methanol and (b) SDS micelles with the inset showing the early time decay.

process due to the Cu(II)−Curcumin interaction is unclear. Previous studies suggest that quenching of fluorescence of organic fluorophores in the presence of Cu(II) is attributable to a charge transfer reaction [31, 32].

It is interesting that the temporally integrated magnitude of the ESA transient of curcumin in methanol is ≈ 125 times higher than that of the complex with $[Cu(II)]_0/[Cur{-}H]_0 = 2$. This result is in good agreement with the spectrally integrated result reported earlier (Figure 3.2a), in which a ratio of 135 is obtained. Additional insight is gained by comparing the ESA decay time constant of curcumin (~ 125 ps) and the Cu(II)−Curcumin complex (~ 1.3 ps) in methanol. Given that the molar extinction coefficients of the two species are similar, as shown in Figure 3.2, this result indicates that the fluorescence intensity of the Cu(II)−Curcumin complex is expected to be at least 100 times weaker than that of curcumin.

Table 3.2. Transient Absorption Kinetic Parameters at 500 nm for Different Cu(II) to curcumin Ratios in Methanol and SDS Micelles.[a]

$[Cu(II)]_0/[Cur-H]_0$	Solvent	a_1[b]	τ_1 (ps)	a_2[b]	τ_2 (ps)	a_3[b]	τ_3 (ps)
0	MeOH	-0.07 ± 0.02	0.9 ± 0.3	-0.42 ± 0.01	8.2 ± 0.2	0.51 ± 0.01	125 ± 5
	SDS	-0.27 ± 0.03	0.5 ± 0.1	-0.18 ± 0.02	2.5 ± 0.3	0.55 ± 0.01	65 ± 5
0.25	MeOH	-0.47 ± 0.02	9.4 ± 0.4	0.53 ± 0.01	120 ± 7	–	–
	SDS	0.88 ± 0.04	61 ± 17	0.12 ± 0.03	300 ± 180	–	–
0.5	MeOH	-0.37 ± 0.02	13 ± 2	0.63 ± 0.02	115 ± 15	–	–
	SDS	0.85 ± 0.1	1.2 ± 0.2	0.15 ± 0.02	48 ± 20	–	–
1	MeOH	0.80 ± 0.1	1.0 ± 0.2	0.20 ± 0.02	110 ± 50	–	–
	SDS	0.88 ± 0.08	1.1 ± 0.2	0.12 ± 0.02	76 ± 32	–	–
2	MeOH	0.93 ± 0.05	1.3 ± 0.1	0.07 ± 0.01	63 ± 30	–	–
	SDS	0.86 ± 0.09	1.1 ± 0.2	0.14 ± 0.02	68 ± 30	–	–

[a]The transient absorption traces, $f(t)$, were fitted with the multiexponential function $f(t) = a_1 e^{-t/\tau_2} + a_2 e^{-t/\tau_2} + a_3 e^{-t/\tau_2}$, where $|a_1| + |a_2| + |a_3| = 1$.
[b]The negative amplitude signifies a growth component.

3.4.7 Kinetic Modelling Analysis

By examining the time constants and decay/growth amplitudes of the kinetics observed for the species present at $[Cu(II)]_0/[Cur{-}H]_0 = 0.25$ – 1, the kinetics in this range are composed of those of free curcumin ($[Cu(II)]_0/[Cur{-}H]_0 = 0$) and complexed curcumin ($[Cu(II)]_0/[Cur{-}H]_0 = 2$). Further insight into the rapid non-radiative process in the Cu(II)−Curcumin complexes is provided by analysing the ESA signals of free curcumin and the Cu(II)−Curcumin complexes at 500 nm using a kinetic model. The proposed kinetic model for free curcumin is shown in Figure 3.11a, which includes (1) excitation of curcumin from the ground state, S_0, to a non-equilibrated excited state, $S_1{}^*$, (2) relaxation of the $S_1{}^*$ state to the lowest energy excited state, S_1, by solvation, (3) deactivation of the S_1 state through fluorescence and non-radiative pathways. The delayed ESA observed in curcumin (Figure 3.9) indicates that ESA is followed by solvation. As for the Cu(II)−Curcumin complex, the proposed kinetic model is shown in Figure 3.11b, which includes (1) excitation of the Cu(II)−Curcumin complexes from the ground state, $[Cu^{II}{-}Cur]^+$, to the excited state, $[Cu^{II}{-}Cur]^{+*}$, and (2) a non-radiative relaxation to yield the ground state.

The kinetic modelling analysis is performed on the data for curcumin and the Cu(II) −Curcumin complexes in methanol as a consequence of the well-resolved kinetics and high signal-to-noise ratio of the ESA signal (500 nm). In the analysis, the ESA signals of the samples with $[Cu(II)]_0/[Cur{-}H]_0$ values ranging from 0.25 to 1 are fitted with a linear combination of two ESA signals, which are those of free curcumin ($[Cu(II)]_0/[Cur{-}H]_0 = 0$) and complexed curcumin ($[Cu(II)]_0/[Cur{-}H]_0 = 2$), as follows.

$$\mathrm{ESA}_x(t) = \alpha\ \mathrm{ESA}_{\mathrm{complexed}}(t) + (1-\alpha)\mathrm{ESA}_{\mathrm{curcumin}}(t) \tag{3.9}$$

where $[Cu(II)]_0/[Cur{-}H]_0 = x$, and $0.25 \leq x \leq 1$. The parameter α is the fraction of complexed curcumin. The fits of the ESA signals to Equation (3.9) and the experimental data are shown in Figure 3.11c. All the α values, which are summarised in Table 3.3 exhibit reasonable agreement with the speciation of complexed and free curcumin as also shown in Figure 3.7.

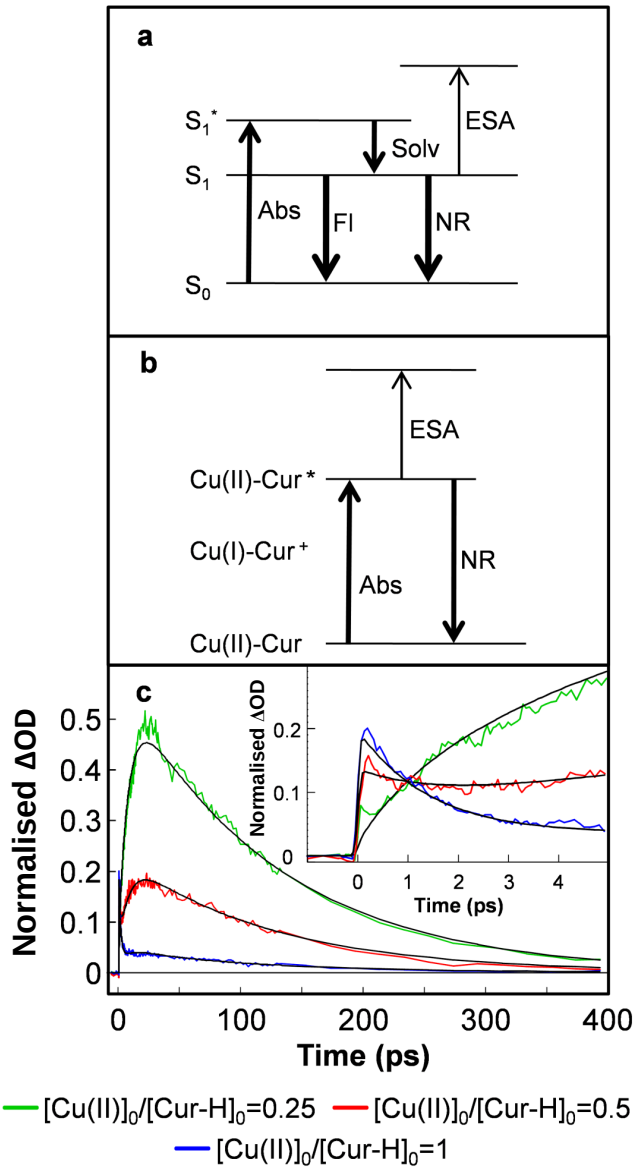

Figure 3.11. Proposed kinetic models for (a) curcumin and (b) the Cu(II)−Curcumin complexes, where Abs: absorption; Solv: solvation, ESA: excited state absorption, Fl: fluorescence, NR: non-radiative transition. (c) The excited state absorption signals of the Cu(II)−Curcumin complexes with $[Cu(II)]_0/[Cur–H]_0 = 0.25$ to 1 are expressed as a linear combination of those of free curcumin and fully complexed curcumin ($[Cu(II)]_0/[Cur–H]_0 = 2$).

Table 3.3. Summary of Linear Combination Kinetic Fitting.

$[Cu(II)]_0/[Cur–H]_0$	Free Cur (%) (1-α)	Bound Cur (%) (α)
0	100	0
0.25	82 ± 2	18 ± 38
0.5	21 ± 1	79 ± 15
0.75	2 ± 1	98 ± 5
1	3 ± 1	97 ± 11
2	0	100

3.5 Conclusions

We have used fluorescence quenching of curcumin by Cu(II) to determine the complexation constant of $[Cu^{II}-Cur]^{+}$ and $[Cu^{II}-Cur_2]$ in methanol and SDS micelles. The formation of $[Cu^{II}-Cur]^{+}$ is favoured over $[Cu^{II}-Cur_2]$ in methanol while both complexes are formed in SDS micelles up to $[Cu(II)]_0/[Cur-H]_0$ value of 2 in this study. We have also elucidated the excited state kinetics of curcumin and the Cu(II)−Curcumin complexes in methanol and SDS micelles using time-resolved transient absorption spectroscopy. While the excited state kinetics of curcumin include solvation and excited state intramolecular hydrogen atom transfer, the Cu(II)−Curcumin complexes exhibit a fast and non-radiative kinetic process with an approximately 1 ps time constant.

3.6 References

(1) Anand, P.; Thomas, S. G.; Kunnumakkara, A. B.; Sundaram, C.; Harikumar, K. B.; Sung, B.; Tharakan, S. T.; Misra, K.; Priyadarsini, I. K.; Rajasekharan, K. N.; Aggarwal, B. B. Biological Activities of Curcumin and Its Analogues (Congeners) Made by Man and Mother Nature. *Biochem. Pharmacol.* **2008**, *76*, 1590–1611.

(2) Aggarwal, B. B.; Kumar, A.; Bharti, A. C. Anticancer Potential of Curcumin: Preclinical and Clinical Studies. *Anticancer Res.* **2003**, *23*, 363–398.

(3) Yang, F. S.; Lim, G. P.; Begum, A. N.; Ubeda, O. J.; Simmons, M. R.; Ambegaokar, S. S.; Chen, P. P.; Kayed, R.; Glabe, C. G.; Frautschy, S. A.; Cole, G. M. Curcumin Inhibits Formation of Amyloid β Oligomers and Fibrils, Binds Plaques, and Reduces Amyloid *in Vivo*. *J. Biol. Chem.* **2005**, *280*, 5892–5901.

(4) Egan, M. E.; Pearson, M.; Weiner, S. A.; Rajendran, V.; Rubin, D.; Glockner-Pagel, J.; Canny, S.; Du, K.; Lukacs, G. L.; Caplan, M. J. Curcumin, a Major Constituent of Turmeric, Corrects Cystic Fibrosis Defects. *Science* **2004**, *304*, 600–602.

(5) Lantz, R. C.; Chen, G. J.; Solyom, A. M.; Jolad, S. D.; Timmermann, B. N. The Effect of Turmeric Extracts on Inflammatory Mediator Production. *Phytomedicine* **2005**, *12*, 445–452.

(6) Ruby, A.; Kuttan, G.; Babu, K. D.; Rajasekharan, K.; Kuttan, R. Anti-Tumour and Antioxidant Activity of Natural Curcuminoids. *Cancer Lett.* **1995**, *94*, 79–83.

(7) Gopinath, D.; Ahmed, M. R.; Gomathi, K.; Chitra, K.; Sehgal, P. K.; Jayakumar, R. Dermal Wound Healing Processes with Curcumin Incorporated Collagen Films. *Biomaterials* **2004**, *25*, 1911–1917.

(8) Shi, M.; Cai, Q.; Yao, L.; Mao, Y.; Ming, Y.; Ouyang, G. Antiproliferation and Apoptosis Induced by Curcumin in Human Ovarian Cancer Cells. *Cell Biol. Int.* **2006**, *30*, 221–226.

(9) Chan, W.-H.; Wu, H.-J. Anti-Apoptotic Effects of Curcumin on Photosensitized Human Epidermal Carcinoma A431 Cells. *J. Cell. Biochem.* **2004**, *92*, 200–212.

(10) Koon, H. K.; Leung, A. W. N.; Yue, K. K. M.; Mak, N. K. Photodynamic Effect of Curcumin on NPC/CNE2 Cells. *J. Environ. Pathol. Toxicol. Oncol.* **2006**, *25*, 205–216.

(11) Park, K.; Lee, J.-H. Photosensitizer Effect of Curcumin on UVB-Irradiated HaCaT Cells through Activation of Caspase Pathways. *Oncol. Rep.* **2007**, *17*, 537–540.

(12) Yoshino, M.; Haneda, M.; Naruse, M.; Htay, H. H.; Tsubouchi, R.; Qiao, S. L.; Li, W. H.; Murakami, K.; Yokochi, T. Prooxidant Activity of Curcumin: Copper-Dependent Formation of 8-Hydroxy-2-Deoxyguanosine in DNA and Induction of Apoptotic Cell Death. *Toxicol. in Vitro* **2004**, *18*, 783–789.

(13) Ahsan, H.; Hadi, S. M. Strand Scission in DNA Induced by Curcumin in the Presence of Cu(II). *Cancer Lett.* **1998**, *124*, 23–30.

(14) Baum, L.; Ng, A. Curcumin Interaction with Copper and Iron Suggests One Possible Mechanism of Action in Alzheimer's Disease Animal Models. *J. Alzheimers Dis.* **2004**, *6*, 367–377.

(15) Ahsan, H.; Parveen, N.; Khan, N. U.; Hadi, S. M. Pro-Oxidant, Anti-Oxidant and Cleavage Activities on DNA of Curcumin and Its Derivatives Demethoxycurcumin and Bisdemethoxycurcumin. *Chem. Biol. Interact.* **1999**, *121*, 161–175.

(16) Bush, A. I.; Pettingell, W. H.; Multhaup, G.; d Paradis, M.; Vonsattel, J. P.; Gusella, J. F.; Beyreuther, K.; Masters, C. L.; Tanzi, R. E. Rapid Induction of Alzheimer Aβ Amyloid Formation by Zinc. *Science* **1994**, *265*, 1464–1467.

(17) Lovell, M. A.; Robertson, J. D.; Teesdale, W. J.; Campbell, J. L.; Markesbery, W. R. Copper, Iron and Zinc in Alzheimer's Disease Senile Plaques. *J. Neurol. Sci.* **1998**, *158*, 47–52.

(18) Syme, C. D.; Nadal, R. C.; Rigby, S. E. J.; Viles, J. H. Copper Binding to the Amyloid-β (Aβ) Peptide Associated with Alzheimer's Disease: Folding, Coordination Geometry, pH Dependence, Stoichiometry, and Affinity of Aβ-(1-28): Insights from a Range of Complementary Spectroscopic Techniques. *J. Biol. Chem.* **2004**, *279*, 18169–18177.

(19) Girolami, G. S.; Jeffries, P. M.; Dubois, L. H. Mechanistic Studies of Copper Thin-Film Growth from Cu(I) and Cu(II) β-Diketonates. *J. Am. Chem. Soc.* **1993**, *115*, 1015–1024.

(20) Shin, H. K.; Chi, K. M.; Farkas, J.; Hampden-Smith, M. J.; Kodas, T. T.; Duesler, E. N. Chemistry of Copper(I) β-Diketonate Complexes. 2. Synthesis, Characterization, and Physical Properties of (β-Diketonato)Copper(I) Trimethylphosphine and Bis(Trimethylphosphine) Complexes. *Inorg. Chem.* **1992**, *31*, 424–431.

(21) Addicoat, M. A.; Metha, G. F.; Kee, T. W. Density Functional Theory Investigation of Cu(I)- and Cu(II)-Curcumin Complexes. *J. Comput. Chem.* **2011**, *32*, 429–438.

(22) Kee, T. W.; Adhikary, R.; Carlson, P. J.; Mukherjee, P.; Petrich, J. W. Femtosecond Fluorescence Upconversion Investigations on the Excited-State Photophysics of Curcumin. *Aust. J. Chem.* **2011**, *64*, 23–30.

(23) Ghosh, R.; Mondal, J. A.; Palit, D. K. Ultrafast Dynamics of the Excited States of Curcumin in Solution. *J. Phys. Chem. B* **2010**, *114*, 12129–12143.

(24) Adhikary, R.; Carlson, P. J.; Kee, T. W.; Petrich, J. W. Excited-State Intramolecular Hydrogen Atom Transfer of Curcumin in Surfactant Micelles. *J. Phys. Chem. B* **2010**, *114*, 2997–3004.

(25) Adhikary, R.; Mukherjee, P.; Kee, T. W.; Petrich, J. W. Excited-State Intramolecular Hydrogen Atom Transfer and Solvation Dynamics of the Medicinal Pigment Curcumin. *J. Phys. Chem. B* **2009**, *113*, 5255–5261.

(26) Protonic, T. A., *Software*; Leeds, UK, www.hyperquad.co.uk.

(27) Khopde, S. M.; Indira Priyadarsini, K.; Palit, D. K.; Mukherjee, T. Effect of Solvent on the Excited-State Photophysical Properties of Curcumin. *Photochem. Photobiol.* **2000**, *72*, 625–631.

(28) Melo, E. C.; Costa, S. M.; Maçanita, A. L.; Santos, H. The Use of the N-(9-Anthroyloxy) Stearic Acid to Probe the Water Content of Sodium Dodecyl Sulfate, Dodecyltimethylammonium Chloride, and Triton X-100 Micelles. *J. Colloid Interface Sci.* **1991**, *141*, 439–453.

(29) Nardo, L.; Paderno, R.; Andreoni, A.; Másson, M.; Haukvik, T.; Tønnesen, H. H. Role of H-Bond Formation in the Photoreactivity of Curcumin. *Spectroscopy* **2008**, *22*, 187–198.

(30) Wang, Z. F.; Leung, M. H. M.; Kee, T. W.; English, D. S. The Role of Charge in the Surfactant-Assisted Stabilization of the Natural Product Curcumin. *Langmuir* **2010**, *26*, 5520–5526.

(31) Fabbrizzi, L.; Licchelli, M.; Pallavicini, P.; Perotti, A.; Taglietti, A.; Sacchi, D. Fluorescent Sensors for Transition Metals Based on Electron-Transfer and Energy-Transfer Mechanisms. *Chem. Eur. J.* **1996**, *2*, 75–82.

(32) Fan, L.-J.; Martin, J. J.; Jones, W. E. Competition Between Energy Transfer Quenching and Chelation Enhanced Fluorescence in a Cu (II) Coordinated Conjugated Polymer System. *J. Fluoresc.* **2009**, *19*, 555–559.

(33) Petter, R. C.; Salek, J. S.; Sikorski, C. T.; Kumaravel, G.; Lin, F. T. Cooperative Binding by Aggregated Mono-6-(Alkylamino)-β-Cyclodextrins. *J. Am. Chem. Soc.* **1990**, *112*, 3860–3868.

(34) Weiss, J. N. The Hill Equation Revisited: Uses and Misuses. *FASEB J.* **1997**, *11*, 835–41.

(35) McKee, D. J.; Frieden, E. Binding of Transition Metal Ions by Ceruloplasmin (Ferroxidase). *Biochemistry* **1971**, *10*, 3880–3883.

CHAPTER 4

REDUCTION OF COPPER(II) TO COPPER(I) IN THE COPPER–CURCUMIN COMPLEX INDUCES DECOMPOSITION OF CURCUMIN

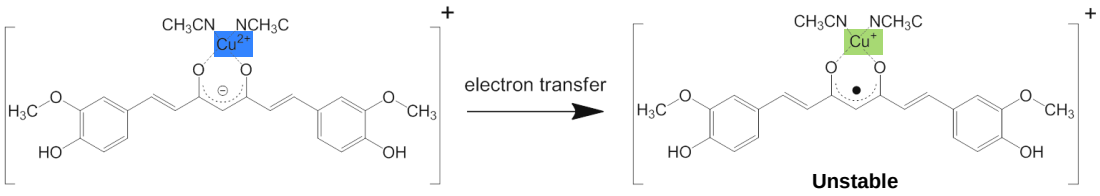

Leung, M. H. M.; Mohan, P.; Pukala, T. L.; Scanlon, D. B.; Lincoln, S. F.; Kee, T. W. Reduction of Copper(II) to Copper(I) in the Copper–Curcumin Complex Induces Decomposition of Curcumin. *Aust. J. Chem.* **2012**, *65*, 490–495. `http://www.publish.csiro.au/nid/51/paper/CH12081.htm`

Statement of Authorship

By signing the Statement of Authorship, each author certifies that their stated contribution to the following publication is accurate and that permission is granted for the publication to be included in this thesis.

Leung, M. H. M.; Mohan, P.; Pukala, T. L.; Scanlon, D. B.; Lincoln, S. F.; Kee, T. W., Reduction of Copper(II) to Copper(I) in the Copper−Curcumin Complex Induces Decomposition of Curcumin. *Aust. J. Chem.* **2012**, *65*, 490–495.

Author Contributions

Name of First Author (Candidate)	Mandy H. M. Leung
Contribution to the Paper	Data Collection and analysis on UV-visible absorption and fluorescence emission data Sample preparation for mass spectrometry and HPLC Preparation and editing of manuscript
Signature	
Date	01/09/2014
Name of Co-Author	Pravena Mohan
Contribution to the Paper	Data collection on UV-visible absorption
Signature	
Date	2/09/2014
Name of Co-Author	Dr. Tara L. Pukala
Contribution to the Paper	Collection and analysis of the mass spectra Editing of manuscript - Mass spectrometry
Signature	
Date	02/09/2014
Name of Co-Author	Dr. Denis B. Scanlon
Contribution to the Paper	Collection and analysis of the HPLC chromatograms Editing of manuscript - HPLC
Signature	
Date	01/09/2014

Name of Co-Author	Prof. Stephen F. Lincoln
Contribution to the Paper	Supervision of the candidate Editing of manuscript
Signature	
Date	01/09/2014

Name of Co-Author	Dr. Tak W. Kee
Contribution to the Paper	Supervision of the candidate Preparation and editing of manuscript Corresponding Author
Signature	
Date	01/09/2014

4.1 Abstract

We report the decomposition of curcumin due to reduction of Cu(II) to Cu(I). Cu(II) binds tightly with curcumin to form a complex which exhibits a high stability in methanol, but it decomposes readily in acetonitrile and in SDS micelles in the presence of ascorbic acid, coincident with reduction of Cu(II) to Cu(I). In this study, the UV-visible absorption of the Cu(II)−Curcumin complex shows a monotonic decrease as a function of time, consistent with the decomposition of curcumin. At a high Cu(II):Curcumin molar ratio of 10:1, the UV-visible absorption spectrum of the Cu(II)−Curcumin complex in acetonitrile exhibits a substantial blue shift of the absorption maximum from 420 nm to 350 nm, which is indicative of a significant decrease in conjugation length of curcumin in the presence of Cu(II). Time-dependent mass spectrometry and high performance liquid chromatography data are also consistent with the decomposition of curcumin as a consequence of reduction of Cu(II) to Cu(I).

4.2 Introduction

Curcumin is a naturally occurring yellow pigment in the Indian spice plant turmeric [1]. It exists either as the keto-enol, and the diketo tautomer, as shown in Figures 4.1a and 4.1b. A recent study showed that the keto-enol tautomer predominates in several organic solvents [2]. Curcumin has shown effectiveness in treating several of diseases, including cancer [3–10], Alzheimer's [11], and cystic fibrosis [12]. In particular, the anticancer properties of curcumin have generated intense interests as its medicinal characteristics are accompanied by virtually no side effects [13–15], which is in stark contrast to conventional chemotherapy agents. Recent clinical trials have been conducted to assess the effectiveness of curcumin as an anti-cancer agent. [16, 17].

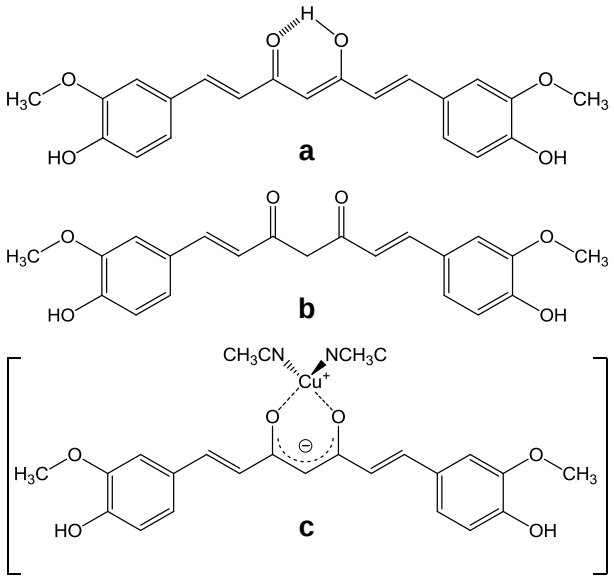

Figure 4.1. Chemical structure of the (a) keto-enol tautomer of curcumin, (b) diketo tautomer of curcumin, and (c) 1:1 Cu(I)−Curcumin complex.

Recently, studies have shown that the interaction between curcumin and Cu(II) may be a very important aspect of the anticancer properties of curcumin [18–25]. First, it was demonstrated that an elevated level of Cu(II) is found in tumours [26]. Second, studies showed that curcumin has the ability to damage the DNA of cancer cells in the presence of Cu(II) [18–21]. It has been proposed that a series of reactions including reduction of Cu(II) to Cu(I), oxidation of curcumin, and generation of superoxide, hydrogen peroxide, and hydroxyl radicals are involved [22]. As a consequence, devel-

oping a good understanding of the behaviour of curcumin in the presence of Cu(II) is fundamental and will lead to insight into the anticancer properties of curcumin.

We have used fluorescence spectroscopy to determine the binding constants of the 1:1 and 1:2 Cu(II)−Curcumin complexes ($[Cu^{II}-Cur]^{+}$ and $[Cu^{II}-Cur_2]$) in methanol and sodium dodecyl sulphate (SDS) micelles. Cu(II) exhibits a high efficiency in quenching the fluorescence of curcumin, which enables the determination of binding constants of $K_1 = (1.33 \pm 0.47) \times 10^8\ M^{-1}$, $K_2 = (6.79 \pm 1.77) \times 10^5\ M^{-1}$, and $K_1 = (9.90 \pm 1.68) \times 10^5\ M^{-1}$, $K_2 = (1.70 \pm 0.48) \times 10^6\ M^{-1}$, respectively, in methanol and SDS micelles [27]. In addition, we have used femtosecond transient absorption spectroscopy to investigate their excited state kinetics [27]. In the binding process, formation of a β-diketonate by deprotonation of the hydroxyl group in the keto-enol tautomer of curcumin (Figure 4.1a) is essential to produce a strong, bidentate chelation with Cu(II) [28, 29]. A recent study revealed that curcumin forms stable complexes with Cu(II) in two different square planar geometries to give the $[Cu^{II}-Cur]^{+}$ and $[Cu^{II}-Cur_2]$ [30].

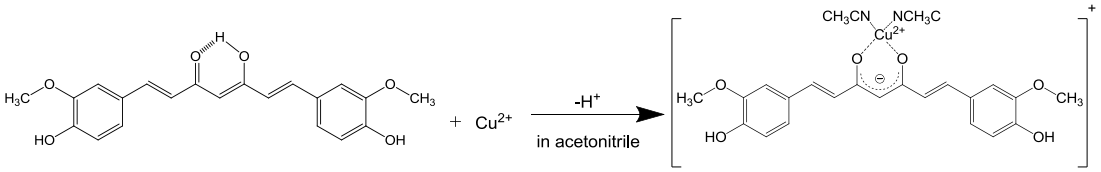

Scheme 4.1. Formation of Cu(II)−Curcumin complex.

In this study, we investigate the effect of reducing Cu(II) to Cu(I) on the stability of the Cu(I)−Curcumin complex in acetonitrile (Figure 4.1c) and SDS micelles. The formation of the Cu(II)−Curcumin complex in acetonitrile is shown in Scheme 4.1. Our time dependent UV-visible absorption results indicate decomposition of curcumin in the Cu(II)−Curcumin complex as a result of the Cu(II) to Cu(I) reduction. Time-dependent mass spectrometry and high performance liquid chromatography (HPLC) studies also produce data consistent with this process. In addition to curcumin decomposition, a significant blue shift of the UV-visible absorption maximum of the Cu(II)−Curcumin complex in acetonitrile from 420 nm to 350 nm was observed at a Cu(II):Curcumin molar ratio of 10:1, consistent with an increasing complexation and formation of the curcumin diketo tautomer as a result of the interaction with Cu(II).

4.3 Materials and Methods

4.3.1 Materials

Curcumin (purity $> 98\,\%$) was obtained from LKT Laboratories. Sodium dodecyl sulphate (SDS, purity $\geq 99\,\%$ by GC Assay) was obtained from Fluka. Methanol (AR Grade, purity $\geq 99.5\,\%$) and acetonitrile (HPLC grade, purity $\geq 99.7\,\%$) were obtained from Merck and Scharlau, respectively. Copper (II) sulphate pentahydrate (ACS reagent, crystalline, purity $\geq 98\,\%$), L-ascorbic acid (reagent grade, crystalline, purity $\geq 98\,\%$), tetrakis(acetonitrile)copper(I) hexafluorophosphate (ACS reagent, purity $\geq 97\,\%$), and trifluoroacetic acid (ReagentPlus, purity 99 %) were obtained from Sigma Aldrich. All aqueous solutions were prepared using deionised water from a Millipore Milli-Q NANO pure water system.

4.3.2 UV-visible Absorption and Fluorescence Studies

UV-visible absorption spectra were recorded from 300 – 600 nm using a Cary 5000 UV-visible/NIR spectrophotometer (Varian). The time dependent UV-visible absorption spectra were obtained using kinetic mode of the data acquisition software at either 30 min or 1 h intervals. A stock solution of 2.7 mM ($1\,\mathrm{mg\,mL^{-1}}$) curcumin in methanol was used. A micellar solution of 16.2 mM SDS was prepared in a pH 7.4 phosphate buffer solution (50 mM). The SDS concentration was twice the critical micelle concentration to ensure formation of micelles. An 11-µL aliquot of the curcumin stock was added to 3 mL of the SDS micellar solution, acetonitrile or methanol to achieve a final concentration of 10 µM for curcumin. For the UV-visible absorption studies with Cu(II), a stock solution of 10 mM copper (II) sulphate pentahydrate in deionised water was used. To achieve a Cu(II) concentration of 10, 20 or 100 µM, aliquots of 3, 6 or 30 µL of the Cu(II) stock was added to the appropriate 3-mL 10 µM curcumin solution above. The resulting water content due to additions of Cu(II) is $\leq 1\,\%$ v/v. For the UV-visible absorption studies with Cu(I), a stock solution of 10 mM tetrakis(acetonitrile)copper(I) hexafluorophosphate in acetonitrile was used. In the studies with ascorbic acid, a 1 mM solution of L-ascorbic acid was first prepared in the SDS micellar solution. An 11-µL aliquot of the curcumin stock was then added to

3 mL of the SDS micellar solution with 1 mM L-ascorbic acid. For the copper titration experiment, 2mL of 10 µM curcumin in acetonitrile was prepared as mentioned above. Solution of either 1 mM of tetrakis(acetonitrile)copper(I) hexafluorophosphate in acetonitrile or $CuSO_4$ in water were used as stock. Aliquots of the copper stock were added (2 µL per addition) to yield 1-µM increments. UV-visible spectra of curcumin in the presence of 0 – 20 µM Cu(I) and 0 – 30 µM Cu(I) of Cu(II) were collected. Solutions of curcumin with different Cu(I) or Cu(II) concentrations remained clear within the experimental time frame.

Fluorescence spectra were recorded from 430 – 750 nm using a Cary Eclipse Fluorescence spectrometer (Varian). The excitation wavelengths used were 417 and 415 nm for the Cu(I) and Cu(II) titration experiments, respectively, with both excitation and emission slit widths set at 5 nm. A solution of 2.7 mM (1 mg mL^{-1}) curcumin in methanol was used as stock. Solution of 1 mM of Cu(I) in acetonitrile or Cu(II) in water were used as stock. A 7.4-µL aliquot of the curcumin stock was added to 2 mL of acetonitrile to achieve a final concentration of 10 µM curcumin. Aliquots of the Cu(I)/Cu(II) stock (2 µL per addition) were added to 2 mL of 10 µM curcumin in acetonitrile to yield 1-µM increments. Fluorescence spectra of 10 µM curcumin in acetonitrile were collected in the presence of 0 – 10 µM tetrakis(acetonitrile)copper(I) hexafluorophosphate and 0 – 30 µM of $CuSO_4$. All solutions remained clear with each addition of copper solution.

4.4 Results and Discussion

4.4.1 Time-dependent UV-visible Absorption Spectra of the Copper−Curcumin Complex

The UV-visible spectra of 10 µM curcumin in the presence of Cu(II) at 10, 20 and 100 µM in acetonitrile are shown in Figures 4.2a – 4.2c, respectively. First, with a Cu(II) concentration of 20 µM (Figure 4.2b), the UV-visible absorption spectrum of curcumin in acetonitrile exhibits a gradual decay, indicating decomposition of curcumin. Interestingly, the decomposition of curcumin in the presence of Cu(II) is solvent dependent and no evidence of decomposition was observed in methanol, as depicted in Figure 4.2d. This solvent dependent behaviour is discussed below. The decomposition of curcumin becomes significantly more pronounced as the Cu(II) concentration is increased, as a comparison of the data for 10 µM, 20 µM and 100 µM Cu(II) shows (Figures 4.2a – 4.2c). In our studies, Cu(II):Curcumin molar ratios of 1:1 to 10:1 are used to investigate the effect and extent of Cu(II) association.

Figure 4.2a also shows the absorption spectrum of 10 µM curcumin in acetonitrile (dashed curve). While the maximum absorption wavelength and the shape of the absorption spectrum are virtually identical for curcumin and the Cu(II)−Curcumin complex at 1:1 molar ratio, increasing the Cu(II):Curcumin molar ratio from 2:1 to 10:1 changes the shape of the UV-visible absorption spectrum and blue-shifts the absorption maximum from 420 nm for the Cu(II):Curcumin molar ratio of 2:1 (Figure 4.2b) to 350 nm at a 10:1 molar ratio (Figure 4.2c). This blue shift is consistent with a decrease in the conjugation length of curcumin as a consequence of complexation, which is possibly due to conversion of the keto-enol tautomer (Figure 4.1a) to the diketo tautomer (Figure 4.1b). The conjugation length of the diketo tautomer is significantly shorter by comparison with the keto-enol tautomer and therefore a significant blue shift in its UV-visible absorption spectrum is expected. The conjugation length of the diketo form of curcumin is similar to that of half curcumin [31], which has a peak absorption wavelength of $\sim$ 350 nm. While the emergence of the UV-visible absorption spectrum peak at 350 nm has been observed in the aqueous environment [32, 33], it is important to stress that the blue shift in the absorption spectrum and decomposition of curcumin

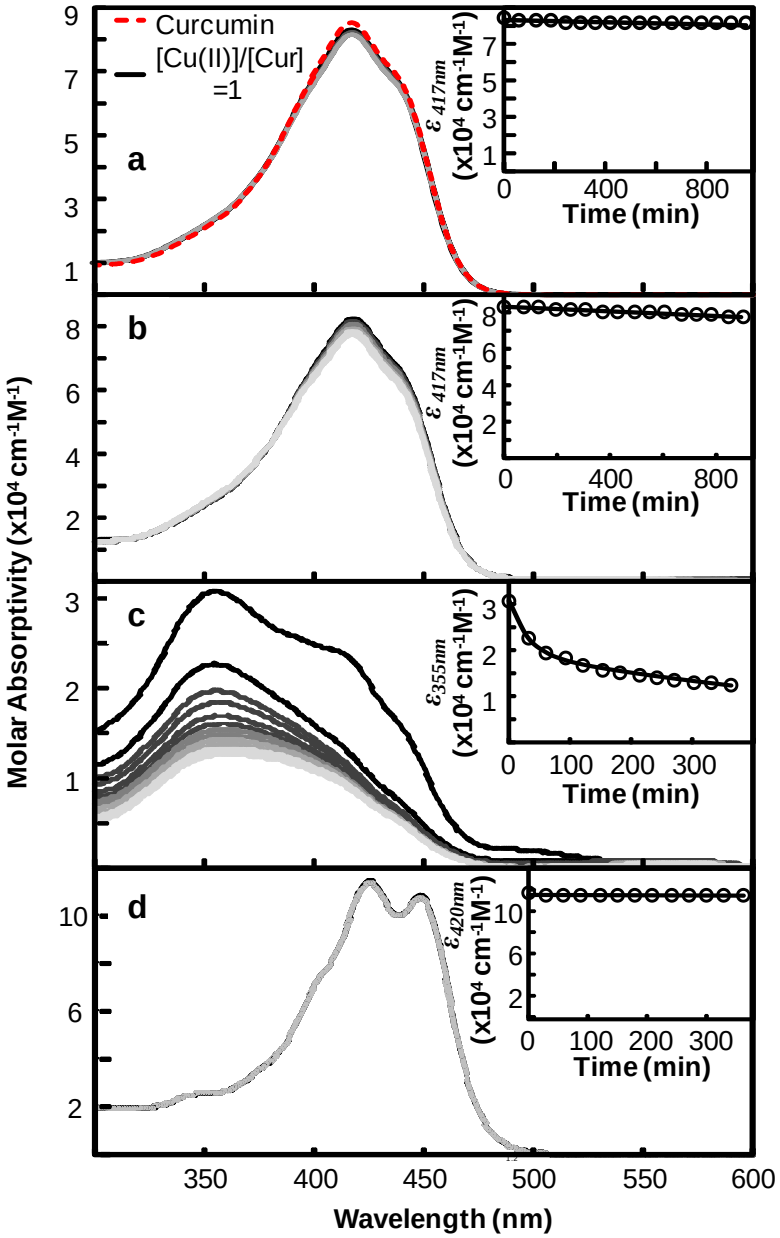

Figure 4.2. UV-visible absorption spectra of 10 µM curcumin in acetonitrile in the presence of (a) 0 µM Cu(II) (dashed), 20 µM Cu(II) (solid) over 14 h, (b) 20 µM Cu(II) over 14 h, (c) 100 µM Cu(II) over 6 h and (d) 10 µM curcumin in methanol in the presence of 10 µM Cu(II) over 6 h. The insets show the decrease of the absorption maxima as a function of time.

in Figure 4.2c are attributable to the presence of Cu(II) in acetonitrile but are unrelated to the presence of a low quantity (≤ 1 % v/v) of water. The absence of any degradation of curcumin in acetonitrile with 3 µL of water, as shown in Figure 4.3a, indicates that curcumin is very stable in the presence of a small amount of water. However, in the presence of Cu(II), curcumin exhibits a high level of degradation, as shown in Figure 4.2c Therefore it is clear that the degradation of curcumin is attributed to the presence of Cu(II) and unrelated to the presence of a small quantity of water. As for the decomposition of curcumin in the presence of Cu(II), there is a solvent dependence on the blue shift of the UV-visible absorption spectrum due to interaction with copper. While this blue shift is pronounced in acetonitrile, there is a smaller change in the UV-visible absorption spectrum in methanol and the decomposition of curcumin is negligible which is probably a reflection of the different ligating properties of acetonitrile and methanol in the Cu(II)−Curcumin complex and a consequent difference in the redox properties of the Cu(II)/Cu(I) couple.

It is evident that the decomposition kinetics of curcumin, as shown in Figure 4.2,

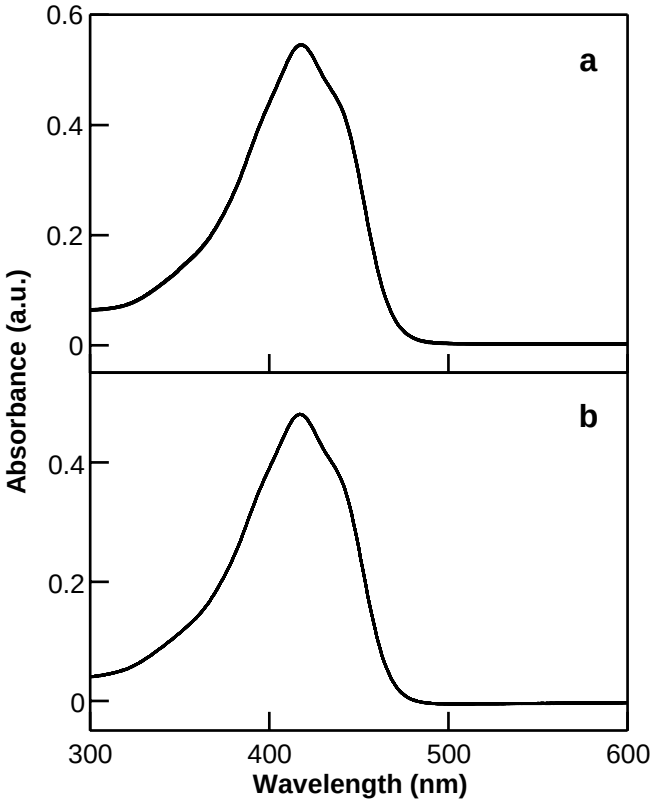

Figure 4.3. UV-visible absorption spectra of 10 µM curcumin in acetonitrile (3 mL) with (a) 20 µL of water and (b) 20 µM Cu(I) over 5 h.

involve multiple time constants. Owing to the presence of long decay, complete decomposition was not observed within the experimental time frame.

4.4.2 Reduction of Cu(II) to Cu(I) in Acetonitrile

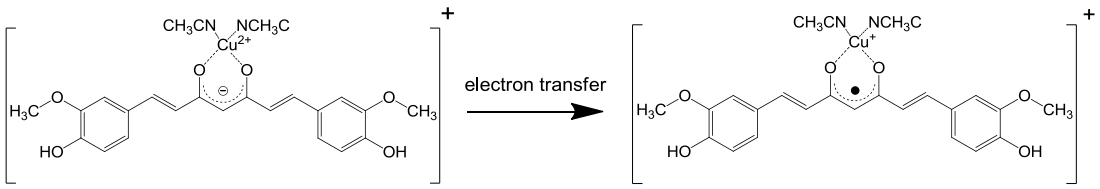

Scheme 4.2. Redox process in Cu(II)−Curcumin complex.

To develop insight into the solvent dependence of the decomposition and blue shift of UV-visible absorption of curcumin in the presence of Cu(II), an understanding of the oxidation state change of copper as a function of solvent variation is required. It is well understood that Cu(II) coordinates with six water ligands in a tetragonally distorted octahedral stereochemistry in water. The same coordination stereochemistry applies to Cu(II) in methanol. In addition, Cu(II) coordinates with several bidentate ligands to form complexes in a slightly distorted square planar structure. The Cu(II) state is highly favoured in water such that even when Cu(I) is added to water it disproportionates to Cu(II) and Cu metal spontaneously [34].

In acetonitrile, however, Cu(I) is stabilised significantly by comparison with Cu(II) [34, 35]. This behaviour is relevant to the decomposition of curcumin in the presence of Cu(II) in acetonitrile. When Cu(II) is added to a solution of curcumin in acetonitrile, the initial complexation of Cu(II) occurs (Scheme 4.1) and subsequently an internal reduction of Cu(II) to Cu(I) occurs and curcumin is oxidised to a curcumin radical which decomposes and $[Cu(NCCH_3)_4]^+$ is formed. To verify this hypothesis, we conducted a control study whereby tetrakis(acetonitrile)copper(I) hexafluorophosphate was added to a solution of 10 µM curcumin in acetonitrile to give a 2:1 Cu(I):Curcumin ratio. The UV-visible absorption spectrum of this solution was recorded over 10 h as shown in Figure 4.3b. All the spectra are well overlapped which shows no evidence of curcumin decomposition and clearly indicating that in the absence of Cu(II) and the redox process shown in Scheme 4.2, curcumin is stable in the presence of Cu(I). Interestingly, the spectral shape of curcumin in the presence of Cu(I) resemble that of curcumin with

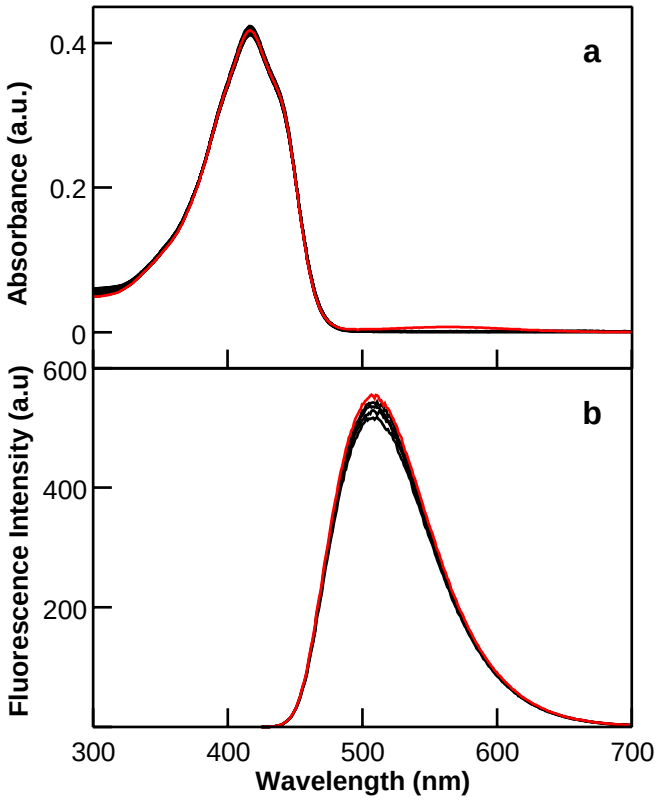

Figure 4.4. (a) UV-visible absorption spectra and (b) fluorescence emission spectra with excitation wavelength of 417 nm of a 10 µM curcumin in acetonitrile solution in the presence of 0 – 20 µM Cu(I) . Red traces represent 0 µM of Cu(I).

addition of water (Figure 4.3a) which indicate there is weak interaction between curcumin and Cu(I). The interaction between curcumin and Cu(I) is further investigated and the UV-visible absorption and fluorescence emission results are presented in Figure 4.4a and Figure 4.4b, respectively. The spectra of curcumin in the presence of Cu(I) in acetonitrile are almost identical to those of curcumin without Cu(I) (shown as red trace in Figure 4.4). The slight changes with increased Cu(I) concentration in the fluorescence emission spectra (Figure 4.4b) are consistent with any interaction between Cu(I) and water being weak. Furthermore, it is well known that the fluorescence quantum yield of curcumin decreases substantially in aqueous environment as water quenches the fluorescence emission efficiently [31, 36, 37]. In contrast, Figure 4.5a shows the UV-visible absorption spectrum of curcumin with an increasing concentration of Cu(II) in acetonitrile, however, shows a substantial spectral change, most notably a blue shift in absorption maximum from 420 nm to 350 nm and a decrease in absorptivity. In addition, the fluorescence of curcumin is effectively quenched by

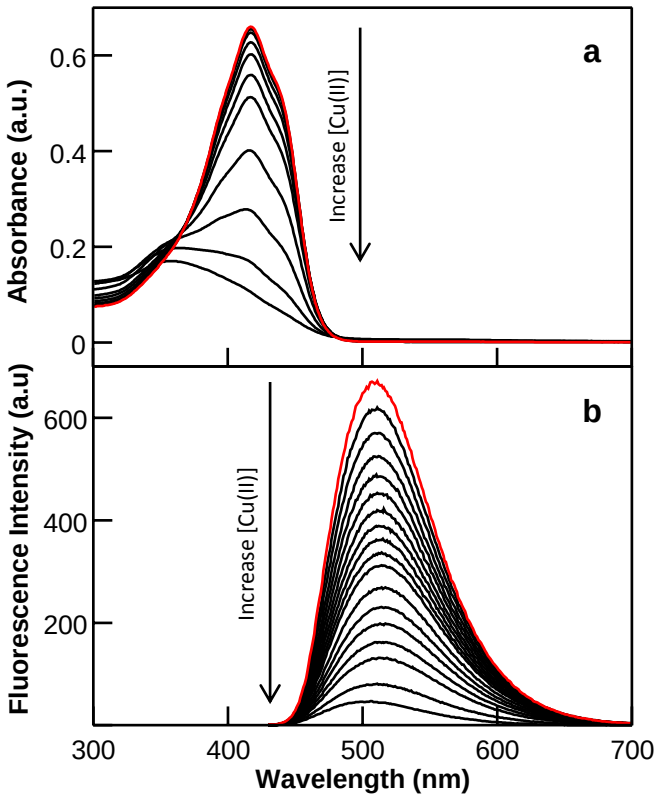

Figure 4.5. (a) UV-visible absorption spectra and (b) fluorescence emission spectra with excitation wavelength of 415 nm of a 10 µM curcumin in acetonitrile solution in the presence of 0 – 30 µM Cu(II). Red traces represent 0 µM of Cu(II).

Cu(II) as shown in Figure 4.5b, whereby a strong dependence of Cu(II) concentration is apparent. These results indicate that there is a strong interaction between Cu(II) and curcumin in acetonitrile, in contrast to that between curcumin and Cu(I). Therefore, the formation of the complex is strongly dependent on the oxidation state of copper.

We next investigated curcumin stability upon reduction of Cu(II) to Cu(I) using ascorbic acid. This study was conducted in aqueous solution on curcumin in SDS micelles in which curcumin exhibits a high stability [27, 38], as does the Cu(II)−Curcumin complex. In the presence of 1 mM ascorbic acid, however, the UV-visible absorption spectrum of the Cu(II)−Curcumin complex decreases in intensity with time, consistent with curcumin decomposition as shown in Figure 4.6. This result coincides with the reduction of Cu(II) to Cu(I) by ascorbic acid [39], which has been shown to induce generation of free radicals, including hydroxyl radicals [40, 41]. It is likely that these reactive free radicals undergo irreversible reactions with curcumin, resulting in decomposition.

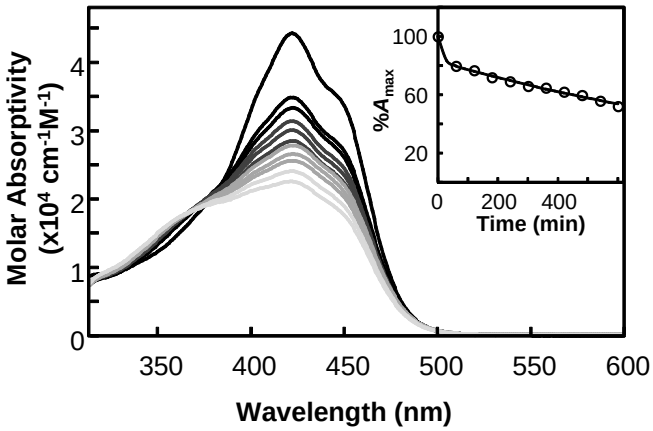

Figure 4.6. UV-visible absorption spectra of 10 µM curcumin in the SDS micellar solution in the presence of 20 µM Cu(II) and 1 mM ascorbic acid over 10 h. The inset shows the decrease of the absorption maxima as a function of time.

The anticancer properties of curcumin are thought to arise from its ability to cause DNA damage in cancer cells [18–21]. Recently, the reduction of Cu(II) to Cu(I) has been proposed to play a role in the DNA damaging ability of curcumin [22]. The suggested mechanism involves a simultaneous oxidation of curcumin and a conversion of molecular oxygen to superoxide, which then form hydrogen peroxide to cause DNA damage [22]. A second proposed mechanism involves a copper mediated decomposition of curcumin to form various metabolites [1]. The resulting metabolites are, therefore, responsible for the anticancer properties of curcumin.

Mass spectrometry and HPLC were used to provide insight into the presence of metabolites as a result of curcumin decomposition due to reduction of Cu(II) to Cu(I). The experiment details for time-dependent mass spectrometry and HPLC on the Cu(II)–Curcumin complex in acetonitrile are presented in Appendix A. Results from time-dependent mass spectrometry and HPLC further support the decomposition of curcumin as a consequence of reduction of Cu(II) to Cu(I) (Appendix A).

4.5 Conclusions

In this study, we show that the decomposition of curcumin in the presence of Cu(II) in acetonitrile is directly due to the reduction of Cu(II) to Cu(I). Evidence for the formation of the Cu(II)−Curcumin complex in acetonitrile is adduced from a substantial blue shift of the curcumin UV-visible absorption maximum from 420 nm to 350 nm at a Cu(II):Curcumin molar ratio of 10:1. This blue shift is attributed to conversion from the curcumin keto-enol tautomer in the free state to the diketo tautomer in the Cu(II) complexed state. This absorbance decreases as a function of time due to decomposition of curcumin following oxidation to curcumin radical accompanying the reduction of Cu(II) to Cu(I). Data from time-dependent mass spectrometry and high performance liquid chromatography further support the decomposition of curcumin respectively, as a consequence of reduction of Cu(II) to Cu(I).

4.6 References

(1) Anand, P.; Thomas, S. G.; Kunnumakkara, A. B.; Sundaram, C.; Harikumar, K. B.; Sung, B.; Tharakan, S. T.; Misra, K.; Priyadarsini, I. K.; Rajasekharan, K. N.; Aggarwal, B. B. Biological Activities of Curcumin and Its Analogues (Congeners) Made by Man and Mother Nature. *Biochem. Pharmacol.* **2008**, *76*, 1590–1611.

(2) Payton, F.; Sandusky, P.; Alworth, W. L. NMR Study of the Solution Structure of Curcumin. *J. Nat. Prod.* **2007**, *70*, 143–146.

(3) Lao, C. D.; Ruffin, M. T. t.; Normolle, D.; Heath, D. D.; Murray, S. I.; Bailey, J. M.; Boggs, M. E.; Crowell, J.; Rock, C. L.; Brenner, D. E. Dose Escalation of a Curcuminoid Formulation. *BMC Complem. Altern. M.* **2006**, *6*, 10.

(4) Marín, Y. E.; Wall, B. A.; Wang, S.; Namkoong, J.; Martino, J. J.; Suh, J.; Lee, H. J.; Rabson, A. B.; Yang, C. S.; Chen, S.; Ryu, J.-H. Curcumin Down-regulates the Constitutive Activity of Nf-κb and Induces Apoptosis in Novel Mouse Melanoma Cells. *Melanoma Res.* **2007**, *17*, 274–283.

(5) Odot, J.; Albert, P.; Carlier, A.; Tarpin, M.; Devy, J.; Madoulet, C. *In Vitro* and *in Vivo* Anti-Tumoral Effect of Curcumin against Melanoma Cells. *Int. J. Cancer* **2004**, *111*, 381–387.

(6) Siwak, D. R.; Shishodia, S.; Aggarwal, B. B.; Kurzrock, R. Curcumin-Induced Antiproliferative and Proapoptotic Effects in Melanoma Cells are Associated with Suppression of IκB Kinase and Nuclear Factor κB Activity and are Independent of the B-Raf/Mitogen-Activated/Extracellular Signal-Regulated Protein Kinase Pathway and the Akt Pathway. *Cancer* **2005**, *104*, 879–890.

(7) Lantz, R. C.; Chen, G. J.; Solyom, A. M.; Jolad, S. D.; Timmermann, B. N. The Effect of Turmeric Extracts on Inflammatory Mediator Production. *Phytomedicine* **2005**, *12*, 445–452.

(8) Ruby, A.; Kuttan, G.; Babu, K. D.; Rajasekharan, K.; Kuttan, R. Anti-Tumour and Antioxidant Activity of Natural Curcuminoids. *Cancer Lett.* **1995**, *94*, 79–83.

(9) Zheng, M.; Ekmekcioglu, S.; Walch, E. T.; Tang, C.-H.; Grimm, E. A. Inhibition of Nuclear Factor-κB and Nitric Oxide by Curcumin Induces G_2/M Cell Cycle Arrest and Apoptosis in Human Melanoma Cells. *Melanoma Res.* **2004**, *14*, 165–171.

(10) Aggarwal, B. B.; Kumar, A.; Bharti, A. C. Anticancer Potential of Curcumin: Preclinical and Clinical Studies. *Anticancer Res.* **2003**, *23*, 363–398.

(11) Yang, F. S.; Lim, G. P.; Begum, A. N.; Ubeda, O. J.; Simmons, M. R.; Ambegaokar, S. S.; Chen, P. P.; Kayed, R.; Glabe, C. G.; Frautschy, S. A.; Cole, G. M. Curcumin Inhibits Formation of Amyloid β Oligomers and Fibrils, Binds Plaques, and Reduces Amyloid *in Vivo*. *J. Biol. Chem.* **2005**, *280*, 5892–5901.

(12) Egan, M. E.; Pearson, M.; Weiner, S. A.; Rajendran, V.; Rubin, D.; Glockner-Pagel, J.; Canny, S.; Du, K.; Lukacs, G. L.; Caplan, M. J. Curcumin, a Major Constituent of Turmeric, Corrects Cystic Fibrosis Defects. *Science* **2004**, *304*, 600–602.

(13) Chan, W.-H.; Wu, H.-J. Anti-Apoptotic Effects of Curcumin on Photosensitized Human Epidermal Carcinoma A431 Cells. *J. Cell. Biochem.* **2004**, *92*, 200–212.

(14) Koon, H. K.; Leung, A. W. N.; Yue, K. K. M.; Mak, N. K. Photodynamic Effect of Curcumin on NPC/CNE2 Cells. *J. Environ. Pathol. Toxicol. Oncol.* **2006**, *25*, 205–216.

(15) Park, K.; Lee, J.-H. Photosensitizer Effect of Curcumin on UVB-Irradiated HaCaT Cells through Activation of Caspase Pathways. *Oncol. Rep.* **2007**, *17*, 537–540.

(16) ClinicalTrials.gov: Trial of Curcumin in Advanced Pancreatic Cancer., `http://clinicaltrials.gov/ct2/show/NCT00094445`.

(17) ClinicalTrials.gov: Curcumin in Patients With Mild to Moderate Alzheimer's Disease., `http://clinicaltrials.gov/ct2/show/NCT00099710`.

(18) Yoshino, M.; Haneda, M.; Naruse, M.; Htay, H. H.; Tsubouchi, R.; Qiao, S. L.; Li, W. H.; Murakami, K.; Yokochi, T. Prooxidant Activity of Curcumin: Copper-Dependent Formation of 8-Hydroxy-2-Deoxyguanosine in DNA and Induction of Apoptotic Cell Death. *Toxicol. in Vitro* **2004**, *18*, 783–789.

(19) Ahsan, H.; Hadi, S. M. Strand Scission in DNA Induced by Curcumin in the Presence of Cu(II). *Cancer Lett.* **1998**, *124*, 23–30.

(20) Ahsan, H.; Parveen, N.; Khan, N. U.; Hadi, S. M. Pro-Oxidant, Anti-Oxidant and Cleavage Activities on DNA of Curcumin and Its Derivatives Demethoxycurcumin and Bisdemethoxycurcumin. *Chem. Biol. Interact.* **1999**, *121*, 161–175.

(21) Lou, J. R.; Zhang, X.-X.; Zheng, J.; Ding, W.-Q. Transient Metals Enhance Cytotoxicity of Curcumin: Potential Involvement of the NFκB and mTOR Signaling Pathways. *Anticancer Res.* **2010**, *30*, 3249–3255.

(22) Sakano, K.; Kawanishi, S. Metal-Mediated DNA Damage Induced by Curcumin in the Presence of Human Cytochrome P450 Isozymes. *Arch. Biochem. Biophys.* **2002**, *405*, 223–230.

(23) Deng, S.-L.; Chen, W.-F.; Zhou, B.; Yang, L.; Liu, Z.-L. Protective Effects of Curcumin and Its Analogues against Free Radical-Induced Oxidative Haemolysis of Human Red Blood Cells. *Food Chem.* **2006**, *98*, 112–119.

(24) Chen, W.-F.; Deng, S.-L.; Zhou, B.; Yang, L.; Liu, Z.-L. Curcumin and Its Analogues as Potent Inhibitors of Low Density Lipoprotein Oxidation: H-Atom Abstraction from the Phenolic Groups and Possible Involvement of the 4-Hydroxy-3-Methoxyphenyl Groups. *Free Radic. Biol. Med.* **2006**, *40*, 526–535.

(25) Barik, A.; Mishra, B.; Shen, L.; Mohan, H.; Kadam, R. M.; Dutta, S.; Zhang, H. Y.; Priyadarsini, K. I. Evaluation of a New Copper(II)-Curcumin Complex as Superoxide Dismutase Mimic and Its Free Radical Reactions. *Free Radic. Biol. Med.* **2005**, *39*, 811–822.

(26) Yoshida, D.; Ikeda, Y.; Nakazawa, S. Quantitative Analysis of Copper, Zinc and Copper/Zinc Ratio in Selected Human Brain Tumors. *J. Neurooncol.* **1993**, *16*, 109–115.

(27) Leung, M. H. M.; Pham, D.-T.; Lincoln, S. F.; Kee, T. W. Femtosecond Transient Absorption Spectroscopy of Copper(II))-Curcumin Complexes. *Phys. Chem. Chem. Phys.* **2012**, *14*, 13580–13587.

(28) Girolami, G. S.; Jeffries, P. M.; Dubois, L. H. Mechanistic Studies of Copper Thin-Film Growth from Cu(I) and Cu(II) β-Diketonates. *J. Am. Chem. Soc.* **1993**, *115*, 1015–1024.

(29) Shin, H. K.; Chi, K. M.; Farkas, J.; Hampden-Smith, M. J.; Kodas, T. T.; Duesler, E. N. Chemistry of Copper(I) β-Diketonate Complexes. 2. Synthesis, Characterization, and Physical Properties of (β-Diketonato)Copper(I) Trimethylphosphine and Bis(Trimethylphosphine) Complexes. *Inorg. Chem.* **1992**, *31*, 424–431.

(30) Addicoat, M. A.; Metha, G. F.; Kee, T. W. Density Functional Theory Investigation of Cu(I)- and Cu(II)-Curcumin Complexes. *J. Comput. Chem.* **2011**, *32*, 429–438.

(31) Chignell, C. F.; Bilskj, P.; Reszka, K. J.; Motten, A. G.; Sik, R. H.; Dahl, T. A. Spectral and Photochemical Properties of Curcumin. *Photochem. Photobiol.* **1994**, *59*, 295–302.

(32) Harada, T.; Pham, D.-T.; Leung, M. H. M.; Ngo, H. T.; Lincoln, S. F.; Easton, C. J.; Kee, T. W. Cooperative Binding and Stabilization of the Medicinal Pigment Curcumin by Diamide Linked γ-Cyclodextrin Dimers: A Spectroscopic Characterization. *J. Phys. Chem. B* **2011**, *115*, 1268–1274.

(33) Leung, M. H. M.; Kee, T. W. Effective Stabilization of Curcumin by Association to Plasma Proteins: Human Serum Albumin and Fibrinogen. *Langmuir* **2009**, *25*, 5773–5777.

(34) Kamau, P.; Jordan, R. B. Complex Formation Constants for the Aqueous Copper(I)-Acetonitrile System by a Simple General Method. *Inorg. Chem.* **2001**, *40*, 3879–3883.

(35) Kolthoff, I. M.; Coetzee, J. F. Polarography in Acetonitrile. 2. Metal Ions which have Significantly Different Polarographic Properties in Acetonitrile and in Water-Anodic Waves-Voltammetry at Rotated Platinum Electrode. *J. Am. Chem. Soc.* **1957**, *79*, 1852–1858.

(36) Bong, P.-H. Spectral and Photophysical Behaviors of Curcumin and Curcuminoids. *Bull. Korean Chem. Soc.* **2000**, *21*, 81–86.

(37) Leung, M. H. M.; Colangelo, H.; Kee, T. W. Encapsulation of Curcumin in Cationic Micelles Suppresses Alkaline Hydrolysis. *Langmuir* **2008**, *24*, 5672–5675.

(38) Tønnesen, H. H.; Másson, M.; Loftsson, T. Studies of Curcumin and Curcuminoids. XXVII. Cyclodextrin Complexation: Solubility, Chemical and Photochemical Stability. *Int. J. Pharm.* **2002**, *244*, 127–135.

(39) Beers, M. F.; Johnson, R. G.; Scarpa, A. Evidence for an Ascorbate Shuttle for the Transfer of Reducing Equivalents across Chromaffin Granule Membranes. *J. Biol. Chem.* **1986**, *261*, 2529–2535.

(40) Ueda, J.-i.; Takai, M.; Shimazu, Y.; Ozawa, T. Reactive Oxygen Species Generated from the Reaction of Copper(II) Complexes with Biological Reductants Cause DNA Strand Scission. *Arch. Biochem. Biophys.* **1998**, *357*, 231–239.

(41) Yoshino, M.; Haneda, M.; Naruse, M.; Murakami, K. Prooxidant Activity of Flavonoids: Copper-Dependent Strand Breaks and the Formation of 8-Hydroxy-2'-Deoxy-guanosine in DNA. *Mol. Genet. Metab.* **1999**, *68*, 468–472.

CHAPTER 5

KETO-ENOL TAUTOMERISATION OF THE MEDICINAL PIGMENT CURCUMIN

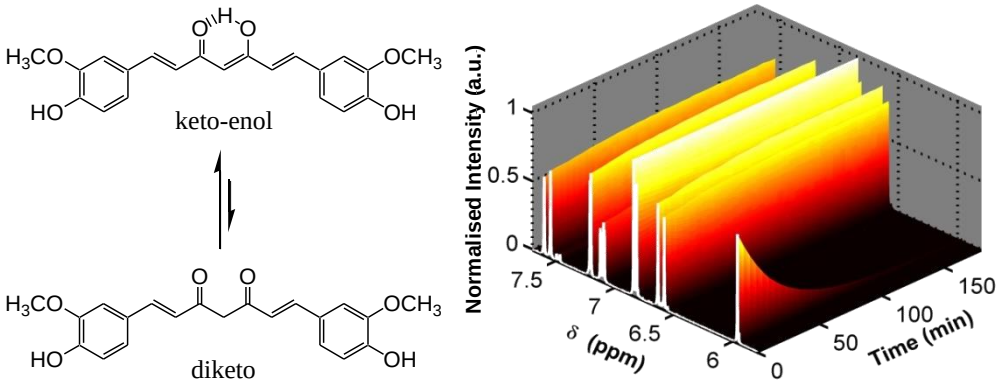

5.1 Abstract

Curcumin is a medicinal agent that exhibits anti-cancer and anti-Alzheimer's disease properties. It has a keto-enol moiety that gives rise to many of its chemical properties including metal complexation and acid-base equilibria. A recent study has shown that keto-enol tautomerisation at this moiety is implicated in the anti-Alzheimer's disease effect of curcumin, highlighting the importance of this reaction. In this study, tautomerisation of curcumin in methanol, acetone and acetonitrile is investigated using ^{1}H nuclear magnetic resonance (NMR) spectroscopy. Curcumin undergoes hydrogen-deuterium exchange with the solvents and the proton resonance peak corresponding to the hydrogen at the α-carbon position (C_α) decays as a function of time, signifying deuteration at this position. Furthermore, the rate of tautomerisation is inferred from the rate of deuteration at the C_α position because tautomerisation is the rate limiting step in the deuteration. The rate constant of tautomerisation of curcumin shows a strong temperature dependence. Analysis of the temperature dependent rate constants using the Arrhenius equation reveals that the activation energies (E_a) of tautomerisation are 80.1 ± 5.9, 64.1 ± 1.0 and 68.3 ± 5.5 kJ mol^{-1} in methanol, D_2O/acetone and D_2O/acetonitrile, respectively. The difference in the E_a is attributable to the presence of D_2O, which exhibits a catalytic effect on the tautomerisation of curcumin. The results of this study represent an important step toward understanding the effect of tautomerisation of curcumin in its medicinal effects.

5.2 Introduction

β-Diketones have always been of interest to chemists because they are common reactants in many synthetic reactions. For instance, a 1,4-addition of a nucleophile to a β-diketone is involved in the Michael reaction [1–3]. Furthermore, β-diketones are important bidentate ligands in coordination chemistry. The two oxygen atoms enable a strong binding to transition metal and lanthanide ions [4–7]. In addition, the keto-enol $\rightleftharpoons$ diketo equilibrium of β-diketones is a fundamental reaction in chemistry, which has been studied extensively for decades [7–11].

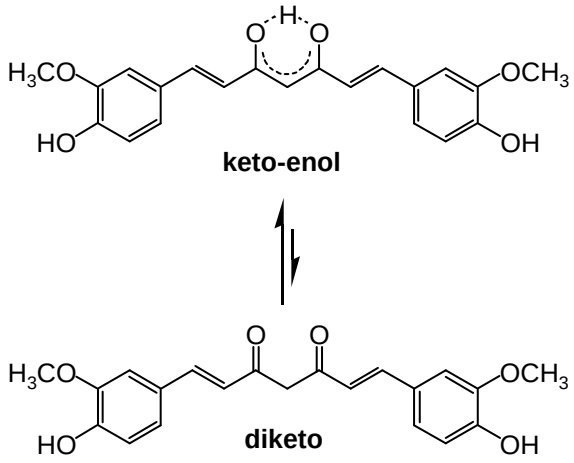

Figure 5.1. Structure of the keto-enol and diketo tautomers of curcumin.

Curcumin is a β-diketone found in the rhizomes of turmeric, which is a common spice plant in many parts of Asia. Curcumin has been under intense investigation because of its biological activities [12–20]. Curcumin exhibits medicinal effects against cystic fibrosis [12, 13], cancer cell proliferation [14, 15] and amyloid β fibril formation [16–18]. Interestingly, curcumin inhibits the formation of amyloid β fibrils by binding with small amyloid β species [17]. Recent research suggested that tautomerisation of curcumin, as illustrated in Figure 5.1, is important to its effectiveness against amyloid fibril formation [18]. Yanagisawa et al. showed that the curcumin derivatives that lack the ability to tautomerise exhibit a weaker interaction with the amyloid β aggregates than the native form of curcumin [18]. The key difference between the two tautomers is the hybridisation of the carbon at the α position (C_α). While sp^2 hybridisation is present in the keto-enol tautomer, the diketo tautomer has sp^3 hybridisation

(Figure 5.1). Additionally, there is intramolecular hydrogen bonding in the keto-enol tautomer, which is absent in the diketo tautomer of curcumin [7, 10, 21–24]. It has been shown that the strength of the hydrogen bond at the keto-enol moiety is strongly correlated to the delocalisation of π-electrons in β-diketones [23]. The delocalisation of π-electrons is further supported by the red-shifted UV-visible absorption maximum of the keto-enol tautomer of curcumin (λ_{max} = 430 nm) compared with that of the diketo tautomer. It has been shown that the diketo form of curcumin has a similar absorption maximum as *trans*-6-(4'-hydroxy-3'-methoxy-phenyl)-2,4-dioxo-5-hexenal, or *half*-curcumin, (λ_{max} = 340 nm) owing to their similar conjugation lengths [25]. Furthermore, recent studies have shown that the presence of intramolecular hydrogen bonding is important in the dynamics of photo-excited curcumin [21, 22].

Tautomerisation of β-diketones has been under investigation for decades. Using different experimental techniques, the thermodynamic and kinetic properties of these species were elucidated [11, 26–31]. NMR spectroscopy has been an important technique for studying the tautomerisation equilibria of β-diketones by determining the relative proportions of the keto-enol and diketo tautomers in various solvents [11, 28, 29, 31]. Studies have shown that tautomerisation of β-diketones exhibits a strong dependence on the surrounding environment [7–9, 30–32]. In particular, a decrease in the relative proportion of the keto-enol tautomer of acetylacetone and dibenzoylmethane is correlated to an increase in solvent polarity [7, 9]. Interestingly, curcumin appears to be an exception to this trend according to a NMR study by Payton et al. [33] These authors showed that the keto-enol tautomer is the dominant form of curcumin in a variety of solvents from a non-polar organic solvent to mixtures of water and dimethylsulphoxide [33]. In addition to the thermodynamic equilibria, NMR spectroscopy has been used to study the kinetics of the tautomerisation of β-diketones. It has been shown that β-diketones undergo hydrogen-deuterium exchange (H/D exchange) with the deuterated analogues of protic solvents, and the rate of which can be measured using ^{1}H NMR spectroscopy [11]. First, the hydroxyl group in the keto-enol moiety of β-diketones undergoes a rapid H/D exchange with the deuterated protic solvent. Subsequently, the hydrogen at the C_α position becomes deuterated at a slower rate than the initial H/D exchange owing to tautomerisation between the keto-enol and diketo structures. The deuteration of the C_α of acetylacetone and ethylacetoacetate has been demonstrated in

a previous study, in which a complete deuteration of these β-diketones was observed due to a high concentration of deuterium from the solvent [11]. In this case, the kinetics of tautomerisation of β-diketones is then inferred from the deuteration at the C_α position because tautomerisation is the rate limiting step in the deuteration process.

In this study, the rate constants of the tautomerisation of curcumin in methanol, acetone and acetonitrile are determined at several temperatures. The temperature dependence of the rate constants is analysed using the Arrhenius equation and the results reveal the activation energy (E_a) of keto-enol to diketo tautomerisation of curcumin for the first time. The E_a values range from 64 – 80 kJ mol^{-1} in these solvents. Furthermore, the difference in the E_a value is attributable to the presence of D_2O, which exhibits a catalytic effect on tautomerisation of curcumin.

5.3 Materials and Methods

5.3.1 Materials

Curcumin (purity $> 98\,\%$) was purchased from LKT Laboratories. Acetone-d_6 (D, 99.9 %) and D_2O (D, 99.9 %) were purchased from Cambridge Isotope Laboratories; methanol-d_4 (D, 99.8 %) and acetonitrile-d_3 (D, 99.8 %) were obtained from Sigma-Aldrich. All materials were used as received.

5.3.2 ^{1}H NMR Spectroscopy

The ^{1}H NMR spectra of curcumin were recorded at temperatures ranging from 25 – 45 °C using a Varian Gemini-2000 NMR spectrometer equipped with variable temperature accessory operating at 300.145 MHz. For measurements with curcumin in methanol-d_4, a volume of 700-µL of methanol-d_4 was equilibrated at the target temperature for 15 min before use, which was followed by dissolving curcumin to yield a 10.9 mM solution. The acquisition of the ^{1}H NMR spectrum was started immediately after the addition of curcumin at 5-min intervals for 3 h. The molar ratio of CD_3OD to curcumin was 2268:1. For measurements with curcumin in acetone-d_6 or acetonitrile-d_3, a 700 µL of 10.9 mM curcumin solution was prepared under nitrogen and then equilibrated at the target temperature for 15 min. A volume of 31-µL of D_2O was added to the thermally equilibrated curcumin solution, which was immediately followed by the NMR spectra acquisition at 5-min intervals for 3 h. The molar ratio of D_2O to curcumin was approximately 227:1. The content of D_2O in acetone-d_6 or acetonitrile-d_3 was approximately 5.6 weight% or 4.4 volume%. All experiments were done in triplicates.

5.3.3 Data Analysis

Chemical shifts (δ) of the collected NMR spectra were referenced to the residue proton resonance of the corresponding deuterated solvents, which are δ = 3.31, 2.05 and 1.94 ppm for the pentet proton signal of the methyl group in methanol-d_4, acetone-d_6 and acetonitrile-d_3, respectively. Assignments of the ^{1}H NMR spectra of curcumin

in methanol-d_4, D_2O/acetone-d_6 and D_2O/acetonitrile-d_3 are shown in Figure 5.2. The area under the resonance peak of H_α was calculated and normalised to the sum of areas under the resonance peaks of H_{1-6}. The rate constant at a given temperature was determined by fitting the normalised area of the H_α peak as a function of time using the rate equations, shown in the following:

$$\frac{d[\mathbf{A}]}{dt} = -k_1[\mathbf{A}][CD_3OD] + k_{-1}[\mathbf{B}][CD_3OH]$$

$$\frac{d[\mathbf{B}]}{dt} = k_1[\mathbf{A}][CD_3OD] - k_{-1}[\mathbf{B}][CD_3OH] - k_2[\mathbf{B}] + k_{-2}[\mathbf{C}]$$

$$\frac{d[\mathbf{C}]}{dt} = k_2[\mathbf{B}] - k_{-2}[\mathbf{C}] - k_3[\mathbf{C}] + k_{-3}[\mathbf{D}]$$

$$\frac{d[\mathbf{D}]}{dt} = k_3[\mathbf{C}] - k_{-3}[\mathbf{D}] - k_4[\mathbf{D}][CD_3OD] + k_{-4}[\mathbf{E}][CD_3OH]$$

$$\frac{d[\mathbf{E}]}{dt} = k_4[\mathbf{D}][CD_3OD] - k_{-4}[\mathbf{E}][CD_3OH]$$

where [**A**], [**B**], [**C**], [**D**] and [**E**] denote the concentration of curcumin in different stages of deuteration (Scheme 5.1). $[CD_3OD]$ and $[CD_3OH]$ are the concentrations of methanol-d_4 and methanol-d_3, respectively. Methanol-d_4 undergoes H/D exchange with the hydroxyl group in the keto-enol moiety of curcumin to yield methanol-d_3. These equations were derived from our proposed reaction scheme, as shown in the following section. These coupled differential equations were solved numerically using a MATLAB script, as shown in Appendix B. Finally, the E_a of the tautomerisation of curcumin was determined by fitting the rate constants as a function of temperature using the Arrhenius equation.

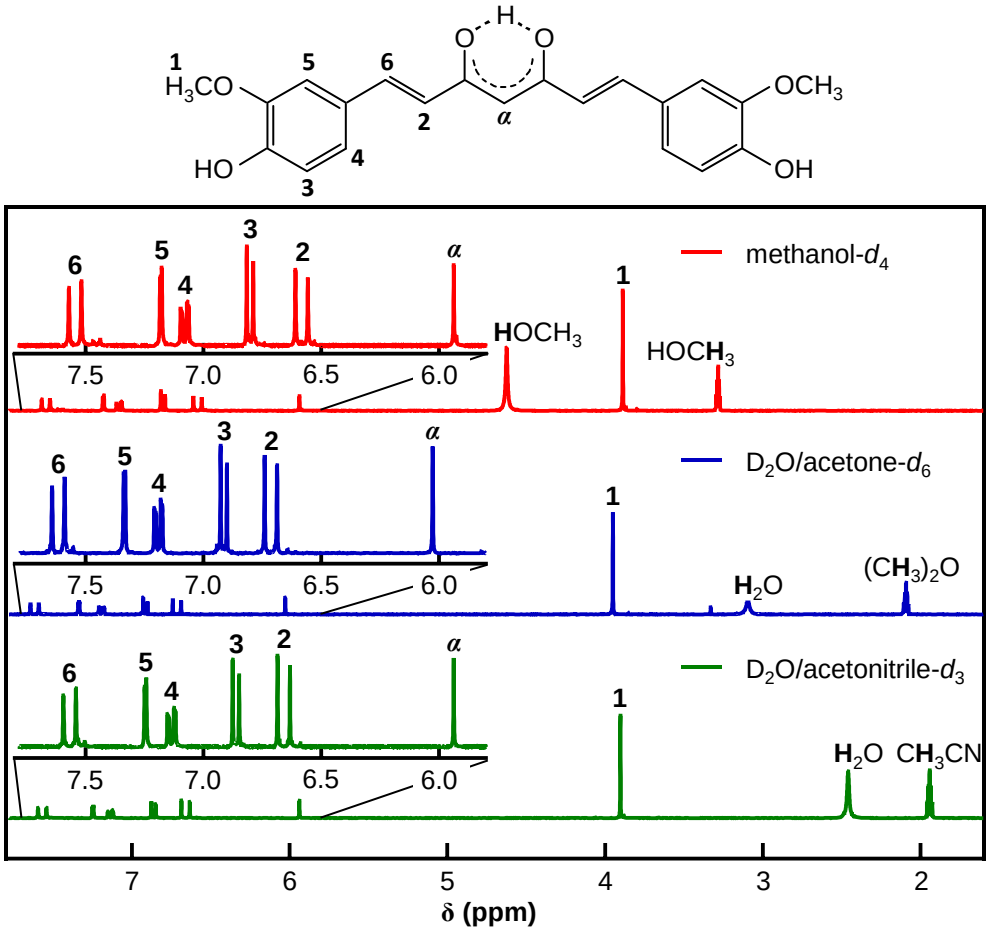

Figure 5.2. Structure of keto-enol curcumin with hydrogens labeled as α and 1-6, and its NMR spectra in methanol-d_4 (top), D_2O/acetone-d_6 (middle) and D_2O/acetonitrile-d_3 (bottom).

5.4 Results and Discussion

5.4.1 Deuteration of Curcumin at C_α

Curcumin exists as the keto-enol tautomer (Figure 5.1) in most polar organic solvents [33]. The enolic hydrogen in the keto-enol moiety forms an intramolecular hydrogen-bond with the oxygen of the carbonyl group (Figure 5.1). It has been suggested that the delocalisation of the π-electrons in the conjugated backbone assists the intramolecular hydrogen-bond formation [23, 34]. As mentioned previously, curcumin undergoes H/D exchange at the C_α position owing to tautomerisation. A reaction scheme for the H/D exchange in methanol-d_4 is shown in Scheme 5.1. The reactants are CD_3OD and the keto-enol tautomer curcumin, **A**. The H/D exchange equilibrium of the enolic hydrogen in the keto-enol moiety of curcumin is shown in the first line of Scheme 5.1. This H/D exchange yielding curcumin **B** is expected to be largely irreversible due to an excess of deuterium from CD_3OD [11]. It is known that the enolic

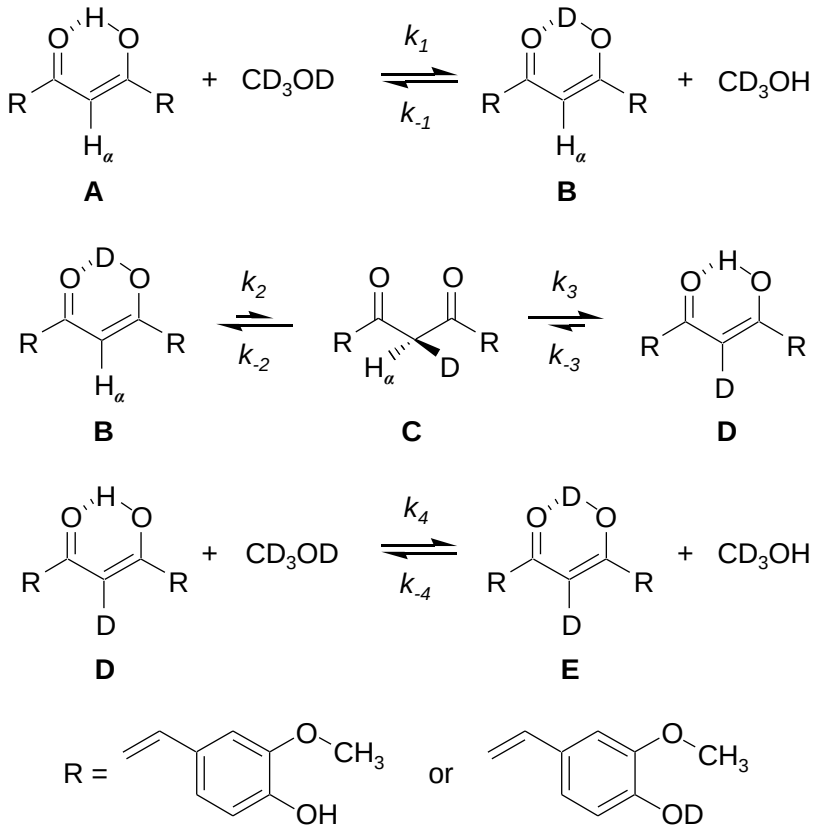

Scheme 5.1. Deuteration of curcumin in methanol-d_4.

hydrogen in the keto-enol moiety of curcumin is acidic and its pKa value has been reported previously [35, 36]. The relatively low pKa value of 8.3 compared with that of the phenol hydrogen of curcumin indicates that this hydrogen can be dissociated at a slightly alkaline environment to produce a negatively charged enolate ion [35, 36]. The enolate ion of curcumin is then able to react with deuterium, resulting in the deuteration of the hydroxyl group in the keto-enol moiety of curcumin. The tautomerisation of curcumin (Figure 5.1) is shown as **B** $\rightleftharpoons$ **C** $\rightleftharpoons$ **D** in Scheme 5.1. As the keto-enol tautomer of curcumin is the dominant form in methanol-d_4 [33], the tautomerisation equilibrium of curcumin is expected to shift towards curcumin **B** and **D**, where curcumin **B** has a H_α and curcumin **D** has a deuterium at the C_α position. Therefore, the rate constants of enolisation (from the diketo curcumin **C** to either keto-enol curcumin **B** or **D**), k_{-2} and k_3, are expected to be significantly larger than the rate constants of the reverse reaction, k_2 and k_{-3}. The difference in the rate constants is illustrated by the arrow size in Scheme 5.1. Consequently, we argue that the rate of deuteration at the C_α position of curcumin reflects the rate of keto-enol to diketo tautomerisation because the tautomerisation reaction, *i.e.*, the step involving k_2, is the rate limiting step for the H/D exchange of curcumin.

The keto-enol to diketo tautomerisation of curcumin was also investigated in acetone-d_6 and acetonitrile-d_3. Acetone-d_6 and acetonitrile-d_3 are aprotic solvents, and they are unable to undergo H/D exchange with curcumin. Therefore, a small quantity of D_2O was added to enable deuteration of curcumin to occur in these solvents. The quantity of D_2O was kept at approximately 5.6 weight% or 4.4 volume% to minimise the influence of D_2O in the properties of these solvents. A higher D_2O content would lead to significant water-induced decomposition of curcumin [37]. In consistence with our argument above, the rate of deuteration at the C_α position of curcumin in acetone-d_6 and acetonitrile-d_3 reflects the rate of keto-enol to diketo tautomerisation.

Recent work by Nichols and Waner has shown that the exchange of H_α with deuterium in β-diketones, including acetylacetone and ethyl acetoacetate, can be investigated using ^{1}H NMR spectroscopy [11]. In our study, the relative concentration of curcumin **B** is determined by the intensity of the resonance peak of H_α. The intensity of the H_α peak decreases as a function of time owing to the H/D exchange as a consequence of the tautomerisation of curcumin **B** to form **C**. Additionally, the H/D

exchange of the enolic hydrogen in the keto-enol moiety of curcumin **D** (**D** $\rightleftharpoons$ **E**) is expected to be same as **A** $\rightleftharpoons$ **B**. The molar ratio of CD_3OD to curcumin is 2268:1 and D_2O (in acetone and acetonitrile) is 227:1. These high molar ratios facilitate deuteration of the hydroxyl groups in the keto-enol moiety to form curcumin **B** and **E**.

Figure 5.3 shows the time-dependent ^1H NMR spectra of curcumin in methanol-d_4, D_2O/acetone-d_6 and D_2O/acetonitrile-d_3 from δ = 7.5 to 5.5 ppm recorded at 45 °C. It is clear that the intensity of the H_α peak, which has a δ of approximately 6 ppm, decreases as a function of time in all three solvents. This time-dependent decrease signifies the deuteration at the C_α position of curcumin as the ^1H NMR active hydrogen is replaced by the inactive deuterium from the solvent. In contrast, the proton resonance of H_{2-6} remain constant over time, indicating the lack of deuterium exchange at these positions. In addition, the NMR peak of H_1 of curcumin, which has a δ of approximately 4 ppm (Figure 5.2), also remains constant over time, in consistence with the behaviour of H_{2-6}.

The deuteration at the C_α position of curcumin is completed within 3 h in methanol-d_4 at 45 °C, as shown in Figure 5.3a. In other words, the H_α signal decreases to the baseline level, indicating that the hydrogen at the C_α position of curcumin has been replaced with deuterium completely. In contrast, the deuteration process is incomplete for curcumin in D_2O/acetone-d_6 and D_2O/acetonitrile-d_3 at 45 °C (Figure 5.3b and Figure 5.3c). There is a 60 % and 30 % decrease in the intensity of the H_α signal of curcumin in D_2O/acetone-d_6 and D_2O/acetonitrile-d_3, respectively. The difference in the level of deuteration at the C_α position of curcumin is attributable to the significantly larger molar ratio of CD_3OD to curcumin than that of D_2O in acetone and acetonitrile, as stated earlier. The higher concentration of available deuterium for H/D exchange from CD_3OD leads to a complete deuteration of curcumin in the equilibria detailed in Scheme 5.1. Therefore, the difference in the molar ratio between the available deuterium and curcumin leads to the significant difference in the level of deuteration in methanol-d_4 and that in D_2O/acetone-d_6 or D_2O/acetonitrile-d_3.

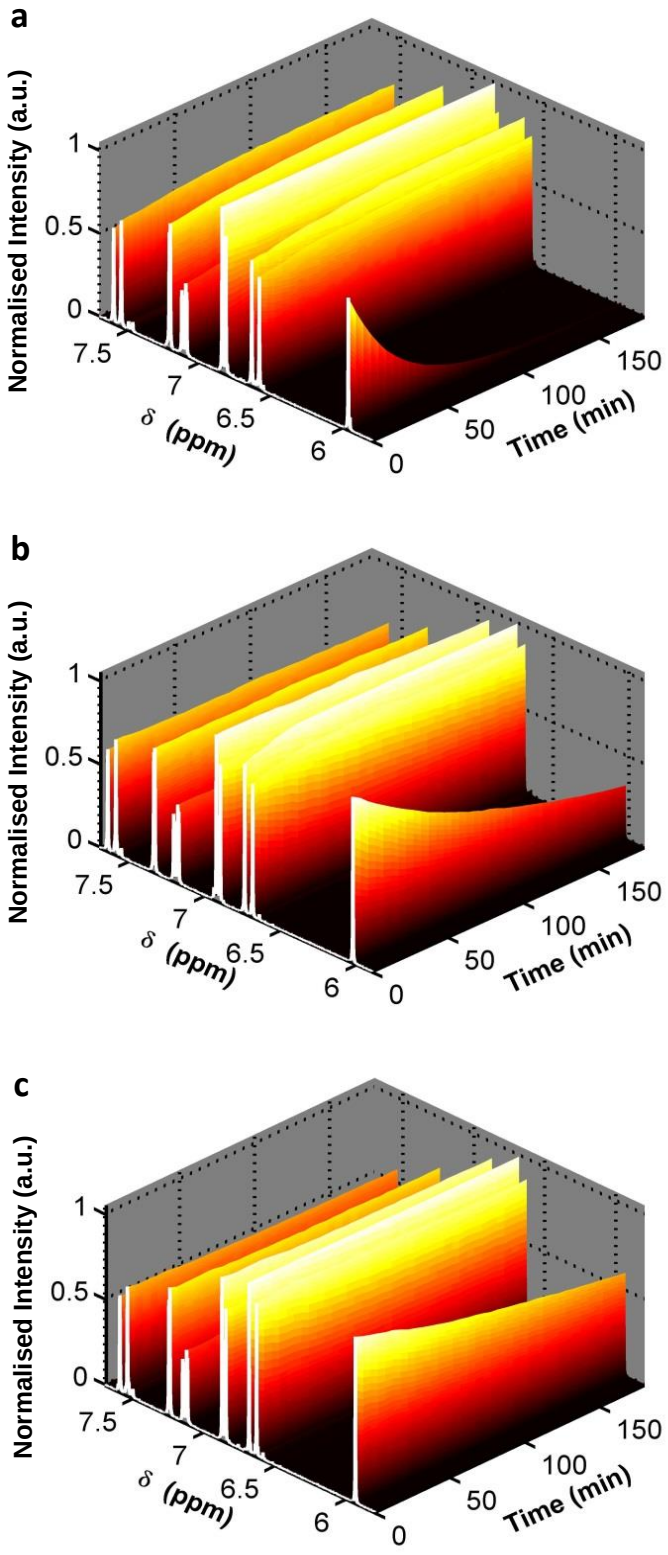

Figure 5.3. ^{1}H NMR spectra from δ = 7.5 to 5.5 ppm of curcumin at 45 °C in (a) methanol-d_4, (b) D_2O/acetone-d_6 and (c) D_2O/acetonitrile-d_3 over time.

5.4.2 From Deuteration to Tautomerisation of Curcumin

The analysis of data using Scheme 1 is as follows. The H/D exchange of the enolic hydrogen of curcumin **A** and **D** with the solvent (the first and last equilibria in Scheme 1) is assumed to occur significantly faster (a factor of 2000) than the keto-enol tautomerisation reaction (the second set of equilibria in Scheme 1) [11], *i.e.*, $k_1/k_2 = 2000$. Furthermore, the H/D exchange of the enolic hydrogen of curcumin is investigated using time-resolved fluorescence upconversion spectroscopy and the results are shown in Figure 5.4. The difference in the decay of the fluorescence upconversion signal is attributable to the deuterium isotope effect on the ESIHT of curcumin, which agrees with previous studies [21, 38]. It is important to note that the well overlapped traces of curcumin in methanol-d_4 indicates that the H/D exchange of the enolic hydrogen is completed as soon as curcumin is dissolved. These results support our assumption on the rate of the H/D exchange of the enolic hydrogen with the solvent being significantly faster than the rate of the tautomerisation of curcumin. In addition, we also assume that $k_1 = k_{-1} = k_4 = k_{-4}$. Furthermore, a previous study has suggested that the concentration ratio of the keto-enol to diketo tautomer is at least 1000:1 [33]. As a result, the ratio of k_{-2} to k_2, which is equal to the equilibrium constant, K, of tautomerisation, is assumed to be 1000 at 25 °C. The values of K at other temperatures (T) are calculated using the relation $\ln K \propto -1/T$ and summarised in Table 5.1. Finally, we also assume that $k_2 = k_{-3}$ and $k_{-2} = k_3$ in the analysis.

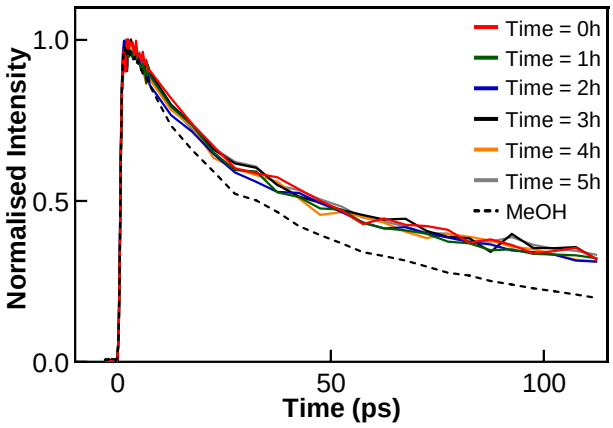

Figure 5.4. Fluorescence upconversion spectra of curcumin in methanol (dashed) and methanol-d_4 (solid) at ambient temperature over 5 hours.

Table 5.1. Rate Constants of Tautomerisation of Curcumin in Methanol-d_4, D_2O/Acetone-d_6 and D_2O/Acetonitrile-d_3 at Several Temperatures

Temperature (K)	K	$k_{\text{methanol-}d_4}$ ($\times 10^{-5}\,s^{-1}$)	$k_{D_2O/\text{acetone-}d_6}$ ($\times 10^{-5}\,s^{-1}$)	$k_{D_2O/\text{acetonitrile-}d_3}$ ($\times 10^{-5}\,s^{-1}$)
298	1000	12.0 ± 1.9	4.0 ± 0.3	1.7 ± 0.3
303	890	20.9 ± 6.0	5.7 ± 0.7	2.6 ± 1.1
308	800	36.4 ± 2.7	11.0 ± 0.7	3.7 ± 0.7
313	720	57.4 ± 3.7	13.2 ± 1.7	7.0 ± 1.1
318	650	90.1 ± 9.9	19.8 ± 1.5	9.0 ± 2.0

Figure 5.5 shows the decrease in the normalised H_α area in methanol-d_4, D_2O/acetone-d_6 and D_2O/acetonitrile-d_3 at several temperatures. As described previously, tautomerisation of curcumin is inferred from deuteration of the H_α of curcumin. The decrease in the intensity of the H_α signal is proportional to the decrease of concentrations of curcumin **A** and **B** as a result of tautomerisation. The rate constant of tautomerisation of curcumin from the keto-enol to diketo structure, k_2, is determined by fitting the decay of the H_α signal with the rate equations detailed in Section 5.3.3. All collected data result in a very good fit with the model used, which are shown as solid curves in Figure 5.5. The rate constants of tautomerisation of curcumin in methanol-d_4, D_2O/acetone-d_6 and D_2O/acetonitrile-d_3 at various temperatures are summarised in Table 5.1.

The rate constants of tautomerisation of curcumin in D_2O/acetone-d_6 are larger than that in D_2O/acetonitrile-d_3 at the same temperature, indicating a fast conversion of keto-enol to diketo tautomer of curcumin in D_2O/acetone-d_6. The difference in the rate constants is attributable to the interactions between curcumin and D_2O in these solvents. Studies have shown that water molecules tend to aggregate in binary mixtures of water/acetonitrile and water/acetone [39–42]. It has been demonstrated that there is significant hydrogen-bonding between water molecules in an acetonitrile-rich environment, which implies the presence of microheterogeneity in D_2O/acetonitrile-d_3 [41]. Furthermore, is has been suggested that at a high acetonitrile mole fraction, the

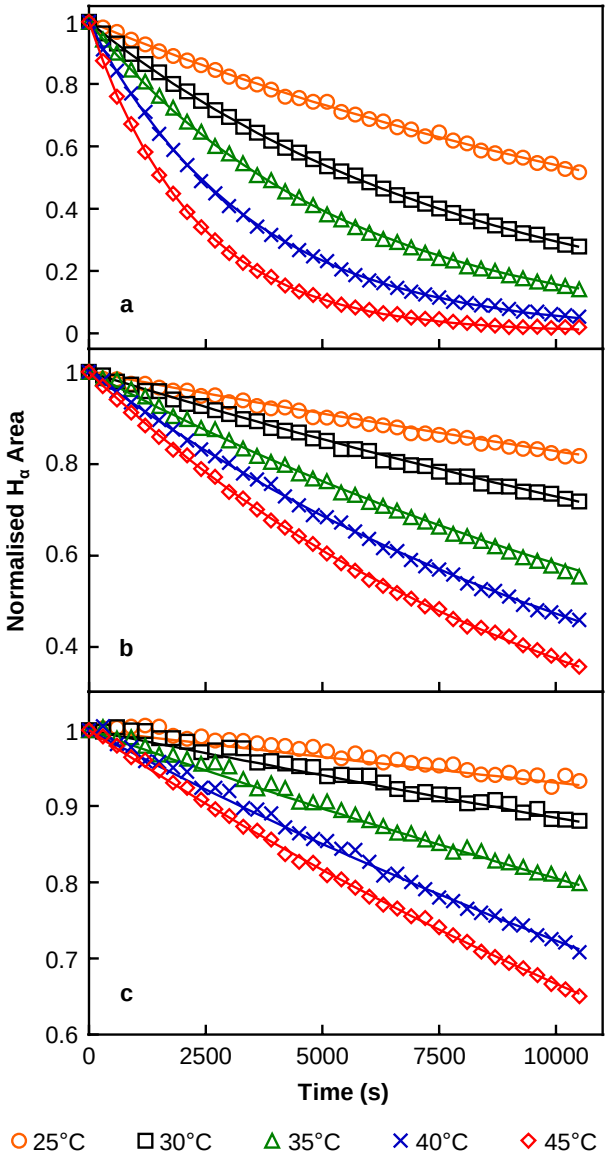

Figure 5.5. The decrease in the normalised H_α signal of curcumin in (a) methanol-d_4, (b) D_2O/acetone-d_6 and (c) D_2O/acetonitrile-d_3 as a function of time at 25 – 45 °C. The solid curves represent the line of best-fit results of the analysis with rate equations.

majority of water molecules form one hydrogen-bond with acetonitrile molecule on the surface of acetonitrile clusters [39]. In the case of water/acetone mixture, however, previous studies suggested that water molecules are isolated at a low water to acetone ratio, such as the one used in this study [41, 42]. In addition, significant bathochromic shifts were observed in the IR signals corresponding to the carbonyl group in acetone and hydroxyl group in water, indicating substantial hydrogen-bonding between acetone and water [42]. Furthermore, Venables and Schmuttenmaer suggested that isolated water molecules form two hydrogen-bonds with two acetone molecules at a low water:acetone ratio [41]. Consequently, D_2O are more dispersed in D_2O/acetone-d_6, which suggests higher probability of successful collisions between curcumin and D_2O than in D_2O/acetonitrile-d_3. The higher rate constants observed in D_2O/acetone-d_6 than those in D_2O/acetonitrile-d_3 are, therefore, attributable to the interactions between curcumin and D_2O.

5.4.3 Activation Energy for Tautomerisation of Curcumin

To determine the activation energy (E_a) barrier of tautomerisation of curcumin, the rate constants of tautomerisation of curcumin at several temperatures are analysed using the Arrhenius Equation. The results are shown in Figure 5.6. The E_a of tautomerisation in methanol-d_4, D_2O/acetone-d_6 and D_2O/acetonitrile-d_3 are calculated from the slope of the best fitted line (Figure 5.6). The E_a of tautomerisation of curcumin are 80.1 ± 5.9, 64.1 ± 1.0 and $68.3 \pm 5.5\,\mathrm{kJ\,mol^{-1}}$ in methanol-d_4, D_2O/acetone-d_6 and D_2O/acetonitrile-d_3, respectively. The higher E_a of tautomerisation of curcumin in methanol-d_4 than those in D_2O/acetone-d_6 and D_2O/acetonitrile-d_3 indicates a larger barrier for tautomerisation of curcumin in methanol-d_4. Furthermore, the E_a of tautomerisation of curcumin in D_2O/acetone-d_6 is likely to be lower than that in D_2O/acetonitrile-d_3. This result is consistent with a stronger interaction between curcumin and D_2O in D_2O/acetone-d_6 than in D_2O/acetonitrile-d_3. This result is independent to the concentration of D_2O as same volume was introduced to both systems. It has been shown that the presence of water molecules stabilises the transition state in the keto-enol tautomerisation [43–46]. Yamabe et al. showed that a catalytic bridge of water molecules disrupted the intramolecular hydrogen bonding in the keto-enol moi-

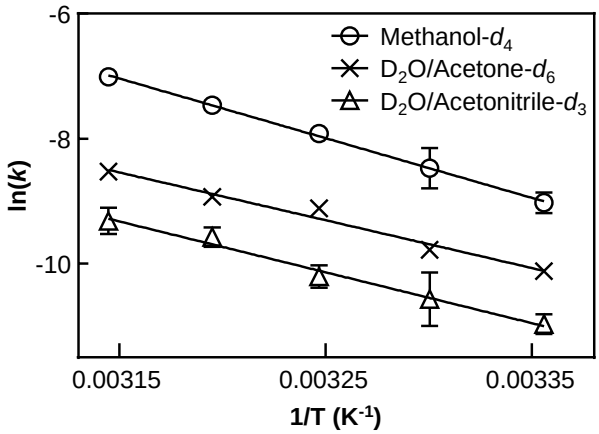

Figure 5.6. Arrhenius plot of the rate constants of tautomerisation of curcumin at 25, 30, 35, 40 and 45 °C in methanol-d_4 (○), D_2O/acetone-d_6 (×) and D_2O/acetonitrile-d_3(△), respectively. The solid lines represent the line of best-fit of the corresponding data.

ety of β-diketones, which results in a substantially lower E_a than that in the absence of water [46]. In other words, water molecules catalyse the tautomerisation reaction by significantly lowering the E_a. Preliminary results from a density functional theory study reveal that the presence of water molecules significantly lowers the energy of the optimised geometry of transition states of tautomerisation of curcumin, as shown in Figure 5.7. Furthermore, a bridge of water molecules arises as the number of water molecules increases from 0 to 3, which agrees with previous study [46]. Therefore, the E_a of the tautomerisation of curcumin in methanol-d_4 is higher than that in D_2O/acetone-d_6 and D_2O/acetonitrile-d_3 because the presence of D_2O lowers the E_a barrier of tautomerisation.

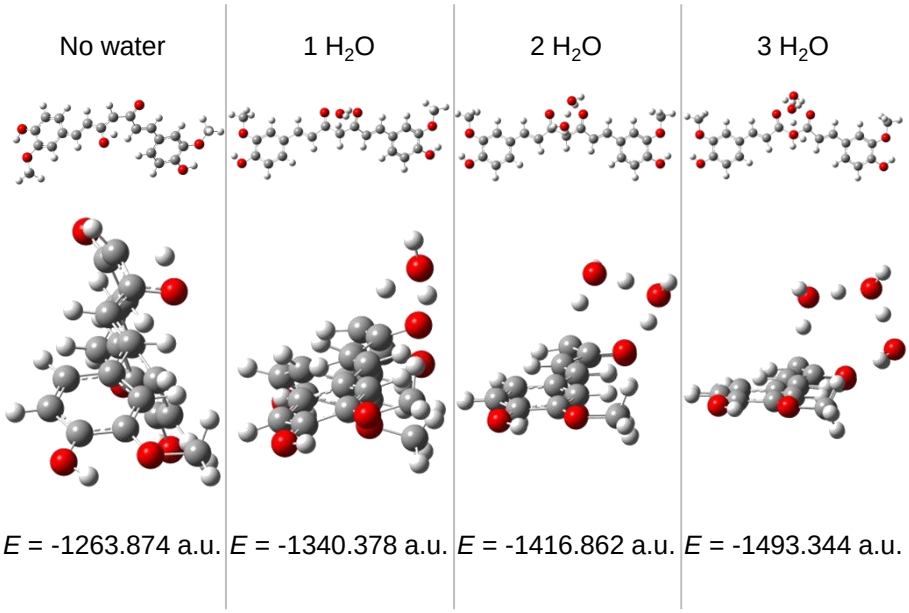

Figure 5.7. DFT optimised geometry of the transition state of tautomerisation of curcumin in the presence of 0 – 3 water molecules.

5.5 Conclusions

In conclusion, the H/D exchange of H_α of curcumin is investigated with ^{1}H NMR in methanol-d_4, D_2O/acetone-d_6 and D_2O/acetonitrile-d_3. Furthermore, the rates of tautomerisation of curcumin, which are inferred from the rates of the H/D exchange of H_α, are determined. There is a strong dependence between the rate constants of tautomerisation of curcumin and temperature. Analysis using the Arrhenius equation reveals that the E_a values of tautomerisation of curcumin are 80.1 ± 5.9, 64.1 ± 1.0 and 68.3 ± 5.5 kJ mol^{-1} in methanol-d_4, D_2O/acetone-d_6 and D_2O/acetonitrile-d_3, respectively. Curcumin has a faster rate of tautomerisation in methanol-d_4 than in D_2O/acetone-d_6 or D_2O/acetonitrile-d_3. The faster rate of tautomerisation observed in methanol-d_4 than that in D_2O/acetone-d_6 or D_2O/acetonitrile-d_3 is due to a higher concentration of deuterium in methanol-d_4. The concentration difference increases the probability of successful collisions significantly and yields a high rate. In addition, the difference between the E_a values for tautomerisation of curcumin in methanol-d_4 and those in D_2O/acetone-d_6 or D_2O/acetonitrile-d_3 is attributable to the presence of D_2O, which exhibits catalytic effect to yield a lower E_a.

5.6 References

(1) Rong, Z.-Q.; Jia, M.-Q.; You, S.-L. Enantioselective N-Heterocyclic Carbene-Catalyzed Michael Addition to α,β-Unsaturated Aldehydes by Redox Oxidation. *Org. Lett.* **2011**, *13*, 4080–4083.

(2) Hamashima, Y.; Hotta, D.; Sodeoka, M. Direct Generation of Nucleophilic Chiral Palladium Enolate from 1,3-Dicarbonyl Compounds: Catalytic Enantioselective Michael Reaction with Enones. *J. Am. Chem. Soc.* **2002**, *124*, 11240–11241.

(3) Watanabe, M.; Ikagawa, A.; Wang, H.; Murata, K.; Ikariya, T. Catalytic Enantioselective Michael Addition of 1,3-Dicarbonyl Compounds to Nitroalkenes Catalyzed by Well-Defined Chiral Ru Amido Complexes. *J. Am. Chem. Soc.* **2004**, *126*, 11148–11149.

(4) Gibson, D. Carbon-Bonded Beta-Diketone Complexes. *Coord. Chem. Rev.* **1969**, *4*, 225–240.

(5) Melby, L. R.; Rose, N. J.; Abramson, E.; Caris, J. C. Synthesis and Fluorescence of Some Trivalent Lanthanide Complexes. *J. Am. Chem. Soc.* **1964**, *86*, 5117–5125.

(6) Vigato, P. A.; Peruzzo, V.; Tamburini, S. The Evolution of β-Diketone or β-Diketophenol Ligands and Related Complexes. *Coord. Chem. Rev.* **2009**, *253*, 1099–1201.

(7) Kawaguchi, S. Variety in the Coordination Modes of β-Dicarbonyl Compounds in Metal Complexes. *Coord. Chem. Rev.* **1986**, *70*, 51–84.

(8) Allen, G.; Dwek, R. A. An N.M.R. Study of Keto-Enol Tautomerism in β-Diketones. *J. Chem. Soc. B* **1966**, 161–163.

(9) Emsley, J. The Composition, Structure and Hydrogen Bonding of the β-Diketones. *Struct. Bond.* **1984**, *57*, 147–199.

(10) Emsley, J.; Freeman, N. J. β-Diketone Interactions: Part 5. Solvent Effects on the Keto$\rightleftharpoons$Enol Equilibrium. *J. Mol. Struct.* **1987**, *161*, 193–204.

(11) Nichols, M. A.; Waner, M. J. Kinetic and Mechanistic Studies of the Deuterium Exchange in Classical Keto-Enol Tautomeric Equilibrium Reactions. *J. Chem. Educ.* **2010**, *87*, 952–955.

(12) Egan, M. E.; Pearson, M.; Weiner, S. A.; Rajendran, V.; Rubin, D.; Glockner-Pagel, J.; Canny, S.; Du, K.; Lukacs, G. L.; Caplan, M. J. Curcumin, a Major Constituent of Turmeric, Corrects Cystic Fibrosis Defects. *Science* **2004**, *304*, 600–602.

(13) Cartiera, M. S.; Ferreira, E. C.; Caputo, C.; Egan, M. E.; Caplan, M. J.; Saltzman, W. M. Partial Correction of Cystic Fibrosis Defects with PLGA Nanoparticles Encapsulating Curcumin. *Mol. Pharmaceutics* **2010**, *7*, 86–93.

(14) Aggarwal, B. B.; Kumar, A.; Bharti, A. C. Anticancer Potential of Curcumin: Preclinical and Clinical Studies. *Anticancer Res.* **2003**, *23*, 363–398.

(15) Harada, T.; Giorgio, L.; Harris, T. J.; Pham, D.-T.; Ngo, H. T.; Need, E. F.; Coventry, B. J.; Lincoln, S. F.; Easton, C. J.; Buchanan, G.; Kee, T. W. Diamide Linked γ-Cyclodextrin Dimers as Molecular-Scale Delivery Systems for the Medicinal Pigment Curcumin to Prostate Cancer Cells. *Mol. Pharmaceutics* **2013**, *10*, 4481–4490.

(16) Baum, L.; Ng, A. Curcumin Interaction with Copper and Iron Suggests One Possible Mechanism of Action in Alzheimer's Disease Animal Models. *J. Alzheimers Dis.* **2004**, *6*, 367–377.

(17) Yang, F. S.; Lim, G. P.; Begum, A. N.; Ubeda, O. J.; Simmons, M. R.; Ambegaokar, S. S.; Chen, P. P.; Kayed, R.; Glabe, C. G.; Frautschy, S. A.; Cole, G. M. Curcumin Inhibits Formation of Amyloid β Oligomers and Fibrils, Binds Plaques, and Reduces Amyloid *in Vivo*. *J. Biol. Chem.* **2005**, *280*, 5892–5901.

(18) Yanagisawa, D.; Shirai, N.; Amatsubo, T.; Taguchi, H.; Hirao, K.; Urushitani, M.; Morikawa, S.; Inubushi, T.; Kato, M.; Kato, F.; Morino, K.; Kimura, H.; Nakano, I.; Yoshida, C.; Okada, T.; Sano, M.; Wada, Y.; Wada, K.-n.; Yamamoto, A.; Tooyama, I. Relationship between the Tautomeric Structures of

Curcumin Derivatives and Their Aβ-Binding Activities in the Context of Therapies for Alzheimer's Disease. *Biomaterials* **2010**, *31*, 4179–4185.

(19) Priyadarsini, K. I. Photophysics, Photochemistry and Photobiology of Curcumin: Studies from Organic Solutions, Bio-Mimetics and Living Cells. *J. Photoch. Photobio. C* **2009**, *10*, 81–95.

(20) Aggarwal, B. B.; Harikumar, K. B. Potential Therapeutic Effects of Curcumin, the Anti-Inflammatory Agent, against Neurodegenerative, Cardiovascular, Pulmonary, Metabolic, Autoimmune and Neoplastic Diseases. *Int. J. Biochem. Cell Biol.* **2009**, *41*, 40–59.

(21) Adhikary, R.; Mukherjee, P.; Kee, T. W.; Petrich, J. W. Excited-State Intramolecular Hydrogen Atom Transfer and Solvation Dynamics of the Medicinal Pigment Curcumin. *J. Phys. Chem. B* **2009**, *113*, 5255–5261.

(22) Ghosh, R.; Mondal, J. A.; Palit, D. K. Ultrafast Dynamics of the Excited States of Curcumin in Solution. *J. Phys. Chem. B* **2010**, *114*, 12129–12143.

(23) Gilli, G.; Bellucci, F.; Ferretti, V.; Bertolasi, V. Evidence for Resonance-Assisted Hydrogen Bonding from Crystal-Structure Correlations on the Enol Form of the β-Diketone Fragment. *J. Am. Chem. Soc.* **1989**, *111*, 1023–1028.

(24) Kolev, T. M.; Velcheva, E. A.; Stamboliyska, B. A.; Spiteller, M. DFT and Experimental Studies of the Structure and Vibrational Spectra of Curcumin. *Int. J. Quantum Chem.* **2005**, *102*, 1069–1079.

(25) Chignell, C. F.; Bilskj, P.; Reszka, K. J.; Motten, A. G.; Sik, R. H.; Dahl, T. A. Spectral and Photochemical Properties of Curcumin. *Photochem. Photobiol.* **1994**, *59*, 295–302.

(26) Lockwood, K. Solvent Effect on Keto-Enol Equilibrium of Acetoacetic Ester. *J. Chem. Educ.* **1965**, *42*, 481–482.

(27) Russell, P. The Effect of Solvent on the Keto–Enol Tautomerism of Some α-Acylphenylacetonitriles. *J. Am. Chem. Soc.* **1952**, *74*, 2654–2656.

(28) Dawber, J.; Crane, M. Keto–Enol Tautomerization: A Thermodynamic and Kinetic Study. *J. Chem. Educ.* **1967**, *44*, 150–152.

(29) Drexler, E.; Field, K. An NMR Study of Keto–Enol Tautomerism in β-Dicarbonyl Compounds. *J. Chem. Educ.* **1976**, *53*, 392–393.

(30) Grushow, A.; Zielinski, T. Hydrogen Bonding Using NMR: A New Look at the 2,4-Pentanedione Keto-Enol Tautomer Experiment. *J. Chem. Educ.* **2002**, *79*, 707–714.

(31) Cook, G.; Feltman, P. M. Determination of Solvent Effects on Keto–Enol Equilibria of 1,3-Dicarbonyl Compounds Using NMR - Revisiting a Classic Physical Chemistry Experiment. *J. Chem. Educ.* **2007**, *84*, 1827–1829.

(32) López-Tobar, E.; Blanch, G.; Ruiz del Castillo, M.; Sanchez-Cortes, S. Encapsulation and Isomerization of Curcumin with Cyclodextrins Characterized by Electronic and Vibrational Spectroscopy. *Vib. Spectrosc.* **2012**, *62*, 292–298.

(33) Payton, F.; Sandusky, P.; Alworth, W. L. NMR Study of the Solution Structure of Curcumin. *J. Nat. Prod.* **2007**, *70*, 143–146.

(34) Bertolasi, V.; Gilli, P.; Ferretti, V.; Gilli, G. Evidence for Resonance-Assisted Hydrogen Bonding. 2. Intercorrelation between Crystal Structure and Spectroscopic Parameters in Eight Intramolecularly Hydrogen Bonded 1,3-Diaryl-1,3-Propanedione Enols. *J. Am. Chem. Soc.* **1991**, *113*, 4917–4925.

(35) Bernabé-Pineda, M.; Ramírez-Silva, M. T.; Romero-Romo, M.; González-Vergara, E.; Rojas-Hernández, A. Determination of Acidity Constants of Curcumin in Aqueous Solution and Apparent Rate Constant of Its Decomposition. *Spectrochim. Acta A* **2004**, *60*, 1091–1097.

(36) Wang, Z. F.; Leung, M. H. M.; Kee, T. W.; English, D. S. The Role of Charge in the Surfactant-Assisted Stabilization of the Natural Product Curcumin. *Langmuir* **2010**, *26*, 5520–5526.

(37) Wang, Y. J.; Pan, M. H.; Cheng, A. L.; Lin, L. I.; Ho, Y. S.; Hsieh, C. Y.; Lin, J. K. Stability of Curcumin in Buffer Solutions and Characterization of Its Degradation Products. *J. Pharm. Biomed. Anal.* **1997**, *15*, 1867–1876.

(38) Adhikary, R.; Carlson, P. J.; Kee, T. W.; Petrich, J. W. Excited-State Intramolecular Hydrogen Atom Transfer of Curcumin in Surfactant Micelles. *J. Phys. Chem. B* **2010**, *114*, 2997–3004.

(39) Takamuku, T.; Tabata, M.; Yamaguchi, A.; Nishimoto, J.; Kumamoto, M.; Wakita, H.; Yamaguchi, T. Liquid Structure of Acetonitrile-Water Mixtures by X-Ray Diffraction and Infrared Spectroscopy. *J. Phys. Chem. B* **1998**, *102*, 8880–8888.

(40) Bertie, J.; Lan, Z. Liquid Water-Acetonitrile Mixtures at 25 °C: The Hydrogen-Bonded Structure Studied through Infrared Absolute Integrated Absorption Intensities. *J. Phys. Chem. B* **1997**, *101*, 4111–4119.

(41) Venables, D.; Schmuttenmaer, C. Spectroscopy and Dynamics of Mixtures of Water with Acetone, Acetonitrile, and Methanol. *J. Chem. Phys.* **2000**, *113*, 11222–11236.

(42) Max, J.; Chapados, C. Infrared Spectroscopy of Acetone-Water Liquid Mixtures. I. Factor Analysis. *J. Chem. Phys.* **2003**, *119*, 5632–5643.

(43) D'Cunha, C.; Morozov, A. N.; Chatfield, D. C. Theoretical Study of HOCl-Catalyzed Keto–Enol Tautomerization of β-Cyclopentanedione in an Explicit Water Environment. *J. Phys. Chem. A* **2013**, *117*, 8437–8448.

(44) Gonz'alez-Rivas, N.; Cedillo, A. Solvent Effects on the Energetic Parameters and Chemical Reactivity in The Keto–Enol Tautomeric Equilibrium of Substituted Carbonyl Compounds. *Comp. Theor. Chem.* **2012**, *994*, 47–53.

(45) Alagona, G.; Ghio, C.; Nagy, P. I. The Catalytic Effect of Water on the Keto–Enol Tautomerism. Pyruvate and Acetylacetone: A Computational Challenge. *Phys. Chem. Chem. Phys.* **2010**, *12*, 10173–10188.

(46) Yamabe, S.; Tsuchida, N.; Miyajima, K. Reaction Paths of Keto–Enol Tautomerization of β-Diketones. *J. Phys. Chem. A* **2004**, *108*, 2750–2757.

CHAPTER 6

NANOPRECIPITATION AND SPECTROSCOPIC CHARACTERISATION OF CURCUMIN-ENCAPSULATED POLYESTER NANOPARTICLES

6.1 Abstract

This study describes a simple one-step nanoprecipitation method to prepare curcumin-encapsulated polyester nanoparticles (Cur-polyester NP). Cur-polyester NP of about 100 nm in diameter with a negatively charged surface were prepared using three biodegradable polyesters, namely polylactate, poly(lactide-*co*-glycolide) and poly(ε-caprolactone). The degradation of curcumin in water is investigated and the encapsulation of curcumin in these polyester nanoparticles greatly suppressed curcumin degradation due to its segregation from water. The UV-visible absorption spectra of the Cur-polyester NP indicate that the local environment of curcumin is similar to that of the palisade layer of micelles. In addition, fluorescence emission has a quantum yield of 4 – 5 %, which is higher than that of curcumin in a micellar system. The fluorescence quantum yields of the Cur-polyester NP are comparable to those of curcumin in organic solvents, further supporting that the polyester nanoparticles are capable of excluding water from the encapsulated curcumin. Furthermore, the results from femtosecond fluorescence upconversion spectroscopy reveal that not only there is a decrease in the signal amplitude corresponding to solvent reorganisation of the excited state of curcumin, but also a lack of deuterium isotope effect in the fluorescence lifetime of the

Cur-polyester NP compared with curcumin in micellar systems. These results indicate that the interaction between curcumin and water in the Cur-polyester NP is weaker than that in micelles. Therefore, the stability of curcumin is greatly improved due to effective segregation from water as curcumin is encapsulated by the polyester nanoparticles.

6.2 Introduction

Curcumin, a hydrophobic polyphenol consists of a 1,3-diketone moiety, is the major component of the yellow pigments found in turmeric [1, 2]. It has been shown that curcumin exhibits a number of medicinal benefits, including anti-cancer, anti-Alzheimer's and anti-inflammatory properties [3–10], however, poor solubility and stability in an aqueous environment hinder its bioavailability. Curcumin has a poor solubility in an aqueous environment ($\sim 10\,\mu g\,mL^{-1}$) due to its hydrophobicity [11, 12]. In contrast, it is highly soluble and stable in polar organic solvent, namely methanol, acetone and tetrahydrofuran (THF). Payton et al. showed that the majority of curcumin exists in the keto-enol form as shown in Figure 6.1 [13]. Figure 6.1 also illustrates the intramolecular hydrogen bonding in the keto-enol moiety and the π-conjugation in curcumin. The π-conjugation enables a strongly allowed $\pi-\pi^*$ transition, resulting an intense absorption band around 420 nm [14, 15]. Although curcumin is non-fluorescent in water due to efficient fluorescence quenching by water molecules and self-quenching of fluorescence since the aqueous environment promotes aggregation of curcumin, the fluorescence quantum yield increases as the solvent environment becomes non-polar [14, 16, 17]. Previous work has demonstrated that solvation and excited-state intramolecular hydrogen transfer (ESIHT) in the keto-enol moiety of curcumin are the major relaxation pathways of its excited state [18–20]. In particular, the ESIHT of curcumin exhibits slow dynamics in deuterated solvents while solvation remains unaffected [18, 19].

It has been shown that the aqueous solubility of curcumin is improved in an alkaline environment as the hydroxyl groups of curcumin are deprotonated. However, this reaction leads to a rapid degradation of curcumin [21, 22]. The degradation of curcumin has also been studied in a physiological environment and more than 50 % of curcumin is degraded within 30 min [21, 23]. Furthermore, hydrolysis of curcumin has been linked to its degradation mechanism, with *trans*-6-(4'-hydroxy-3'-methoxyphenyl)-2,4-dioxo-5-hexenal as the major product [21]. Molecular fragmentation of this species gives rise to other minor products, including vanillin, ferulic acid and feruloyl methane [21]. In order to suppress the degradation of curcumin in water, a number of delivery systems, including cyclodextrins, micellar system and polymer nanoparticles, have

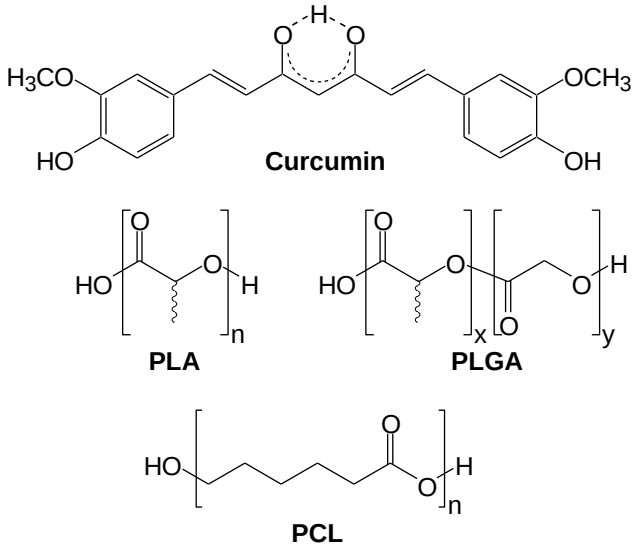

Figure 6.1. Chemical structure of curcumin, polylactate (PLA), poly(D,L-lactide-*co*-glycolide) (PLGA) and poly(ε-caprolactone) (PCL).

been used to improve the bioavailability of curcumin. [15, 16, 23–26]. The two main features that enable a delivery agent to solubilise and stabilise curcumin are a hydrophobic core and a hydrophilic outer layer. The hydrophobic regions encapsulate curcumin to segregate it from water, improving the stability by suppressing hydrolysis of curcumin. In addition, the hydrophilic outer layer interacts with water, which enables the curcumin-delivery agent complex to remain suspended in water.

The use of polyester nanoparticle as delivery agents has been under extensive research for their biocompatability [27–30]. It has been shown that polyester nanoparticles, in particular poly(D,L-lactide-*co*-glycolide) (PLGA) and poly(ε-caprolactone) (PCL), undergo hydrolysis of their ester bonds to form smaller units, which are further metabolised by cells [31, 32]. Recent studies have demonstrated efficient delivery of curcumin by biodegradable polyester nanoparticles [30, 33–38]. These nanoparticles exhibit medicinal effects against cancer, cystic fibrosis and wound healing. It is well established that these nanoparticles accumulate in solid tumours due to enhanced permeability and retention (EPR) effect, which is a phenomenon of defective vessels and inefficient lymphatic drainage of tumours [39–42]. The defective anatomy of the blood vessel in tumours leads to extensive leakage of blood plasma components and these nanoparticles. As a result of the poor lymphatic clearance, these nanoparticles are retained in the tumour [40, 41, 43]. It is also suggested that the EPR effect de-

pends on particle size. On one hand, small particles with a diameter of less than 10 nm have short retention in the bloodstream as they are easily cleared by the kidney [39–42]. On the other hand, larger particles with a diameter greater than 10 nm have a longer retention time in the bloodstream. Furthermore, because the pore cut-off size of blood vessels in the circulation system is about 100 nm, particles with a size between 10 nm and 100 nm can be passively transported from the circulation system and then be accumulated in tumours due to the lack of efficient lymphatic clearance [42]. As a consequence, particles with a size of 10 – 100 nm are necessary to benefit from the EPR effect. The aim of this study is to prepare polyester nanoparticles with the following three desirable features to improve the bioavailability of curcumin: (1) a hydrophobic environment to encapsulate curcumin, (2) a hydrophilic outer layer to enable suspension of the curcumin-delivery agent complex in water and (3) a particle size of less than 100 nm to maximise the EPR effect.

In this chapter, we report a one-step nanoprecipitation method for the preparation of nano-sized ($\sim$ 100 nm) curcumin-encapsulated biodegradable polyester nanoparticles (Cur-polyester NP) using polylactate (PLA), PLGA and PCL. The resulting Cur-polyester NP exhibit a strong UV-visible absorption around 420 nm and fluorescence emission around 500 nm. These spectroscopic characteristics indicate the presence of curcumin in an environment similar to the palisade layer of micelles [16, 19]. Furthermore, curcumin has a higher fluorescence quantum yield when it is encapsulated by the polyester nanoparticles than it is by micelles. The increase in the fluorescence quantum yield implies that there are weaker interactions between curcumin and water in the polyester nanoparticles than in micelles. In addition, the stability of curcumin is improved significantly in all three Cur-polyester NP. In particular, no decomposition was observed for curcumin encapsulated in PLA nanoparticles. The high stability is attributable to the lack of interaction between curcumin and water, which is also supported by time-resolved fluorescence upconversion results. The low signal amplitude for solvent reorganisation and the absence of a deuterium isotope effect in the fluorescence lifetime of Cur-polyester NP indicate that there are limited interactions between curcumin and water. Therefore, the polyester nanoparticles segregate the encapsulated curcumin from water, suppressing the hydrolysis of curcumin.

6.3 Materials and Methods

6.3.1 Materials

Curcumin (purity $> 98\%$) was purchased from LKT Laboratories. Polylactic acid (average M_w:60 000), poly(D,L-lactide-*co*-glycolide) (50:50 lactide : glycolide, M_w: 40 000 – 75 000) and poly(ε-caprolactone) (average M_n:45 000) were sourced from Sigma Aldrich. Acetone (AR grade) from Chem-Supply and Methanol (isocratic HPLC grade, 254 nm) from Scharlau were used as received. Tetrahydrofuran (HPLC grade, without stabiliser) was purchased from Scharlau and freshly distilled before used. Water from a Millipore Milli-Q NANOpure water system was used in all experiments.

6.3.2 Preparation of Curcumin-polyester Nanoparticles

The Cur-polyester NP were prepared by a nanoprecipitation method as described previously with modifications [37, 38, 44]. For the preparation of curcumin encapsulated PLA nanoparticles (Cur-PLA NP), stock solutions of 100 mg/mL PLA in chloroform and 1 mg/mL curcumin in THF were prepared. A volume of 50-µL of the curcumin stock solution was diluted with 445 µL of THF. A 5-µL aliquot of the PLA stock solution was added to the curcumin solution (THF) to yield a 500 µL curcumin/PLA solution. For the preparation of curcumin encapsulated PLGA or PCL nanoparticles (Cur-PLGA NP or Cur-PCL NP), stock solutions of 4 mg/mL PLGA or PCL, and curcumin in acetone were prepared. A volume of 125-µL PLGA or PCL stock solution was mixed with 25 µL to yield a 150-µL curcumin/PLGA or curcumin/PCL solution. The ratio of curcumin:polyester in the resulting curcumin/polyester solutions was 1:5 by weight for curcumin:PLGA or PCL, and 1:10 for curcumin:PLA. For a 1:10 curcumin:polyester by weight solution of curcumin/PLGA or curcumin/PCL solution, a volume of 12.5-µL curcumin stock solution was mixed with 125 µL polyester stock, which was followed by an addition of 12.5-µL acetone resulting a 150-µL. All the experiments were done with a weight ratio of 1:10 for Cur-PLA NP and 1:5 for Cur-PLGA NP or Cur-PCL NP, except for the investigation on aqueous stability, where a 1:10 ratio by weight for Cur-PLGA NP and Cur-PCL NP was used. It is important to note that the molar ratio of curcumin to monomer units are 1:50, 1:15 and 1:30 for

a 1:10 curcumin:PLA, a 1:5 and a 1:10 curcumin:PLGA or curcumin:PCL ratio by weight, respectively. This curcumin/polyester solution was then injected into 40 mL of Milli-Q water using a glass syringe and stirred for 30 min in dark. The overall %v/v of the organic solvent in the organic/water mixture was approximately 0.4 % for acetone (Cur-PLGA NP and Cur-PCL NP); and about 1.3 % for THF/chloroform (Cur-PLA NP). In particular, chloroform was about 0.02 %. The organic solvent was then removed under reduced pressure at 40 °C for 30 min to ensure a complete removal. The resulting Cur-polyester NP solution was filtered with a 0.45 µm hydrophilic syringe filter (Minisart), which was followed by an additional filtration with a 0.2 µm hydrophilic syringe filter (Minisart) to remove large aggregates. The concentration of Cur-polyester NP solution was estimated from the absorbance at 425 nm before and after filtering of the Cur-polyester NP solution. The yield of the final Cur-polyester NP solutions was about 50 %. Care was taken to limit the exposure of the Cur-polyester NP solutions to ambient light.

6.3.3 Dynamic Light Scattering Measurement

The particle size distribution and zeta potential of Cur-polyester NP were characterised by dynamic light scattering using a Malvern Zetasizer nano ZS. For the particle size distribution measurements, the concentration of the Cur-polyester NP solutions was approximately 1.5 ppm. The measurements were made with a 633 nm laser at a back scattering angle of 173°. For the zeta potential measurements, the concentration of the Cur-polyester NP solutions was about 4 ppm. All results were collected using a disposable folded capillary cell and measurements were taken at 25 °C with a 2-min equilibration time before the start of measurement for each Cur-polyester NP solution. Measurements were done in triplicates for each experiment. The particle size was the cumulants mean of a distribution with a polydispersity index less than 0.3 [34]. Both the diameter and zeta potential of the nanoparticles were reported as the mean of three independent experiments and the error was the standard deviation of the mean.

6.3.4 Steady State UV-visible Absorption and Fluorescence Spectroscopy

UV-visible absorption spectra of Cur-polyester NP from 350 – 700 nm were recorded with a Varian Cary 5000 UV-visible/NIR spectrophotometer. For the determination of the stability of Cur-polyester NP, UV-visible spectra of an approximately $\sim$ 1-ppm Cur-polyester NP were collected at 15-min intervals for 12 h at 25 °C. The rate of degradation of the Cur-polyester NP was reported as the mean of three independent experiments and the error was the standard deviation of the mean.

Fluorescence spectra of Cur-polyester NP (430 – 750 nm) were recorded with a Varian Cary Eclipse Fluorescence spectrophotometer. Care was taken to ensure the absorbance of the Cur-polyester NP solution at the excitation wavelength was below 0.1 to minimise the inner filter effect. The excitation wavelength used was 514 nm and 420 nm for Rhodamine B and curcumin, respectively. A 5-nm slit width was set for both excitation and emission wavelength. The fluorescence quantum yield of Cur-polyester NP was calculated by referencing reported fluorescence quantum yields in literature, which are 3 % and 31 % for curcumin in methanol and Rhodamine B in water, respectively [15, 45]. The fluorescence quantum yields of Cur-polyester NP were reported as the mean of three independent experiments and the error was the standard deviation of the mean.

6.3.5 Time-resolved Fluorescence Spectroscopy

For the fluorescence lifetime measurements, the Cur-polyester NP solutions were further concentrated under reduce pressure and filtered with a 0.2 µm hydrophilic syringe filter (Minisart). The final concentration was about 35 ppm for Cur-PLA NP, 15 ppm for Cur-PLGA NP and 80 ppm for Cur-PCL NP solution. For the studies of Cur-polyester NP in deuterated water, a 1:1 volume ratio of deuterated water was introduced into the concentrated Cur-polyester NP solution. This solution of Cur-polyester NP with deuterated water was further concentrated under reduce pressure, which was followed by filtration with a 0.2 µm hydrophilic syringe filter (Minisart). The resulting solutions had a concentration of 35 ppm, 15 ppm and 45 ppm of curcumin for Cur-PLA

NP, Cur-PLGA NP and Cur-PCL NP, respectively. All measurements were performed on freshly prepared samples at room temperature using a quartz cuvette with a 2-mm path length.

The excited state lifetime was measured with the fluorescence upconversion technique. Briefly, the laser source was a Ti:sapphire mode-locked oscillator (Spectra Physics, Tsunami) pumped by a 8 W Nd:YVO_4 diode laser (Spectra Physics, Millennia Pro-s). This output seeded a Ti:sapphire regenerative amplifier (Spectra-Physics, Spitfire Pro XP) pumped by a 20 W Q-switched Nd:YLF laser (Spectra-Physics, Empower). The output of the amplifier was centred at 800 nm with a repetition rate of 1 kHz and pulse duration of 100 fs, which was then split into excitation and gate beams. Frequency-doubled pulses (400 nm) at 0.05 mW were used to excite the sample and fluorescence were collected with a plano-convex lens. The gate pulse and fluorescence were then focussed onto a 0.4 mm type-I BBO crystal to generate sum frequency signals, which were detected by a photomultiplier tube attached to a monochromator. The fluorescence decay of Cur-polyester NP was monitored at 500 nm. It has been shown that the propagation of a focusing light through inhomogeneous media results in scattering and distortions [46–49]. In particular, the temporal distortion of the ultrashort pulse on transmission through polystyrene particle solution has been demonstrated [49]. Furthermore, the nonlinear property of curcumin may induce nonlinear distortion of the ultrashort pulse [50]. Therefore, an instrument response function of 800-fs (fwhm) was used based on the goodness of fit. Each experiment is an average of eight scans with a 3000-ps time window. A maximum of 10 % curcumin photodegradation was observed in the experiment. The average fluorescence lifetime was reported as the mean of three independent experiments and the error was estimated from the confidence intervals determined by the support plane analysis [51].

6.4 Results and Discussion

6.4.1 Characterisation of Curcumin-polyester Nanoparticles

Three types of Cur-polyester NP, namely Cur-PLA NP, Cur-PLGA NP and Cur-PCL NP, were prepared using the one-step nanoprecipitation method described previously. The resulting Cur-polyester NP were characterised using dynamic light scattering for their diameters and zeta potentials, of which the values are summarised in Table 6.1. The nanoparticle size distribution and zeta potential results are shown in Figure 6.2. The Cur-polyester NP exhibit no observable particle aggregation within the time window of measurements. Although no observable aggregation within the short time frame of the experiments, the Cur-polyester NP show a slight increase in their particle sizes after a week, as shown in Figure 6.3. The gradual increase in the particle size indicates particle aggregation of the Cur-polyester NP over a long time period.

The Cur-polyester NP have diameters of 89 ± 16, 68 ± 16 and 96 ± 20 nm for Cur-

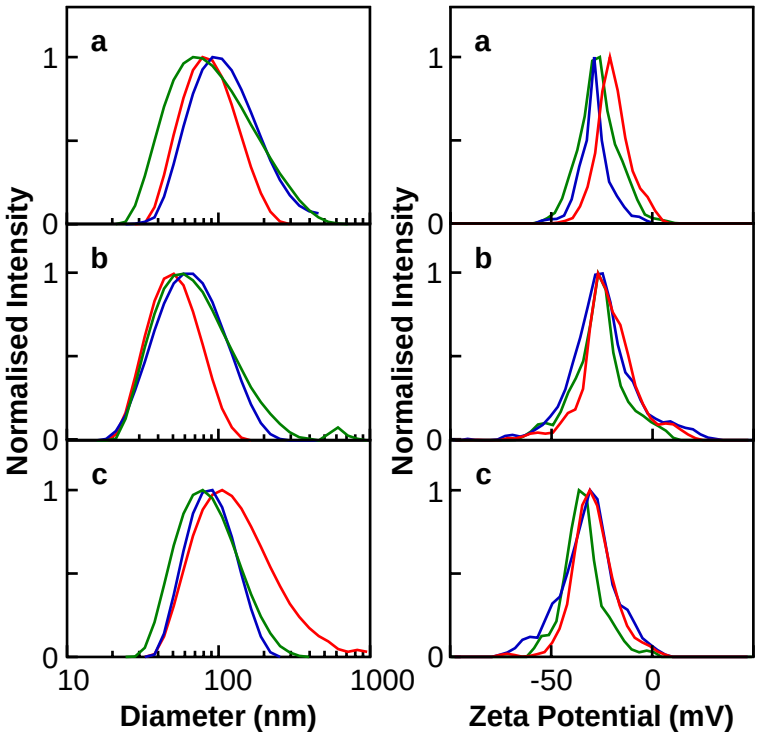

Figure 6.2. Three independent experiments on the particle size distribution (right) and zeta potential (left) of (a) Cur-PLA, (b) Cur-PLGA and (c) Cur-PCL nanoparticles in neat water.

Table 6.1. Summary of Particle Diameter, Zeta Potential, Rate of Degradation ($k_{\text{degrad.}}$) and Fluorescence Quantum Yield (Φ_{fl}) of Curcumin-encapsulated Polyester Nanoparticles.[a]

Polyester	**Diameter** (nm)	**Number of Curcumin in NP**[b] ($\times 10^4$)	**Zeta Potential** (mV)	$k_{\text{degrad.}}$ (% h^{-1})	Φ_{fl}	**Distance between Curcumin**[d] (nm)
PLA	89 ± 16	8.0	-24 ± 5	0.05 ± 0.05	0.05 ± 0.01	2.07
PLGA	68 ± 16	7.0	-24 ± 2	0.15 ± 0.06	0.04 ± 0.01	1.65
				0.49 ± 0.18[c]		
PCL	96 ± 20	17.4	-28 ± 4	0.14 ± 0.05	0.05 ± 0.01	1.72
				0.57 ± 0.20[c]		

[a]The reported values are the mean value of three independent experiments and the error values are the standard deviation of the mean.
[b]See Appendix C.1.
[c]A ratio of 1:5 curcumin:polyester by weight or molar ratio of curcumin:monomer unit of 1:15 solution is used.
[d]See Appendix C.2.

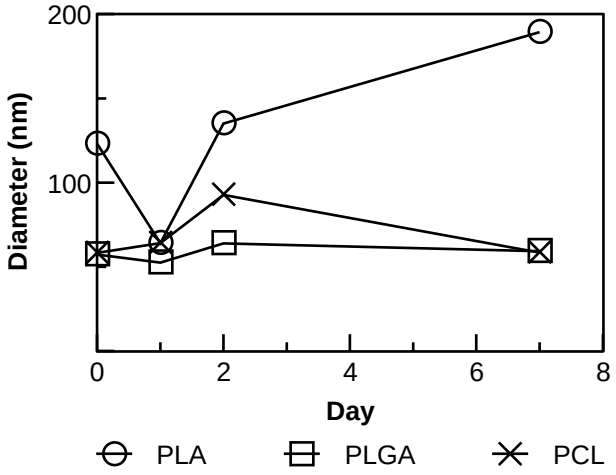

Figure 6.3. Particle size measurements of Cur-PLA (circles), Cur-PLGA (squares) and Cur-PCL (crosses) nanoparticles in neat water over a week.

PLA NP, Cur-PLGA NP and Cur-PCL NP, respectively. From the diameters of Cur-polyester NP, the volume of polyester nanoparticles is estimated assuming they are spherical in shape, thus the average number of curcumin per polyester nanoparticle is estimated using the method detailed in Appendix C.1 and the results are summarised in Table 6.1. There are about 8×10^4, 7×10^4 and 17×10^4 curcumin molecules in each polyester nanoparticle on average for Cur-PLA NP, Cur-PLGA NP and Cur-PCL NP, respectively. Furthermore, a study has demonstrated that the particle size is dependent on the type of organic solvent used to dissolve the polyester [52]. It has been shown that acetone gives smaller sized polyester nanoparticles than THF due to its higher polarity [52]. Although acetone is useful in the preparation of Cur-PLGA NP and Cur-PCL NP, the PLA used in this study has a poor solubility in acetone because of its large molecular weight compared with those from literature [53]. To overcome this, a dilute PLA solution (THF) with a small amount of chloroform was used to ensure a complete dissolution. Therefore, to achieve a 1:5 ratio of curcumin to PLA by weight, a larger volume of PLA in THF/chloroform was injected into water. However, a poor yield of nanoparticles was observed with this condition. Therefore, a 1:10 ratio of curcumin to PLA by weight was used with the same concentration of PLA as that in PLGA and PCL. In addition to the solvent dependence on the sizes of nanoparticle, it has been demonstrated that the diameters of polyester nanoparticles are also dependent on the concentration of polyester in organic solvent used in the nanoprecipitation [52, 54]. With a low concentration of polymer stock solution, the yield of small sized

nanoparticles increases significantly compared with those with a higher polymer concentration stock [52, 54]. In this study, the low concentration of polyester in organic phase ($\sim$ 3000 ppm for PLGA or PCL; and $\sim$ 1000 ppm for PLA) ensures a complete dissolution of the polyester, hence minimises interstrand interactions and enables the formation of nanoparticles of small sizes [54]. Furthermore, the injection method of the organic phase into the aqueous phase using a syringe promotes fast mixing of the two phases, facilitating the production of nano-sized particles. Our results are consistent with the classical nucleation theory, where polymer chains collapse in water into small spherical aggregates spontaneously upon injection of the organic phase [55]. The absence of significant interstrand interactions in a dilute polyester solution provides the optimal condition for nucleation. The particles then grow further by collision with the randomly dispersed solute molecules (curcumin and polyester) until the concentration of the solute molecules reaches an equilibrium level [55]. As the growth of the nanoparticles is dependent on the random collision, it is limited by the concentration of the solute molecules. The probability for successful collisions diminishes at a low solute concentration, such as the condition used in this study. This condition enables the particle size to remain small when the solute concentration reaches an equilibrium. In addition, it has been shown that an increase in the polarity of the final dispersant medium leads to reduction of large aggregates [52, 55]. Therefore, injecting a small volume of organic phase into the aqueous phase results in low organic:aqueous volume ratios of 1:266 for Cur-PLGA NP and Cur-PCL NP, and 1:80 for Cur-PLA NP, which yield a high polarity in the final dispersant medium. Cur-polyester NP prepared with the one-step nanoprecipitation method have particle sizes less than 100 nm, which are within the ideal size range for particles to benefit from the EPR effect that is important in the passive accumulation in solid tumour as discussed earlier.

In addition to the small particle size, the Cur-polyester NP exhibit negative zeta potentials of -24 ± 5, -24 ± 2 and -28 ± 4 mV for Cur-PLA NP, Cur-PLGA NP and Cur-PCL NP, respectively. The negative surface charge of the Cur-polyester NP is in good agreement with previous studies of nanoparticles that show colloidal stability [33, 35]. It is noteworthy that the negative surface charge of the Cur-polyester NP is a key property to enable colloidal stability as the repulsion of the surfaces of the Cur-polyester NP is greater than the van der Waals interaction between nanoparticles.

As a consequence, the Cur-polyester NP are able to form a stable suspension in water to deliver curcumin in the aqueous environment. Overall, the Cur-polyester NP have significant promise to address the lack of bioavailability of curcumin.

6.4.2 Solution Stability of Curcumin-polyester Nanoparticles

All three Cur-polyester NP have strong absorption in the UV-visible region with absorption maxima at 420 – 425 nm for Cur-PLA NP, Cur-PLGA NP and Cur-PCL NP, as shown in Figure 6.4 (solid curves). The polyesters are optically transparent in the visible spectrum and the absorption band observed around 420 nm is attributable to the $\pi-\pi^*$ transition of curcumin [15, 56]. The UV-visible absorption spectra of Cur-polyester NP are almost identical to those of curcumin encapsulated in micellar systems, namely, Triton X-100, cetyl trimethylammonium bromide (CTAB) and dodecyl trimethylammonium bromide (DTAB) [16, 19]. In addition, a shoulder in the absorption band is observed around 450 nm in all three Cur-polyester NP (as indicated by the solid arrows in Figure 6.4), which is vastly different from that of curcumin in an aqueous environment [23]. It has been suggested that curcumin is located at the palisade layer of the neutral and cationic micelles, in which the surrounding environment is similar to protic solvents [14, 18]. Similarly, these results suggest that curcumin is encapsulated in the polyester nanoparticle, where the local environment is similar to that of the palisade layer of micelles. Furthermore, Cur-polyester NP exhibit red-shifted fluorescence relative to their absorption, as shown in Figure 6.4 (dashed curves). The fluorescence maxima are at 502 – 508 nm and the emission spectra of Cur-polyester NP resemble those of curcumin in TX-100 and cationic micelles (CTAB and DTAB) [19], which support that curcumin is located in the polyester nanoparticle.

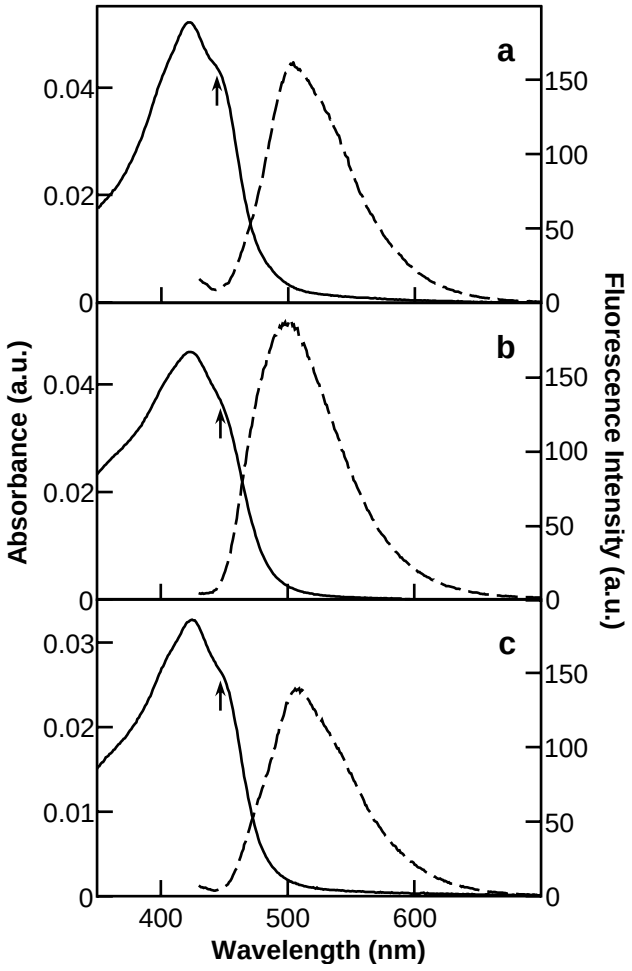

Figure 6.4. Steady state UV-visible absorption and fluorescence emission spectra of (a) Cur-PLA, (b) Cur-PLGA and (c) Cur-PCL nanoparticles in neat water.

Previous studies have shown that curcumin has a poor stability in the aqueous environment but it is stable inside micelles, plasma proteins and cyclodextrins [21, 24, 57]. The stability of curcumin in polyester nanoparticles was investigated with an expectation that a similar level of stabilisation to that provided by micelles should be observed. As the absorbance around 425 nm is attributable to the presence of curcumin in polyester nanoparticle solution, the stability of curcumin was investigated using UV-visible absorption spectroscopy. It follows that a decrease in the absorbance around 425 nm signifies the degradation of curcumin, as shown in Figure 6.5. The insets of Figure 6.5 display the degradation of curcumin in the polyester nanoparticles within a narrow absorbance range. The time dependent degradation fits well with a pseudo-zero-order kinetic model (represented as solid lines), of which the slope is used to determine the rate of degradation. The rates of degradation of curcumin in Cur-PLA NP, Cur-PLGA NP and Cur-PCL NP are summarised in Table 6.1. The pseudo-zero-order kinetics observed in curcumin degradation imply that only a small population is involved in the process, presumably at the surface of the nanoparticles. The degraded curcumin is then replenished at the surface by curcumin encapsulated within the interior, giving rise to an overall pseudo-zero-order kinetic.

The slow decays of the UV-visible absorption of curcumin in Cur-polyester NP reveal that curcumin is stable in the polyester nanoparticles. In particular, the Cur-PLA NP (Figure 6.5a) show almost no degradation of curcumin within 12 h. Previous studies have demonstrated the use of micelles, cyclodextrins and plasma protein to stabilise curcumin in aqueous environment [15, 16, 23, 24, 57]. Micelles show significant stabilisation of curcumin even at a pH 13 environment, where rapid decomposition of curcumin is expected [24]. In addition, a measurable fluorescence intensity of curcumin in micelles indicates that curcumin has weak interactions with water [16]. A significant level of stabilisation of curcumin is also observed in cyclodextrins and proteins, of which the fluorescence intensity is attributable to the association of curcumin with the hydrophobic interior of the delivery agents [23, 58]. The rates of degradation of $0.7\,\%\,\mathrm{h}^{-1}$ and $1.2\,\%\,\mathrm{h}^{-1}$ have been reported previously for curcumin encapsulated in γ-cyclodextrin dimers and human serum albumin protein, respectively [23, 58]. Furthermore, the stronger binding affinity of curcumin to plasma protein yields a higher stabilisation of curcumin, which suggests that the binding of curcumin to the hydropho-

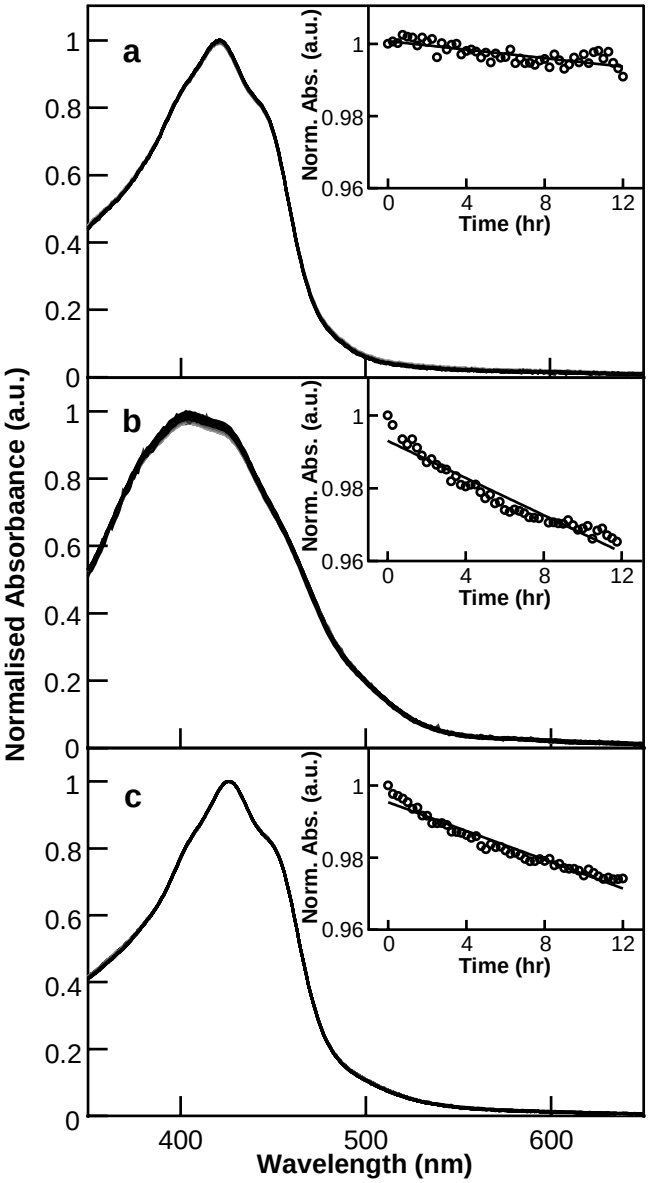

Figure 6.5. Stability of (a) Cur-PLA NP, (b) Cur-PLGA NP and (c) Cur-PCL NP in neat water by steady state UV-visible absorption spectroscopy. The insets show the decrease in the absorption maximum owing to degradation of curcumin. Note the narrow range of absorbance values in the inset.

bic region is essential for effectively stabilisation [58]. Therefore, it has been proposed that curcumin is encapsulated in the hydrophobic regions of the stabilising agent resulting suppression of degradation of curcumin. In other words, the hydrophobic region of the stabilising agent segregates curcumin from water and suppresses hydrolysis of curcumin [16, 23, 24].

The molar ratio of curcumin to polyester plays a role in the ability of the polyester nanoparticles to suppress curcumin degradation. The molar ratio of curcumin to the

monomer units presented in Figure 6.5 is 1:50 for Cur-PLA NP and 1:30 for Cur-PLGA NP or Cur-PCL NP. A higher concentration of curcumin is present in the Cur-PLGA NP and Cur-PCL NP, of which the results are shown in Figure 6.6. It is important to note that ineffective encapsulation of curcumin of PLA NP occurs with a molar ratio higher than 1:50, which results in precipitation of curcumin. With a molar ratio of approximately 1:15, the rate of degradation of curcumin increases for Cur-PLGA NP and Cur-PCL NP, as summarised in Table 6.1. The faster degradation of curcumin observed at a higher curcumin concentration suggests that the encapsulation by polyester nanoparticles is less efficient. As a consequence, a population of curcumin is located at the surface of the polyester nanoparticles and it inhibits the suppression of the degradation of curcumin. Overall, the Cur-polyester NP exhibit a slower decay of curcumin than that in micelles, cyclodextrins and proteins, suggesting that polyester nanoparticles are superior in suppressing the degradation of curcumin [15, 16, 23, 24, 57]. This

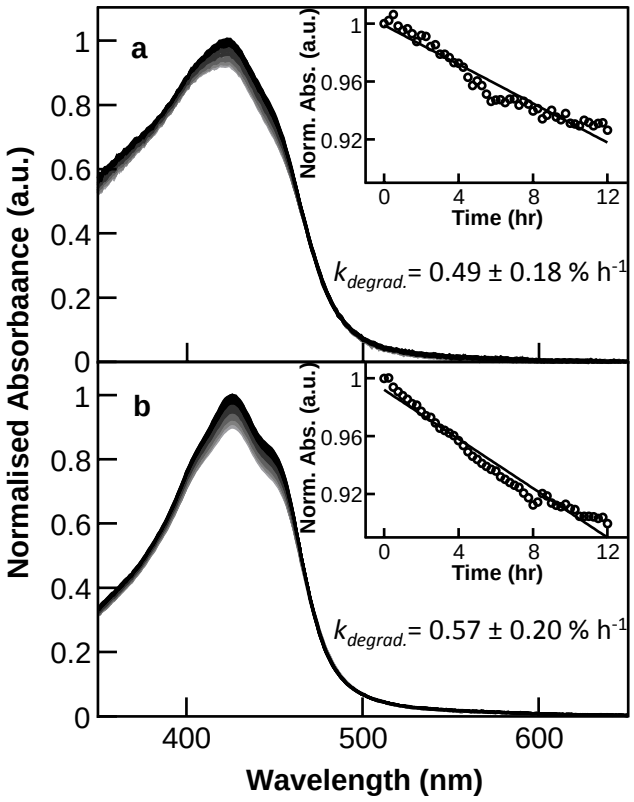

Figure 6.6. Stability of 1:15 curcumin:monomer unit mole ratio of (a) Cur-PLGA NP and (b) Cur-PCL NP in neat water by steady state UV-visible absorption spectroscopy. The insets show the decrease in the absorption maximum owing to degradation of curcumin.

phenomenon leads to a central question: what is the role of polyester nanoparticles on the suppression of curcumin degradation?

The fluorescence quantum yields (Φ_{fl}) of Cur-polyester NP, which are summarised in Table 6.1, are higher than those of curcumin in micelles [15, 16, 19]. It is important to note that in order to improve the signal to noise ratio, a 1:15 molar ratio for Cur-PLGA NP or Cur-PCL NP is used to investigate the photophysics of curcumin. The Φ_{fl} are 5 % for Cur-PLA NP and Cur-PCL NP, and 4 % for Cur-PLGA NP. These values are higher than that of curcumin in micelles ($\Phi_{fl} = 0.007 - 3\,\%$) [15]. In addition, the average distance between two adjacent curcumin molecules in Cur-polyester NP is estimated using the method detailed in Appendix C.2. The average distances between adjacent curcumin molecules all three polyester nanoparticles are less than 3 nm, as summarised in Table 6.1. The short distance between adjacent curcumin indicates that there is a high probability of self-quenching of fluorescence by Forster resonance energy transfer [59–61]. Furthermore, it has been shown that the Φ_{fl} of curcumin in the aqueous environment is substantially lower than that in non-polar environment [14, 16, 17]. The high Φ_{fl} of Cur-polyester NP implies that the curcumin is in an environment that is more hydrophobic than that of the palisade layer of micelles. The vibronic coupling between excited state curcumin and the O−H vibration of the solvent is an efficient mechanism for the nonradiative deactivation of the excited state of curcumin [62, 63]. In other words, it is relatively unlikely for water molecule to be present in the hydrophobic regions of the polyester nanoparticles, results in efficient exclusion of water and enhances the Φ_{fl} of curcumin. Therefore, the suppression of degradation of curcumin is attributable to the effective segregation of curcumin from water by polyester nanoparticles.

6.4.3 Time-resolved Fluorescence Spectroscopy of Curcumin-polyester Nanoparticles

Time-resolved fluorescence upconversion spectroscopy reveals further insight into the effective segregation of curcumin from water by polyester nanoparticles. The time-resolved fluorescence decays of the Cur-polyester NP were monitored at 500 nm with an excitation wavelength of 400 nm and a time window of 3000 ps. The 400-nm ex-

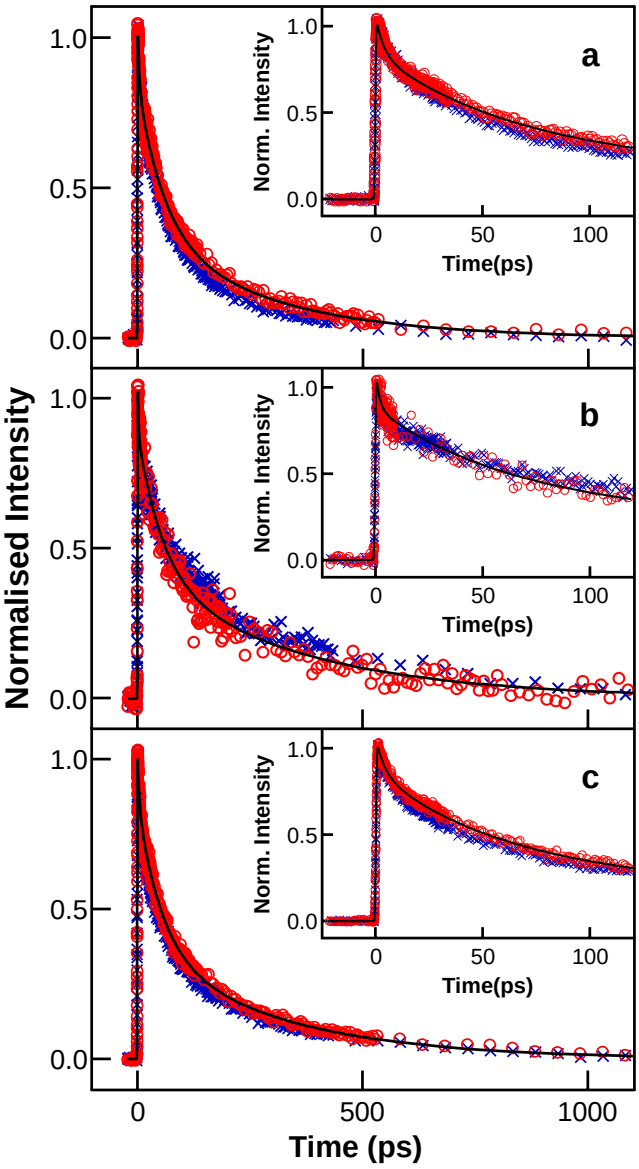

Figure 6.7. Fluorescence upconversion data of (a) Cur-PLA NP, (b) Cur-PLGA NP and (c) Cur-PCL NP in neat water (red circles and the best-fit curves are in black) and deuterated water (blue crosses) with the insets showing the early time decay from 0 – 120 ps. The well overlapped results signify the absence of any deuterium isotope effect in all three Cur-polyester NP.

Table 6.2. Fluorescence Upconversion Decay Parameters for Curcumin-encapsulated Polyester Nanoparticles.[a]

Polyester	**Solvent**	A_1	τ_1 (ps)	A_2	τ_2 (ps)	A_3	τ_3 (ps)	$\langle\tau\rangle$ (ps)
PLA	H_2O	0.19 ± 0.07	4 ± 2	0.46 ± 0.20	57 ± 30	0.35 ± 0.22	277 ± 98	124
PLA	D_2O	0.18 ± 0.09	3 ± 2	0.44 ± 0.19	41 ± 22	0.38 ± 0.21	200 ± 68	94
PLGA	H_2O	0.23 ± 0.12	2 ± 1	0.38 ± 0.23	66 ± 49	0.39 ± 0.23	378 ± 154	172
PLGA	D_2O	0.20 ± 0.10	3 ± 2	0.34 ± 0.25	63 ± 53	0.46 ± 0.20	380 ± 163	197
PCL	H_2O	0.17 ± 0.07	5 ± 3	0.47 ± 0.14	55 ± 25	0.35 ± 0.16	319 ± 103	140
PCL	D_2O	0.20 ± 0.07	4 ± 2	0.43 ± 0.13	45 ± 20	0.37 ± 0.15	255 ± 73	114

[a] The fluorescence upconversion traces, $f(t)$, were fitted with the multiexponential function $f(t) = A_1 e^{-t/\tau_1} + A_2 e^{-t/\tau_2} + A_3 e^{-t/\tau_3}$, where $A_1 + A_2 + A_3 = 1$. The reported values are the mean of three independent experiments and the error was estimated from the mean of confidence intervals determined by the support plane analysis [51].

citation wavelength is on the blue-side of the absorption spectra of the Cur-polyester NP. The excitation promotes the ground state curcumin to the excited state. In addition, monitoring the fluorescence decay at 500 nm, which is roughly the emission maximum of the Cur-polyester NP, provides a good signal-to-noise ratio in the data. The fluorescence decay as a function of time in Cur-PLA NP, Cur-PLGA NP and Cur-PCL NP are shown in Figure 6.7. The results for both Cur-polyester NP in H_2O (red traces) and D_2O (blue traces) are presented. The well overlapped decay traces indicate that the fluorescence decay of curcumin in polyester nanoparticle is the same for both with and without the addition of D_2O. All the time-resolved fluorescence decay traces were well fitted with a triexponential function and the fitted parameters are summarised in Table 6.2. It is important to note that the decay profiles of the different Cur-polyester NP are very similar. The same decay time constants for the three Cur-polyester NP indicate that the Cur-polyester NP provide a very similar environment where curcumin is located. The Cur-polyester NP exhibit a very fast decay component with a time constant of 2 – 5 ps, which is followed by a slower component of 40 – 70 ps and finally a slow 200 – 400 ps. The fast component of 2 – 4 ps is identical to those reported for curcumin in micelles, which has been assigned to reorganisation of water molecules [19].

Cur-polyester NP show a decay component on the order of 50 ps and it is in agreement with those reported for curcumin in DTAB and SDS micelles. This decay component has been assigned to the ESIHT of curcumin [19]. A previous study has shown that the ESIHT of curcumin encapsulated in micelle shows a very pronounced deuterium isotope effect (1.6 times longer in the time constant) [19]. For Cur-polyester NP, however, no deuterium isotope effect was observed in the presence of D_2O. The best-fit parameters shown in Table 6.2 are identical within error between Cur-polyester NP in H_2O and D_2O. Furthermore, the amplitudes between the Cur-polyester NP in H_2O and D_2O are very similar when the lifetime are fixed to 3.5, 55 and 300 ps for τ_1, τ_2 and τ_3, respectively, as shown in Table 6.3. To our knowledge, these results are the first work to investigate the excited state kinetics of curcumin encapsulated in polyester nanoparticles and to demonstrate the lack of deuterium isotope effects. It has been shown that the fluorescence decay of curcumin is very sensitive to the presence of hydrogen bonding interaction with the solvent [18, 19, 62, 63]. In other words, the rate

of ESIHT is dependent on the strength of intermolecular hydrogen bonding between curcumin and surrounding molecules [18, 19, 62, 63]. In this case, curcumin is able to form hydrogen bonds with the oxygen atoms in the ester group of polyesters (Figure 6.1) similar to the hydrogen bonds in protic solvents. The presence of a high number of hydrogen bonding interactions between curcumin and the polyester leads to a similar rate of ESIHT to those in polar protic solvents [18, 63]. For instance, the rates of ESIHT of curcumin in polyester nanoparticles are very similar to that of curcumin in methanol [18]. In the case of Cur-polyester NP, the high fluorescence quantum yield and the lack of a deuterium isotope effect indicate a low water content within the nanoparticle. Curcumin is located in a hydrophobic environment of the nanoparticle and segregated from water, giving rise to the suppression of hydrolysis. The superior stabilisation by polyester nanoparticles relative to micelles is attributable to the difference in the water content of the local environment where curcumin is encapsulated. The lack of deuterium isotope effect suggests that the interaction between curcumin and D_2O is limited by the polyester nanoparticles.

Table 6.3. Fluorescence Upconversion Decay Amplitude Parameters with Fixed Time Constants for Curcumin-encapsulated Polyester Nanoparticles.[a]

Polyester	Solvent	A_1	A_2	A_3
PLA	H_2O	0.18 ± 0.07	0.48 ± 0.20	0.34 ± 0.22
PLA	D_2O	0.20 ± 0.09	0.55 ± 0.19	0.25 ± 0.21
PLGA	H_2O	0.23 ± 0.12	0.26 ± 0.23	0.51 ± 0.23
PLGA	D_2O	0.21 ± 0.10	0.23 ± 0.25	0.56 ± 0.20
PCL	H_2O	0.18 ± 0.07	0.46 ± 0.14	0.36 ± 0.16
PCL	D_2O	0.23 ± 0.07	0.47 ± 0.13	0.30 ± 0.15

[a] The fluorescence upconversion traces, $f(t)$, were fitted with the multiexponential function $f(t) = A_1 e^{-t/3.5} + A_2 e^{-t/55} + A_3 e^{-t/300}$, where $A_1 + A_2 + A_3 = 1$. The reported values are the mean of three independent experiments and the error values are as in Table 6.2.

6.5 Conclusions

A simple one-step nanoprecipitation method for the preparation of nano-sized Cur-polyester NP with a negatively charged surface has been demonstrated. The resulting Cur-polyester NP, namely Cur-PLA NP, Cur-PLGA NP and Cur-PCL NP, enhance the stability, solubility and fluorescence emission of curcumin in an aqueous environment. The improvement is attributable to the lack of significant interactions between the encapsulated curcumin and water. The time-resolved fluorescence results have shown a lack of deuterium isotope effect in the fluorescence lifetime of Cur-polyester NP, which further support the absence of interaction between curcumin and water. The polyester nanoparticles segregate curcumin from water by encapsulating curcumin within the hydrophobic region of the nanoparticle. The Cur-polyester NP presented herein exhibit all the three features that are desirable as a curcumin delivery agent: (1) hydrophobic encapsulation of curcumin, (2) a hydrophilic surface to remain suspended in water and (3) a particle size of less than 100 nm.

6.6 References

(1) Roughley, P. J.; Whiting, D. A. Experiments in Biosynthesis of Curcumin. *J. Chem. Soc. Perkin. Trans. 1* **1973**, *20*, 2379–2388.

(2) Sa, G.; Das, T. Anti-Cancer Effects of Curcumin: Cycle of Life and Death. *Cell Division* **2008**, *3*, 1–14.

(3) Huang, M. T.; Lou, Y. R.; Ma, W.; Newmark, H. L.; Reuhl, K. R.; Conney, A. H. Inhibitory Effects of Dietary Curcumin on Forestomach, Duodenal, and Colon Carcinogenesis in Mice. *Cancer Res.* **1994**, *54*, 5841–5847.

(4) Rao, C. V.; Rivenson, A.; Simi, B.; Reddy, B. S. Chemoprevention of Colon Carcinogenesis by Dietary Curcumin, a Naturally-Occurring Plant Phenolic Compound. *Cancer Res.* **1995**, *55*, 259–266.

(5) Caruso, F.; Rossi, M.; Benson, A.; Opazo, C.; Freedman, D.; Monti, E.; Gariboldi, M. B.; Shaulky, J.; Marchetti, F.; Pettinari, R.; Pettinari, C. Ruthenium-Arene Complexes of Curcumin: X-Ray and Density Functional Theory Structure, Synthesis, and Spectroscopic Characterization, *in Vitro* Antitumor Activity, and DNA Docking Studies of (p-Cymene)Ru(Curcuminato)Chloro. *J. Med. Chem.* **2012**, *55*, 1072–1081.

(6) Lim, G. P.; Chu, T.; Yang, F. S.; Beech, W.; Frautschy, S. A.; Cole, G. M. The Curry Spice Curcumin Reduces Oxidative Damage and Amyloid Pathology in an Alzheimer Transgenic Mouse. *J. Neurosci.* **2001**, *21*, 8370–8377.

(7) Ono, K.; Hasegawa, K.; Naiki, H.; Yamada, M. Curcumin has Potent Anti-Amyloidogenic Effects for Alzheimer's β-Amyloid Fibrils *in Vitro*. *J. Neurosci. Res.* **2004**, *75*, 742–750.

(8) Yang, F. S.; Lim, G. P.; Begum, A. N.; Ubeda, O. J.; Simmons, M. R.; Ambegaokar, S. S.; Chen, P. P.; Kayed, R.; Glabe, C. G.; Frautschy, S. A.; Cole, G. M. Curcumin Inhibits Formation of Amyloid β Oligomers and Fibrils, Binds Plaques, and Reduces Amyloid *in Vivo*. *J. Biol. Chem.* **2005**, *280*, 5892–5901.

(9) Lantz, R. C.; Chen, G. J.; Solyom, A. M.; Jolad, S. D.; Timmermann, B. N. The Effect of Turmeric Extracts on Inflammatory Mediator Production. *Phytomedicine* **2005**, *12*, 445–452.

(10) Suresh, M. V.; Wagner, M. C.; Rosania, G. R.; Stringer, K. A.; Min, K. A.; Risler, L.; Shen, D. D.; Georges, G. E.; Reddy, A. T.; Parkkinen, J.; Reddy, R. C. Pulmonary Administration of Water-Soluble Curcumin Complex Reduces Severity of Acute Lung Injury. *Am. J. Respir. Cell Mol. Biol.* **2012**, *47*, 280–287.

(11) Kaminaga, Y.; Nagatsu, A.; Akiyama, T.; Sugimoto, N.; Yamazaki, T.; Maitani, T.; Mizukami, H. Production of Unnatural Glucosides of Curcumin with Drastically Enhanced Water Solubility by Cell Suspension Cultures of Catharanthus Roseus. *FEBS Lett.* **2003**, *555*, 311–316.

(12) Letchford, K.; Liggins, R.; Burt, H. Solubilization of Hydrophobic Drugs by Methoxy Poly(Ethylene Glycol)-Block-Polycaprolactone Diblock Copolymer Micelles: Theoretical and Experimental Data and Correlations. *J. Pharm. Sci.* **2008**, *97*, 1179–1190.

(13) Payton, F.; Sandusky, P.; Alworth, W. L. NMR Study of the Solution Structure of Curcumin. *J. Nat. Prod.* **2007**, *70*, 143–146.

(14) Chignell, C. F.; Bilskj, P.; Reszka, K. J.; Motten, A. G.; Sik, R. H.; Dahl, T. A. Spectral and Photochemical Properties of Curcumin. *Photochem. Photobiol.* **1994**, *59*, 295–302.

(15) Wang, Z. F.; Leung, M. H. M.; Kee, T. W.; English, D. S. The Role of Charge in the Surfactant-Assisted Stabilization of the Natural Product Curcumin. *Langmuir* **2010**, *26*, 5520–5526.

(16) Leung, M. H. M.; Colangelo, H.; Kee, T. W. Encapsulation of Curcumin in Cationic Micelles Suppresses Alkaline Hydrolysis. *Langmuir* **2008**, *24*, 5672–5675.

(17) Bong, P.-H. Spectral and Photophysical Behaviors of Curcumin and Curcuminoids. *Bull. Korean Chem. Soc.* **2000**, *21*, 81–86.

(18) Adhikary, R.; Mukherjee, P.; Kee, T. W.; Petrich, J. W. Excited-State Intramolecular Hydrogen Atom Transfer and Solvation Dynamics of the Medicinal Pigment Curcumin. *J. Phys. Chem. B* **2009**, *113*, 5255–5261.

(19) Adhikary, R.; Carlson, P. J.; Kee, T. W.; Petrich, J. W. Excited-State Intramolecular Hydrogen Atom Transfer of Curcumin in Surfactant Micelles. *J. Phys. Chem. B* **2010**, *114*, 2997–3004.

(20) Nardo, L.; Andreoni, A.; Másson, M.; Haukvik, T.; Tønnesen, H. H. Studies on Curcumin and Curcuminoids. XXXIX. Photophysical Properties of Bisdemethoxycurcumin. *J. Fluorescence* **2011**, *21*, 627–635.

(21) Wang, Y. J.; Pan, M. H.; Cheng, A. L.; Lin, L. I.; Ho, Y. S.; Hsieh, C. Y.; Lin, J. K. Stability of Curcumin in Buffer Solutions and Characterization of Its Degradation Products. *J. Pharm. Biomed. Anal.* **1997**, *15*, 1867–1876.

(22) Tønnesen, H. H.; Karlsen, J. Studies on Curcumin and Curcuminoids. VI. Kinetics of Curcumin Degradation in Aqueous Solution. *Z. Lebensm. Unters. Forsch.* **1985**, *180*, 402–404.

(23) Harada, T.; Pham, D.-T.; Leung, M. H. M.; Ngo, H. T.; Lincoln, S. F.; Easton, C. J.; Kee, T. W. Cooperative Binding and Stabilization of the Medicinal Pigment Curcumin by Diamide Linked γ-Cyclodextrin Dimers: A Spectroscopic Characterization. *J. Phys. Chem. B* **2011**, *115*, 1268–1274.

(24) Tønnesen, H. H.; Másson, M.; Loftsson, T. Studies of Curcumin and Curcuminoids. XXVII. Cyclodextrin Complexation: Solubility, Chemical and Photochemical Stability. *Int. J. Pharm.* **2002**, *244*, 127–135.

(25) Bisht, S.; Feldmann, G.; Soni, S.; Ravi, R.; Karikar, C.; Maitra, A.; Maitra, A. Polymeric Nanoparticle-Encapsulated Curcumin ("Nanocurcumin"): A Novel Strategy for Human Cancer Therapy. *J. Nanobiotechnology* **2007**, *5*, 18.

(26) Mohanty, C.; Acharya, S.; Mohanty, A. K.; Dilnawaz, F.; Sahoo, S. K. Curcumin-Encapsulated MePEG/PCL Diblock Copolymeric Micelles: A Novel Controlled Delivery Vehicle for Cancer Therapy. *Nanomedicine* **2010**, *5*, 433–449.

(27) Khalil, N. M.; do Nascimento, T. C. F.; Casa, D. M.; Dalmolin, L. F.; de Mattos, A. C.; Hoss, I.; Romano, M. A.; Mainardes, R. M. Pharmacokinetics of Curcumin-Loaded PLGA and PLGA-PEG Blend Nanoparticles after Oral Administration in Rats. *Colloids Surf. B* **2013**, *101*, 353–360.

(28) Tsai, Y.-M.; Chang-Liao, W.-L.; Chien, C.-F.; Lin, L.-C.; Tsai, T.-H. Effect of Polymer Molecular Weight on Relative Oral Bioavailability of Curcumin. *Int. J. Nanomedicine* **2012**, *7*, 2957–2966.

(29) Tsai, Y.-M.; Chien, C.-F.; Lin, L.-C.; Tsai, T.-H. Curcumin and its Nano-Formulation: The Kinetics of Tissue Distribution and Blood-Brain Barrier Penetration. *Int. J. Pharm.* **2011**, *416*, 331–338.

(30) Cartiera, M. S.; Ferreira, E. C.; Caputo, C.; Egan, M. E.; Caplan, M. J.; Saltzman, W. M. Partial Correction of Cystic Fibrosis Defects with PLGA Nanoparticles Encapsulating Curcumin. *Mol. Pharmaceutics* **2010**, *7*, 86–93.

(31) Chernenko, T.; Matthaeus, C.; Milane, L.; Quintero, L.; Amiji, M.; Diem, M. Label-free Raman Spectral Imaging of Intracellular Delivery and Degradation of Polymeric Nanoparticle Systems. *ACS Nano* **2009**, *3*, 3552–3559.

(32) Musyanovych, A.; Schmitz-Wienke, J.; Mailaender, V.; Walther, P.; Landfester, K. Preparation of Biodegradable Polymer Nanoparticles by Miniemulsion Technique and Their Cell Interactions. *Macromol. Biosci.* **2008**, *8*, 127–139.

(33) Chereddy, K. K.; Coco, R.; Memvanga, P. B.; Ucakar, B.; des Rieux, A.; Vandermeulen, G.; Preat, V. Combined Effect of PLGA and Curcumin on Wound Healing Activity. *J. Controlled Release* **2013**, *171*, 208–215.

(34) Verderio, P.; Bonetti, P.; Colombo, M.; Pandolfi, L.; Prosperi, D. Intracellular Drug Release from Curcumin-Loaded PLGA Nanoparticles Induces G2/M Block in Breast Cancer Cells. *Biomacromolecules* **2013**, *14*, 672–682.

(35) Punfa, W.; Yodkeeree, S.; Pitchakarn, P.; Ampasavate, C.; Limtrakul, P. Enhancement of Cellular Uptake and Cytotoxicity of Curcumin-Loaded PLGA Nano-particles by Conjugation with Anti-p-Glycoprotein in Drug Resistance Cancer Cells. *Acta Pharmacol. Sin.* **2012**, *33*, 823–831.

(36) Mukerjee, A.; Vishwanatha, J. K. Formulation, Characterization and Evaluation of Curcumin-Loaded PLGA Nanospheres for Cancer Therapy. *Anticancer Res.* **2009**, *29*, 3867–3875.

(37) Yallapu, M. M.; Gupta, B. K.; Jaggi, M.; Chauhan, S. C. Fabrication of Curcumin Encapsulated PLGA Nanoparticles for Improved Therapeutic Effects in Metastatic Cancer Cells. *J. Colloid Interface Sci.* **2010**, *351*, 19–29.

(38) Shao, J.; Zheng, D.; Jiang, Z.; Xu, H.; Hu, Y.; Li, X.; Lu, X. Curcumin Delivery by Methoxy Polyethylene Glycol-Poly(Caprolactone) Nanoparticles Inhibits the Growth of C6 Glioma Cells. *Acta Biochim. Biophys. Sin.* **2011**, *43*, 267–274.

(39) Lammers, T.; Hennink, W. E.; Storm, G. Tumour-Targeted Nanomedicines: Principles and Practice. *Br. J. Cancer* **2008**, *99*, 392–397.

(40) Maeda, H.; Wu, J.; Sawa, T.; Matsumura, Y.; Hori, K. Tumor Vascular Permeability and the EPR Effect in Macromolecular Therapeutics: A Review. *J. Control. Release* **2000**, *65*, 271–284.

(41) Maeda, H. Macromolecular Therapeutics in Cancer Treatment: the EPR Effect and Beyond. *J. Control. Release* **2012**, *164*, 138–144.

(42) Dufort, S.; Sancey, L.; Coll, J.-L. Physico-Chemical Parameters that Govern Nanoparticles Fate also Dictate Rules for Their Molecular Evolution. *Adv. Drug Delivery Rev.* **2012**, *64*, 179–189.

(43) Iyer, A. K.; Khaled, G.; Fang, J.; Maeda, H. Exploiting the Enhanced Permeability and Retention Effect for Tumor Targeting. *Drug Discov. Today* **2006**, *11*, 812–818.

(44) Clafton, S. N.; Huang, D. M.; Massey, W. R.; Kee, T. W. Femtosecond Dynamics of Excitons and Hole-Polarons in Composite P3HT/PCBM Nanoparticles. *J. Phys. Chem. B* **2013**, *117*, 4626–4633.

(45) Magde, D.; Rojas, G.; Seybold, P. Solvent Dependence of the Fluorescence Lifetimes of Xanthene Dyes. *Photochem. Photobiol.* **1999**, *70*, 737–744.

(46) Katz, O.; Small, E.; Bromberg, Y.; Silberberg, Y. Focusing and Compression of Ultrashort Pulses through Scattering Media. *Nature Photon.* **2011**, *5*, 372–377.

(47) Webster, M. A.; Gerke, T. D.; Weiner, A. M.; Webb, K. J. Spectral and Temporal Speckle Field Measurements of a Random Medium. *Opt. Lett.* **2004**, *29*, 1491–1493.

(48) Dogariu, A.; Kutsche, C.; Likamwa, P.; Boreman, G.; Moudgil, B. Time-Domain Depolarization of Waves Retroreflected from Dense Colloidal Media. *Opt. Lett.* **1997**, *22*, 585–587.

(49) Bruce, N. C.; Schmidt, F. E. W.; Dainty, J. C.; Barry, N. P.; Hyde, S. C. W.; French, P. M. W. Investigation of the Temporal Spread of an Ultrashort Light Pulse on Transmission through a Highly Scattering Medium. *Appl. Opt.* **1995**, *34*, 5823–5828.

(50) Henari, F. Z.; Cassidy, S.; Jasim, K. E.; Dakhel, A. A. Nonlinear Refractive Index Measurements of Curcumin With CW Laser. *J. Nonlinear Opt. Phys. Mater.* **2013**, *22*, 1350017.

(51) Lakowicz, J. R., *Principles of Fluorescence Spectroscopy*, 3rd ed.; Lakowicz, J. R., Ed.; Springer: 2006.

(52) Thioune, O.; Fessi, H.; Devissaguet, J.; Puisieux, F. Preparation of Pseudolatex by Nanoprecipitation: Influence of the Solvent Nature on Intrinsic Viscosity and Interaction Constant. *Int. J. Pharm.* **1997**, *146*, 233–238.

(53) Murakami, H.; Kobayashi, M.; Takeuchi, H.; Kawashima, Y. Further Application of a Modified Spontaneous Emulsification Solvent Diffusion Method to Various Types of PLGA and PLA Polymers for Preparation of Nanoparticles. *Powder Technology* **2000**, *107*, 137–143.

(54) Legrand, P.; Lesieur, S.; Bochot, A.; Gref, R.; Raatjes, W.; Barratt, G.; Vauthier, C. Influence of Polymer Behaviour in Organic Solution on the Production of Polylactide Nanoparticles by Nanoprecipitation. *Int. J. Pharm.* **2007**, *344*, 33–43.

(55) Lepeltier, E.; Bourgaux, C.; Couvreur, P. Nanoprecipitation and the "Ouzo Effect": Application to Drug Delivery Devices. *Adv. Drug Delivery Rev.* **2014**, *71*, 86–97.

(56) Galasso, V.; Kovac, B.; Modelli, A.; Ottaviani, M. F.; Pichierri, F. Spectroscopic and Theoretical Study of the Electronic Structure of Curcumin and Related Fragment Molecules. *J. Phys. Chem. A* **2008**, *112*, 2331–2338.

(57) Iwunze, M. O. Binding and Distribution Characteristics of Curcumin Solubilized in CTAB Micelle. *J. Mol. Liq.* **2004**, *111*, 161–165.

(58) Leung, M. H. M.; Kee, T. W. Effective Stabilization of Curcumin by Association to Plasma Proteins: Human Serum Albumin and Fibrinogen. *Langmuir* **2009**, *25*, 5773–5777.

(59) Mohammadi, F.; Bordbar, A.-K.; Divsalar, A.; Mohammadi, K.; Saboury, A. Analysis of Binding Interaction of Curcumin and Diacetylcurcumin with Human and Bovine Serum Albumin Using Fluorescence and Circular Dichroism Spectroscopy., English *Protein J.* **2009**, *28*, 189–196.

(60) Barik, A.; Mishra, B.; Kunwar, A.; Priyadarsini, K. I. Interaction of Curcumin with Human Serum Albumin: Thermodynamic Properties, Fluorescence Energy Transfer and Denaturation Effects. *Chem. Phys. Lett.* **2007**, *436*, 239–243.

(61) Hegde, A. H.; Sandhya, B.; Seetharamappa, J. Investigations to Reveal the Nature af Interactions af Human Hemoglobin with Curcumin Using Optical Techniques. *Int. J. Biol. Macromol.* **2013**, *52*, 133–138.

(62) Nardo, L.; Paderno, R.; Andreoni, A.; Másson, M.; Haukvik, T.; Tønnesen, H. H. Role of H-Bond Formation in the Photoreactivity of Curcumin. *Spectroscopy* **2008**, *22*, 187–198.

(63) Khopde, S. M.; Indira Priyadarsini, K.; Palit, D. K.; Mukherjee, T. Effect of Solvent on the Excited-State Photophysical Properties of Curcumin. *Photochem. Photobiol.* **2000**, *72*, 625–631.

CHAPTER 7

CONCLUDING REMARKS

Recent studies have shown that the biological activities of curcumin are related to its interaction with Cu(II) and keto-enol tautomerisation. However, the detailed mechanism of the mode of action is still unclear. This thesis explores the effect of Cu(II) on curcumin and tautomerisation of curcumin in solution using various spectroscopic techniques. In addition, a potential curcumin delivery system using polyester nanoparticles is described to improve its aqueous stability and solubility, which are important aspects for effective treatments.

The complexation between curcumin and Cu(II) and the degradation of curcumin due to reduction of Cu(II) have been investigated. The key findings are summarised in Chapter 3 and 4. The complexation constants indicate strong binding between curcumin and Cu(II), which suggests that curcumin is likely to complex with Cu(II) in biologically relevant environment. The transient absorption spectroscopic results show that the excited state of Cu(II)−Curcumin complexes exhibit a different excited state kinetics than that of curcumin as a consequence of charge transfer reaction. The results from UV-visible absorption, time-dependent mass spectrometry and high performance liquid chromatography reveal that the decomposition of curcumin in the presence of Cu(II) in acetonitrile correlates with the reduction of Cu(II) to Cu(I). The decomposition of curcumin is likely to generate reactive radicals. Therefore, it is proposed that the biological activity of curcumin is likely to be related to the generation of reactive oxygen species as a consequence of its complexation with Cu(II) in a reducing environment.

Furthermore, the investigation on tautomerisation of curcumin is presented in Chapter 5. The activation energy of tautomerisation of curcumin has been determined for the first time. The activation energy of tautomerisation of curcumin is significantly

lower in D_2O/acetone-d_6 and D_2O/acetonitrile-d_3 than that in neat methanol-d_4. The difference in the activation energy values is attributable to the presence of water. This result suggests that the presence of the diketo tautomer is favoured in the presence of water. It is also possible that the diketo tautomer is involved in the mode of action of curcumin.

In addition, a one-step nanoprecipitation method for the preparation of nano-sized Cur-polyester NP with a negatively charged surface has been demonstrated in Chapter 6. The resulting Cur-polyester NPs enhance the stability, solubility and fluorescence emission of curcumin in an aqueous environment due to efficient segregation of curcumin from bulk water. These Cur-polyester NPs show potential as curcumin delivery agents.

Overall, this thesis has offered two perspectives regarding the medicinal activities of curcumin. The experiments have been designed and carried out using SDS micelles as a simple membrane model. As a consequence of the methodology, the results presented using this membrane model are likely to be different in a cell environment. To provide further insight with a biological emphasis on the behaviour of curcumin, there is a great need for investigations using other membrane models, such as small unilamellar phospholipid vesicles, which bear more resemblance to phosphate lipid bilayer [1, 2].

Furthermore, uptake and viability studies of the Cur-polyester NP in human cells are essential to evaluate their potential as curcumin delivery agents [3, 4]. In order to study the Cur-polyester NP in a cell environment, the issue of rapid self-aggregation in a buffered environment needs to be addressed. The electrostatic repulsion between nanoparticles inhibits their self-aggregation, which can be achieved by extra coating of polyelectrolytes that provides significant surface charges [5, 6].

7.1 References

(1) Dietrich, C.; Bagatolli, L.; Volovyk, Z.; Thompson, N.; Levi, M.; Jacobson, K.; Gratton, E. Lipid Rafts Reconstituted in Model Membranes. *Biophys. J.* **2001**, *80*, 1417–1428.

(2) Maiti, K.; Mukherjee, K.; Gantait, A.; Saha, B. P.; Mukherjee, P. K. Curcumin-Phospholipid Complex: Preparation, Therapeutic Evaluation and Pharmacokinetic Study in Rats. *Int. J. Pharm.* **2007**, *330*, 155–163.

(3) Harada, T.; Giorgio, L.; Harris, T. J.; Pham, D.-T.; Ngo, H. T.; Need, E. F.; Coventry, B. J.; Lincoln, S. F.; Easton, C. J.; Buchanan, G.; Kee, T. W. Diamide Linked γ-Cyclodextrin Dimers as Molecular-Scale Delivery Systems for the Medicinal Pigment Curcumin to Prostate Cancer Cells. *Mol. Pharmaceutics* **2013**, *10*, 4481–4490.

(4) Kunwar, A.; Barik, A.; Mishra, B.; Rathinasamy, K.; Pandey, R.; Priyadarsini, K. Quantitative Cellular Uptake, Localization and Cytotoxicity of Curcumin in Normal and Tumor Cells. *Biochim. Biophys. Acta - General Subjects* **2008**, *1780*, 673–679.

(5) Win, K. Y.; Feng, S.-S. Effects of Particle Size and Surface Coating on Cellular Uptake of Polymeric Nanoparticles for Oral Delivery of Anticancer Drugs. *Biomaterials* **2005**, *26*, 2713–2722.

(6) Bagwe, R. P.; Hilliard, L. R.; Tan, W. Surface Modification of Silica Nanoparticles to Reduce Aggregation and Nonspecific Binding. *Langmuir* **2006**, *22*, 4357–4362.

APPENDIX A

SUPPORTING INFORMATION: REDUCTION OF COPPER(II) TO COPPER(I) IN THE COPPER–CURCUMIN COMPLEX INDUCES DECOMPOSITION OF CURCUMIN

A.1 Time-dependent Mass Spectrometry of the Copper(II)−Curcumin Complex

Mass Spectrometry Studies

Mass spectrometry studies were performed on acetonitrile solutions consisting of 10 µM curcumin with 0, 20 and 100 µM Cu(II) at 0, 6 and 24 h after preparation. The same studies were also conducted using 10 µM curcumin in methanol with 0, 20 and 100 µM Cu(II) at 0, 6 and 24 h after preparation. Briefly, solutions of 5.42 mM (2 mg mL^{-1}) curcumin in acetonitrile and 50 mM $CuSO_4$ in water were used as stock for the experiments involving acetonitrile. For the experiment with methanol as the solvent, 5.42 mM curcumin and 50 mM $CuSO_4$, both in methanol, were used as stock. A volume of 9-µL of the curcumin stock was added to 5 mL of either acetonitrile or methanol to yield a 10-µM curcumin solution. To achieve a Cu(II) concentration of either 20 or 100 µM, aliquots of 2 or 20 µL of the Cu(II) stock was added to the corresponding 5-mL 10 µM curcumin solution. No precipitation was observed for all samples over 24 h. Mass spectra were recorded in the negative ion mode using an LTQ Orbitrap XL (Thermo Fisher Scientific) for high resolution and high mass accuracy. The

samples were introduced by nanoelectrospray from platinum-coated borosilicate capillaries made in-house. Instrumental parameters were typically: spray voltage 1.5 kV, capillary temperature 200 °C, MS1 scan *m/z* range 50 – 1000, resolution 30 000, and maximum inject time 200 ms.

Mass Spectrometry of the Copper(II)−Curcumin Complex in Acetonitrile

Mass spectrometry was used to provide insight into the presence of metabolites as a result of curcumin decomposition due to reduction of Cu(II) to Cu(I). The mass spectra of 10 µM curcumin in acetonitrile in the presence of 20 µM Cu(II) at 0, 6 and 24 h after preparation are shown in Figure A.1. The mass spectrum at 0 h shows two major peaks at mass-to-charge ratios (*m/z*) of 367.1 and 183.1, which correspond to the singly deprotonated curcumin and the doubly deprotonated curcumin anions, respectively. The top panel of Figure A.1 shows that the peak at *m/z* = 367.1 decreases over time due to decomposition of curcumin. In particular, at 24 h after preparing the solution, this peak is no longer the most abundant species in the spectrum (Figure A.1 bottom panel). In contrast, the most abundant species are those with *m/z* = 89.1 and 125.0. The emergence of these species with lower molecular weights after 24 h of curcumin decomposition clearly indicates the formation of metabolites of curcumin. Curcumin alone in acetonitrile is very stable over the course of 24 h, as shown in the mass spectra in Figure A.2. Although the mass spectra in Figure A.1 are insufficient to determine the structures of the metabolites, they offer the first insight into the presence of these metabolites in the decomposition of curcumin in acetonitrile due to reduction of Cu(II) to Cu(I).

Mass spectra were also collected for 10 µM curcumin in acetonitrile at 0 h in the presence of 0, 20 and 100 µM Cu(II). The results, which are presented in Figure A.3, show that the mass spectra are independent of Cu(II) concentration, with curcumin$^-$, (M-H)$^-$ (*m/z* = 367.1) as the most abundant species. The persistence of the *m/z* = 367.1 peak with the absence of any evidence of metabolites as a function of Cu(II) concentration at 0 h is consistent with the assignment of the 350 nm UV-vis absorption peak in Figure 4.2c as the diketo tautomer of curcumin.

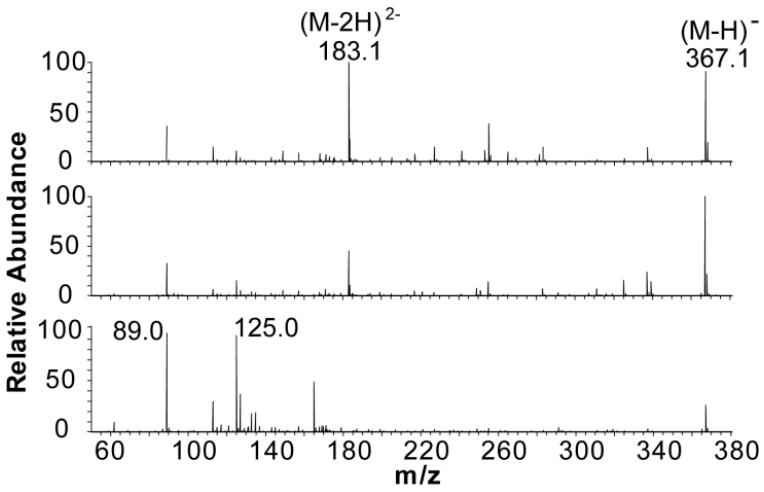

Figure A.1. Mass spectra of 10 µM curcumin in the presence of 20 µM Cu(II) in acetonitrile at 0 h (top), 6 h (middle), and 24 h (bottom) after preparation. The peaks at *m/z* = 367.1 and 183.1 correspond to curcumin $(M\text{-}H)^-$ and curcumin $(M\text{-}H)^{2-}$, respectively. The emergence of the peak at *m/z* = 89.0 and those around *m/z* = 125.0 as a function of time indicates the appearance of curcumin metabolites due to decomposition.

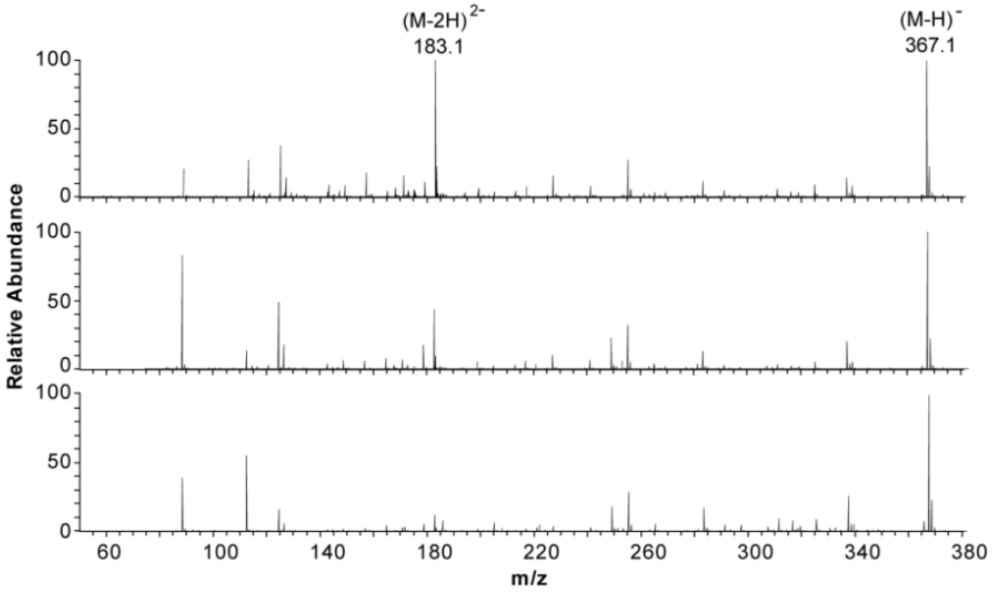

Figure A.2. Mass spectra of 10 µM curcumin in acetonitrile at 0 h (top), 6 h (middle), and 24 h (bottom). The results show that curcumin (*m/z* = 367.1) is the most abundant species throughout, indicating the absence of any degradation. Note that the *m/z* = 183.1 peak corresponds to doubly charged curcumin.

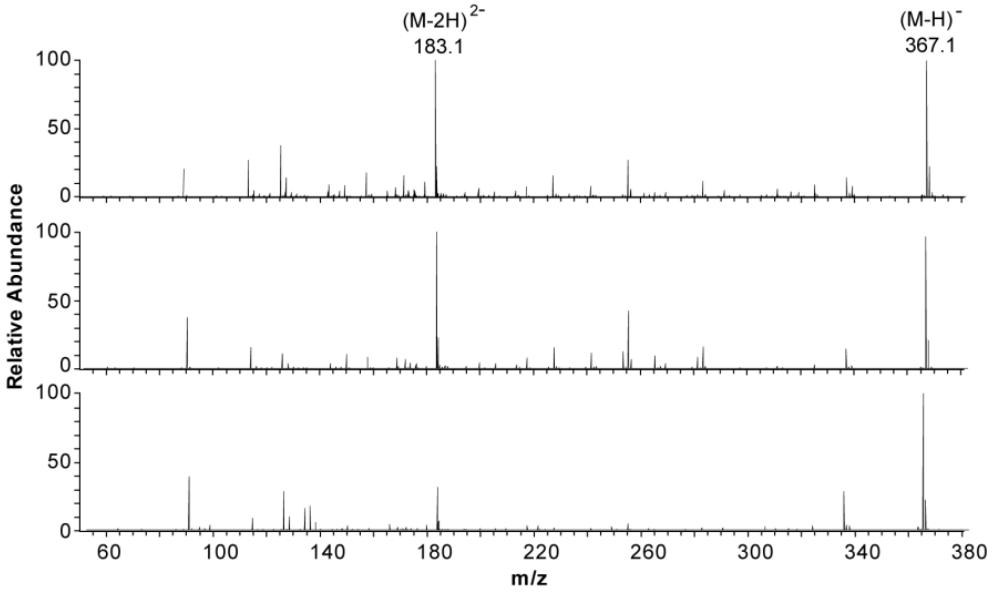

Figure A.3. Mass spectra of 10 µM curcumin in acetonitrile at 0 h with the following Cu(II) concentrations: 0 µM (top), 20 µM (middle), and 100 µM (bottom).

A.2 Time-dependent High Performance Liquid Chromatography of the Copper(II)−Curcumin Complex

High Performance Liquid Chromatography Studies

A 13.6 mM (5 mg mL^{-1}) curcumin solution was prepared in acetonitrile. A 6.63-µL aliquot of this solution was first added to 3 mL of acetonitrile to achieve a final curcumin concentration of 30 µM. For a 300-µM Cu(II) concentration (a 10:1 Cu(II):Curcumin molar ratio), an aliquot of 90-µL was added to the curcumin solution resulting in a clear solution. Reversed-phase high performance liquid chromatography (RP-HPLC) was performed on an Agilent 1200 using a Phenomenex Gemini 5 µm C18 column 110A (250 mm × 4.6 mm). The buffer system used was 0.1 %v/v trifluoroacetic acid in water (pH 2) with a linear gradient from 25 – 75 % acetonitrile over 30 min. The flow rate was 1 mL min^{-1} and the curcumin metabolites were detected at 350 nm. The HPLC chromatograms were presented as milli-absorbance unit (mAU) vs time.

High Performance Liquid Chromatography Analyses of the Copper(II)−Curcumin Complex in Acetonitrile

Figure A.4 show the HPLC chromatograms of the 10:1 molar ratio Cu(II):Curcumin acetonitrile solution at 0 and 24 h. The HPLC chromatogram in Figure A.4a has a peak with a retention time (t_R) of 23.8 min. A comparison of this HPLC chromatogram with that of curcumin alone in acetonitrile (Figure A.5, $t_R \approx$23 min) shows that this peak corresponds to curcumin in acetonitrile and the high level of agreement between the two chromatograms indicates negligible decomposition at 0 h, as is expected. At 24 h, however, the HPLC chromatogram (Figure A.4b) is greatly different from that at 0 h. First, the absence of any signals with a t_R of 23.8 min suggests that curcumin is largely decomposed, which is consistent with the UV-vis absorption and the mass spectrometry data. Second, owing to the significant decomposition of curcumin at

24 h, the signals with t_R values of 2.3 min and 3.3 min in Figure A.4b are attributable to the metabolites of curcumin. The formation of these metabolites is strictly dependent on the presence of Cu(II) because the HPLC chromatograms of curcumin alone in acetonitrile over 24 h show negligible changes over 24 h.

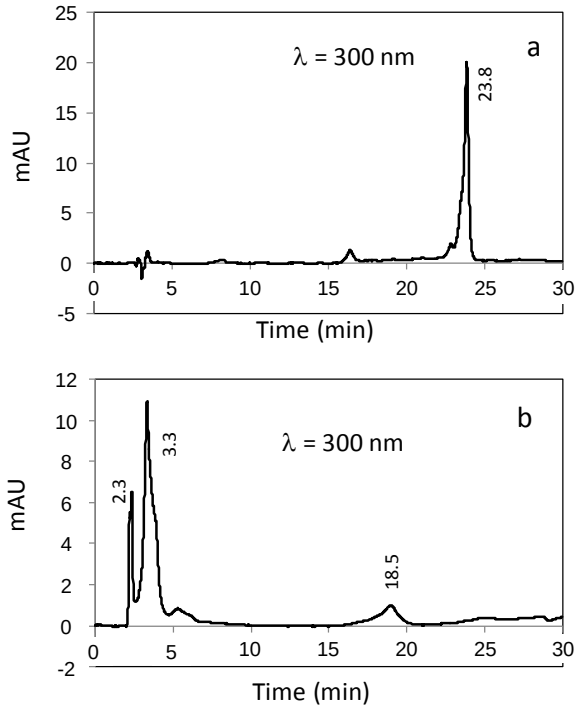

Figure A.4. HPLC chromatograms of 30 µM curcumin in the presence of 300 µM Cu(II) in acetonitrile (10:1 Cu(II):Curcumin ratio) at (a) 0 h, and (b) 24 h at $\lambda = 300$ nm. The signal at $t_R = 23.8$ min in (a) corresponds to curcumin and those at $t_R = 2.3$ min and 3.3 min in (b) correspond to curcumin metabolites due to decomposition.

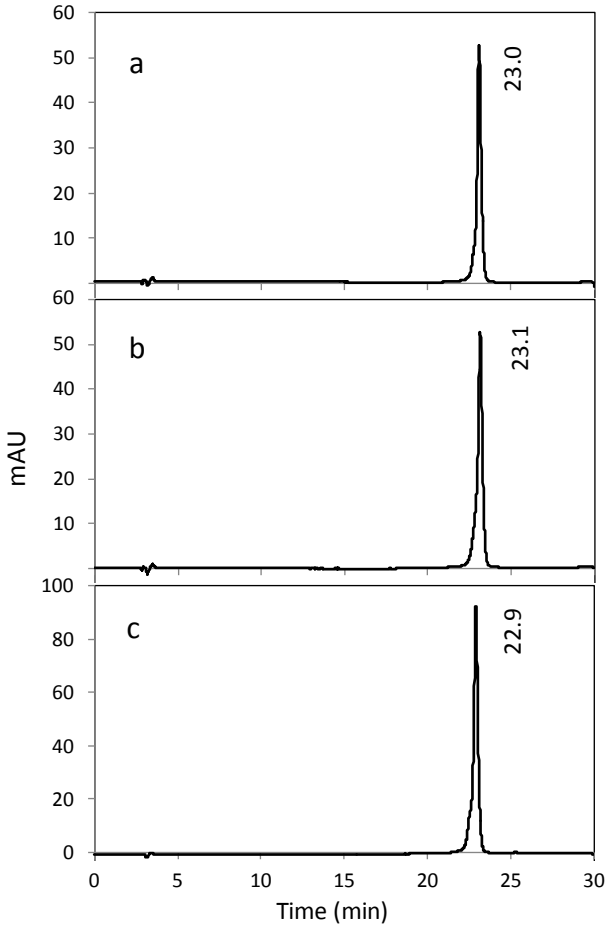

Figure A.5. HPLC chromatograms of 10 µM curcumin in acetonitrile at (a) 0 h, (b) 6 h, and (c) 24 h after equilibration are identical within experimental error, showing that the level of degradation is negligible.

APPENDIX B

SUPPORTING INFORMATION: KETO–ENOL TAUTOMERISATION OF THE MEDICINAL PIGMENT CURCUMIN

B.1 MATLAB Script for the Determination of the Rate Constant of Tautomerisation of Curcumin

The script used for data analysis according to the rate equations in Chapter 5 is shown in the following:

```
function diff=CD3OD(x,t1,NorH)
% This script is written for curcumin in deuterated methanol.
dt=0.0005;                % time interval of the fitiing
k1=x(1)*2000;             % larger than k2 by a factor of 2000
                          % (see Section 5.4.2)
k2=x(1);                  % rate of tautomerisation
k3=x(1)*K;                % multiply k2 by the equilibrium
                          % constant,K,(see Table 5.1).
t(1,1)=0;
A(1,1)=NorH(1);
B(1,1)=0;
C(1,1)=0;
D(1,1)=0;
E(1,1)=0;
od(1,1)=2267;             % number of OH with respect to curcumin,
                          % 227 for Acetone and Acetonitrile.
```

```
oh(1,1)=5;                  % number of OD with respect to curcumin,
                            % 0.2 for Acetone and Acetonitrile.
    for i=2:(t1(end)/dt),
        t(i,1) = (i-1)*dt;

        A(i,1) = A(i-1,1) + (-k1*A(i-1,1)*od(i-1,1) + ...
            (k1*B(i-1,1)*oh(i-1,1)))*dt;
        B(i,1) = B(i-1,1) + ((k1*A(i-1,1)*od(i-1,1)) + ...
            (-k2*B(i-1,1)) + (k3*C(i-1,1)) + ...
            (-k1*B(i-1,1)*oh(i-1,1)))*dt;

        od(i,1)= od(i-1,1) + ((-k1*A(i-1,1)*od(i-1,1)) + ...
            (k1*B(i-1,1)*oh(i-1,1)))*dt;
        oh(i,1)= oh(i-1,1) + ((k1*A(i-1,1)*od(i-1,1)) + ...
            (-k1*B(i-1,1)*oh(i-1,1)))*dt;

        C(i,1) = C(i-1,1) + ((k2*B(i-1,1)) + (-k3*C(i-1,1)) + ...
            (-k3*C(i-1,1)) + (k2*D(i-1,1)))*dt;
        D(i,1) = D(i-1,1) + ((k3*C(i-1,1)) + (-k2*D(i-1,1)) + ...
            (-k1*D(i-1,1)*od(i-1,1)) + ...
            (k1*E(i-1,1)*oh(i-1,1)))*dt;
        E(i,1) = E(i-1,1) + ((k1*D(i-1,1)*od(i-1,1)) + ...
            (-k1*E(i-1,1)*oh(i-1,1)))*dt;

        od(i,1)= od(i,1) + ((-k1*D(i-1,1)*od(i,1)) + ...
            (k1*E(i-1,1)*oh(i,1)))*dt;
        oh(i,1)= oh(i,1) + ((k1*D(i-1,1)*od(i,1)) + ...
            (-k1*E(i-1,1)*oh(i,1)))*dt;
    end
new_NorH=interp1(t1,NorH,t);
new_NorH(isnan(new_NorH))=0;
diff=(A+B)-new_NorH;    %(A+B) is the raw data and
                        % new_NorH is the fitting
```

APPENDIX C

SUPPORTING INFORMATION: NANOPRECIPITATION AND SPECTROSCOPIC CHARACTERISATION OF CURCUMIN-ENCAPSULATED POLYESTER NANOPARTICLES

C.1 Determination of the Number of Curcumin Encapsulated in Polyester Nanoparticles

The average number of curcumin encapsulated in each polyester nanoparticle is estimated arithmetically. The volume of each nanoparticle is calculated from the diameter of nanoparticle assuming that the nanoparticles are spherical in shape, as shown in Table C.1. Furthermore, the mass of each nanoparticle is estimated from the volume of nanoparticle and density of polyester, as shown in Table C.2, assuming the major constituent of nanoparticle is polyester.

Table C.1. Summary of Diameter, Volume and Mass of Cur-polyester Nanoparticles.

Cur-polyester NP	**Diameter of NP**[a] ($\times 10^{-6}$ cm)	**Volume of NP**[b] ($\times 10^{-16}$ cm^3)	**Mass of NP**[c] ($\times 10^{-16}$ g)
PLA	8.9	3.69	4.87
PLGA	6.8	1.65	2.14
PCL	9.6	4.63	5.33

[a] Data from dynamic light scattering experiment.
[b] Assuming spherical shaped nanoparticles, $V = \frac{4}{3}\pi r^3$.
[c] Assuming the nanoparticle has same density as the polyester, $\rho = \frac{m}{V}$.

Table C.2. Summary of Molecular Weight, Mass and Density of Curcumin and Polyester Used in Preparation of Cur-polyester Nanoparticles.

Curcumin	**Molecular Weight** (g mol^{-1})	**Mass**[a] (g)	**Density** (g cm^{-3})
Curcumin	368.39	0.00005	-
PLA	60000	0.00025	1.32
PLGA	57500	0.00025	1.30
PCL	45000	0.00025	1.15

[a] For a 50 % yield of nanoparticle, the resulting mass is half for both curcumin and polyester in the final nanoparticle solution.

Assuming there is complete encapsulation of curcumin by polyester nanoparticles and there is no free curcumin aggregates in water, the average number of curcumin in each nanoparticle is therefore estimated using Equation (C.1), as shown in Table C.3.

$$\langle n \rangle_{\text{Cur per NP}} = \frac{n_{\text{Cur}_{\text{Total}}}}{n_{\text{NP}_{\text{Total}}}} \tag{C.1}$$

where $n_{\text{Cur}_{\text{Total}}}$ and $n_{\text{NP}_{\text{Total}}}$ denote the total number of curcumin and polyester nanoparticles, respectively.

Table C.3. Summary of Total Number of Polyester Nanoparticles and Curcumin Molecules and the Average Number of Curcumin Molecules in a Cur-polyester Nanoparticle.

Cur-polyester NP	**Total Number of NP**[a] ($\times 10^{11}$)	**Total Number of Curcumin**[b] ($\times 10^{16}$)	**Number of Curcumin in NP**[c] ($\times 10^{4}$)
PLA	5.1	4.1	8.0
PLGA	11.7	8.2	7.0
PCL	4.7	8.2	17.4

[a] $n_{\text{NP}_{\text{Total}}} = \frac{\text{mass}_{\text{polyester}}}{\text{mass}_{\text{NP}}}$.

[b] $n_{\text{Cur}_{\text{Total}}} = \frac{\text{mole}_{\text{Cur}}}{N_{\text{A}}}$ where N_{A} is the Avogadro's constant.

C.2 Determination of the Distance between Adjacent Curcumin

The volume of nanoparticles occupied by each curcumin molecule is estimated using Equation (C.2).

$$V_{\text{Cur}} = \frac{V_{\text{NP}}}{\langle n \rangle_{\text{Cur per NP}}} \tag{C.2}$$

where V_{NP} and $\langle n \rangle_{\text{Cur per NP}}$ denote the volume of polyester nanoparticle and the average number of curcumin in a nanoparticle, respectively. Assuming curcumin is uniformly distributed and occupied a spherical volume inside each polyester nanoparticle, therefore, the distance between curcumin equal to the diameter of the sphere, as shown in Table C.4.

Table C.4. Average Volume of a Polyester Nanoparticle and Average Distance between Adjacent Curcumin in a Cur-polyester Nanoparticle.

Cur-polyester NP	**Volume of NP per Curcumin** ($\times 10^{-21}$ cm^3)	**Distance between Curcumin** (nm)
PLA	4.6	2.07
PLGA	2.4	1.65
PCL	2.7	1.72